Studies on Room-Temperature Chemical Sintering of Metal Nanoparticles by Ligand Exchange with Tri-*n*-Octylphosphine Oxide and Subsequent Dipping into an Organic Solvent Containing a Sintering Agent

March 2022

Graduate School of Systems Engineering

Wakayama University

Soichiro Okada

トリ-*n*-オクチルホスフィンオキシドとの
配位子交換に続く焼結促進剤を含む
有機溶媒への浸漬による
金属ナノ粒子の室温焼結に関する研究

令和 4 年 3 月

和歌山大学大学院システム工学研究科

岡田　宗一郎

Abstract

To aim at the application for electronics fields such as flexible display and heterogenerous catalysis, room-temperature (RT) chemical sintering of metal nanoparticles (NPs) was performed by dipping into an organic solvent containing a sintering agent. The coalescence of metal NPs was systematically investigated with the various combinations of metal, ligand, dipping solvent, and sintering agent. Furthermore, electrical resistivity and catalytic activity of the obtained porous metal thin films were evaluated.

In this study, the author mainly disclosed the following three points.

1. The lowest electrical resistivity of the Ag thin film on the PET substrate obtained from tri-*n*-octylphosphine oxide (TOPO)-capped Ag NP paste was $(1.2 \pm 0.5) \times 10^{-5}$ Ω m in the case of dipping into the methanol solution containing cetyltrimethylammonium chloride at RT. In addition, it was shown by X-ray diffraction pattern (XRD) and X-ray photoelectron spectroscopy (XPS) measurements that the purity of the obtained Ag thin film was comparatively high. (Chapter 2)
2. The Cu/Ag thin film on the PET substrate was prepared from TOPO-capped Cu-Ag core-shell (Cu@Ag) NPs by dipping into the 29 mM HCl methanol solution at RT. The lowest electrical resistivity of the obtained Cu/Ag thin film was $(5.1 \pm 1.7) \times 10^{-5}$ Ω m. The effective coalescence of Cu@Ag NPs with slight oxidation was successfully achieved at RT. (Chapter 3)
3. Owing to the use of TOPO as a sacrificial template, porous Pd structures were successfully obtained from Pd NPs by dipping into the methanol solution containing KOH at RT. The catalytic activity of porous Pd structures in the Suzuki coupling reaction increased with the increase of the KOH concentration in the RT sintering. (Chapter 4)

Based on these results, the author concludes that the RT chemical sintering method developed in this study could be adapted to the fabrication of electrodes on printed electronics and heterogeneous catalysts at low cost and energy. The findings obtained in this study would largely contribute to the development of industries using metal thin films such as electronics, chemical industry, and cells.

概要

本研究では, フレキシブルディスプレイなどのエレクトロニクス分野や不均一系触媒分野への応用を指向し, 金属ナノ粒子の焼結促進剤を含む有機溶媒浸漬による室温焼結について検討した。金属, 配位子, 浸漬溶媒, 焼結促進剤の組み合わせを変えて, ナノ粒子の融合度を系統的に評価した。そして, 得られた多孔性金属薄膜の抵抗率や触媒活性を評価した。

この研究においては, 主に以下の三点について明らかにした。

1. トリ-*n*-オクチルホスフィンオキシド(TOPO) 修飾銀ナノ粒子ペーストを塩化セチルトリメチルアンモニウムメタノール溶液に浸漬することで, 最小抵抗率 (~10^{-5} Ω m) の銀薄膜がポリエチレンテレフタレート (PET) 基板上で得られた。また, X 線回折法 (XRD) と X 線光電子分光法 (XPS) から, 得られた薄膜は純度の高い銀であることがわかった (第二章).
2. TOPO 修飾 Cu-Ag コアシェル型 (Cu@Ag) ナノ粒子を 29 mM HCl メタノール溶液に室温で浸漬することで, Cu/Ag 薄膜を PET 基板上で作製した。得られた薄膜の最小抵抗率は $(5.1 \pm 1.7) \times 10^{-5}$ Ω m だった。この結果より, Cu@Ag ナノ粒子は室温でも効果的に融合し, 酸化も抑制されていることがわかった (第三章).
3. 犠牲鋳型として TOPO を用いて, Pd ナノ粒子を KOH メタノール溶液に室温で浸漬することで多孔性 Pd 構造体を作製した。鈴木カップリング反応における多孔性 Pd 構造体の触媒活性は, 室温焼結時の KOH 濃度の増加に伴って増加した (第四章).

これらの結果を基に, 本研究で開発した室温焼結法はプリンテッドエレクトロニクスでの配線材料や不均一系触媒の低価格で省エネルギーの製造に応用できると結論づけた。この研究で得られた知見は, 金属薄膜を用いるエレクトロニクス, 化学工業, 電池などの産業発展に大きく貢献するであろう。

Preface

The studies of this thesis were carried out under the guidance of Professor Setsuko Yajima at Graduate School of Systems Engineering, Wakayama University.

The objective of these studies is to develop a room-temperature chemical sintering method of metal nanoparticles for the application in the fields of electronics and catalysis.

Soichiro Okada

Graduate School of Systems Engineering,

Wakayama University

Sakae−dani 930, Wakayama 640−8510, Japan

March 2022

Index

Chapter 1: General Introduction

Section 1-1: Background

1-1-1 Metal Nanoparticles (NPs)

Nanoparticle (NP) is a very small particle ranging in size from 1 to 100 nm and it generally consists of organic polymers [1, 2] and inorganic materials such as silica [3-6]. Particularly, metal NPs have attracted much attention in various industrial fields such as electronics [7], biomedical assay [8-10], photovoltaics [11, 12], and catalysis [13] due to the specific properties (e.g., surface plasmon resonance [14-18], melting point depression [19], and high catalytic activity [20, 21]), depending on their size and shape. As materials of metal NPs, noble metals such as Au [22], Ag [23], Pt [24], and Pd [25] are general and other common metals such as Cu [26], Fe [27], Co [28], Ni [29], and Al [30] are also often used. Among them, Au, Ag, and Cu NPs show the local surface plasmon resonance [31], which is the unique property originated from the miniaturization of metals. In addition, catalytic activities of some metal NPs (e.g. Pt, Pd, Au, etc.) are remarkably higher than those of their bulk metals due to the much larger surface area [32].

Meanwhile, metal NPs easily aggregate due to their high surface energy. Normally, the surface of metal NPs is covered with organic compounds such as surfactants in order to prevent their aggregation (Figure 1-1a). This kind of compound is called ligand. The ligand consists of two parts, adsorption group and non-adsorption moiety (Figure 1-1b). The adsorption groups of ligands interact with the surface of metal NPs. Adsorption groups of thiol [33], carboxy [34], amino [35], phosphine [36], phosphine oxide [37], and hydroxy groups [38] have been used, depending on the kind of metal. The non-adsorption moiety (e.g. alkyl chain and aromatic ring) of ligands affects the solvent dispersibility of metal NPs. Metal NPs covered with ligands having a hydrophilic group disperse in polar solvents (e.g. water and ethanol). On the other hand, metal NPs covered with ligands having a hydrophobic group disperse in non-polar solvents (e.g. *n*-hexane and cyclohexane). The available ligands, however, are severely limited by the synthetic conditions of metal NPs. Therefore, ligand exchange has been performed for the functionalization after the synthesis of metal NPs (Figure 1-2) [39-45].

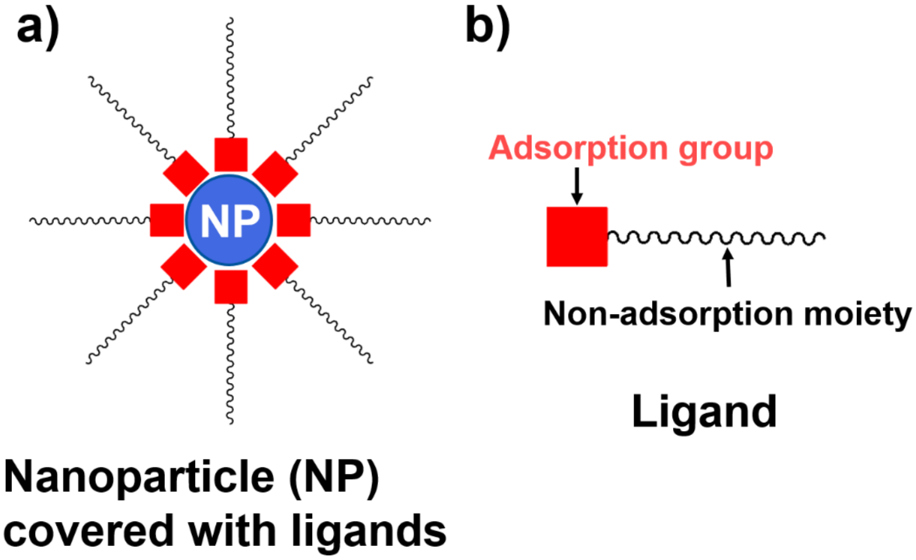

Figure 1-1. Illustration of (a) NP covered with ligands and (b) composition of ligand.

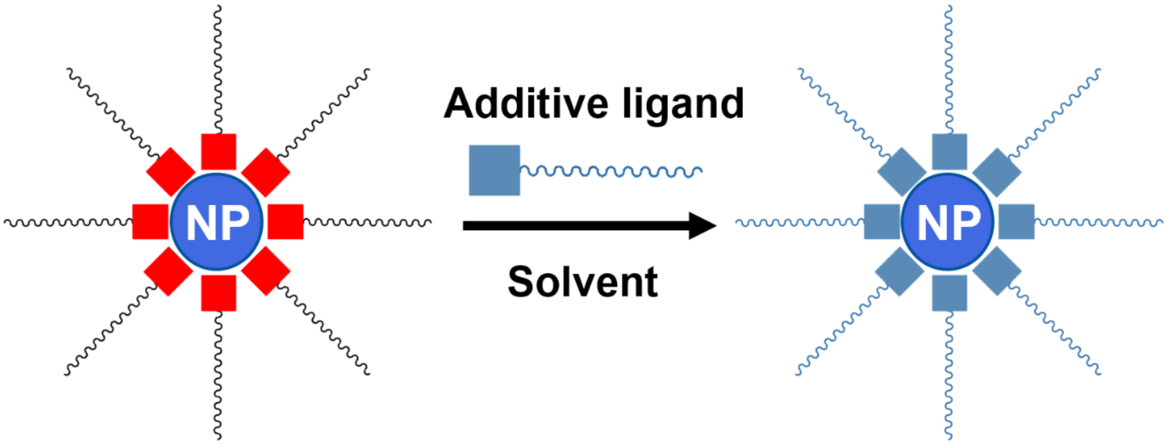

Figure 1-2. Ligand exchange on the surface of metal NPs.

1-1-2 Ligand Exchange on the Surface of Metal NPs

Ligand exchange proceeds based on adsorption equilibrium towards the surface of metal NPs between original ligands and additive ligands (Figure 1-3a) [39]. If the adsorption strength of additive ligands is almost the same as that of original ligands, the progress degree of ligand exchange is determined by the molar ratio of original ligands to additive ligands. On the other hand, if the adsorption strength of additive ligands is much larger than that of original ligands, ligand exchange proceeds irreversibly (Figure 1-3b). In this case, original ligands are completely replaced with additive ligands.

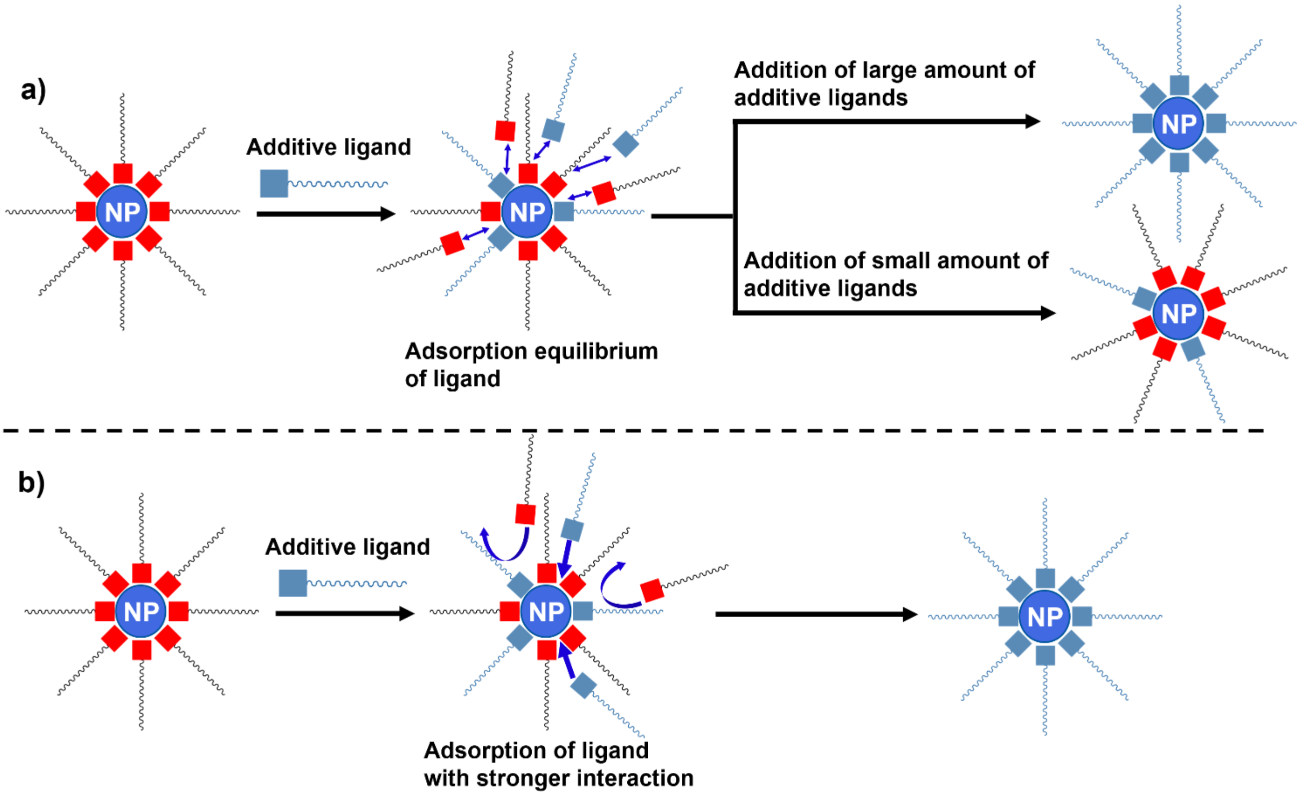

Figure 1-3. Ligand exchange based on (a) adsorption equilibrium and (b) difference of adsorption strength.

Ligand exchange is conducted by the following two methods: single-phase system and two-phase system. In the single-phase method, metal NPs are mixed with additive ligands in a homogeneous solvent (Figure 1-4a) [39-43]. The kinds of ligands are limited by their solubility to the dispersion of metal NPs. Although the diameters of metal NPs do not change during the ligand exchange, the crystallinity could change in some cases [40, 42]. The two-phase system method is performed in a mixture of two immiscible solvents (Figure 1-4b) [44, 45]. The ligand exchange proceeds through phase transfer of NPs. For example, the *n*-hexane dispersion of Ag_2Se NPs capped with 1-dodecanethiol was combined with the *N.N*-dimethylformamide (DMF) solution of 11-mercaptoundecanoic acid as an additive ligand [45] (Figure 1-5). Although Ag_2Se NPs capped with 1-dodecanethiol before the ligand exchange do not disperse in DMF, Ag_2Se NPs capped with 11-mercaptoundecanoic acid after the ligand exchange disperse in various hydrophilic media such as water. Thus, solvent dispersibility of metal NPs could be controlled by ligands.

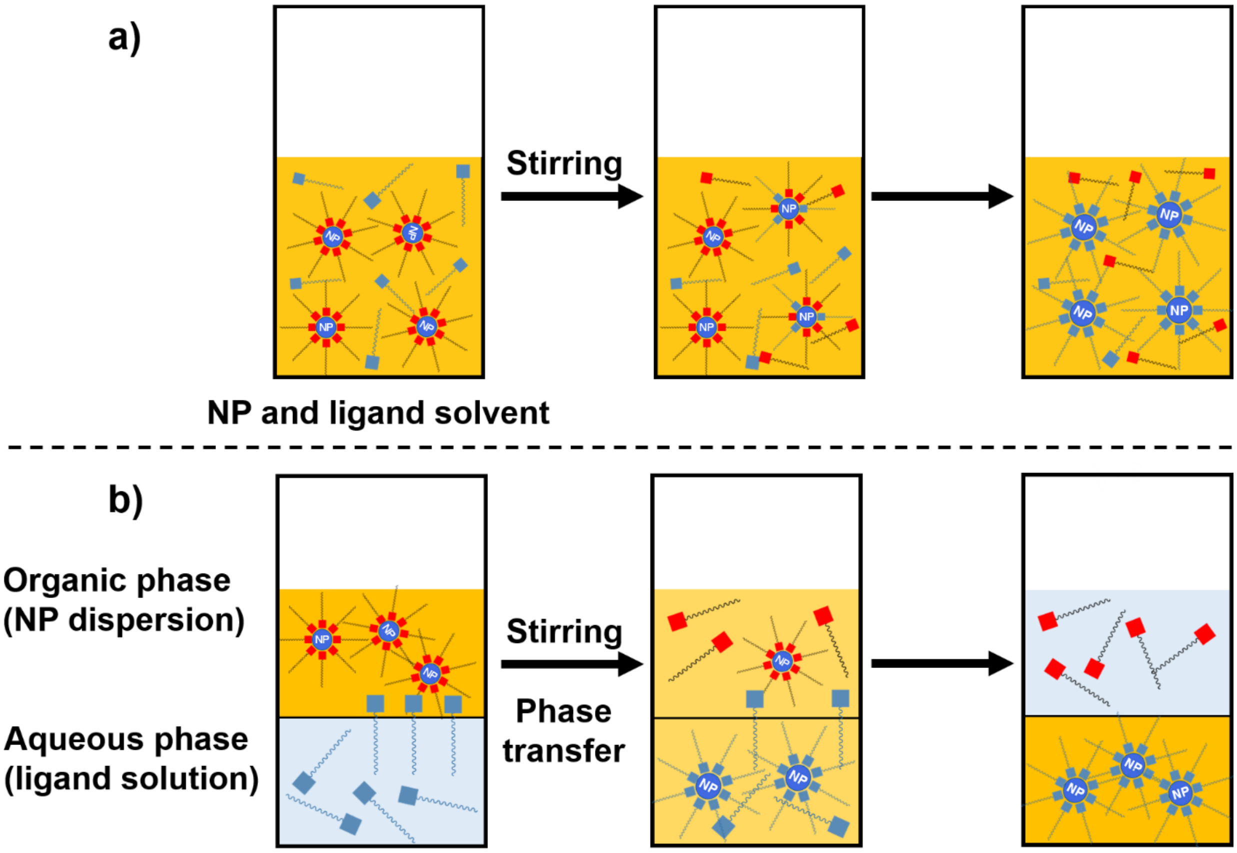

Figure 1-4. Ligand exchange in (a) single-phase system and (b) two-phase system.

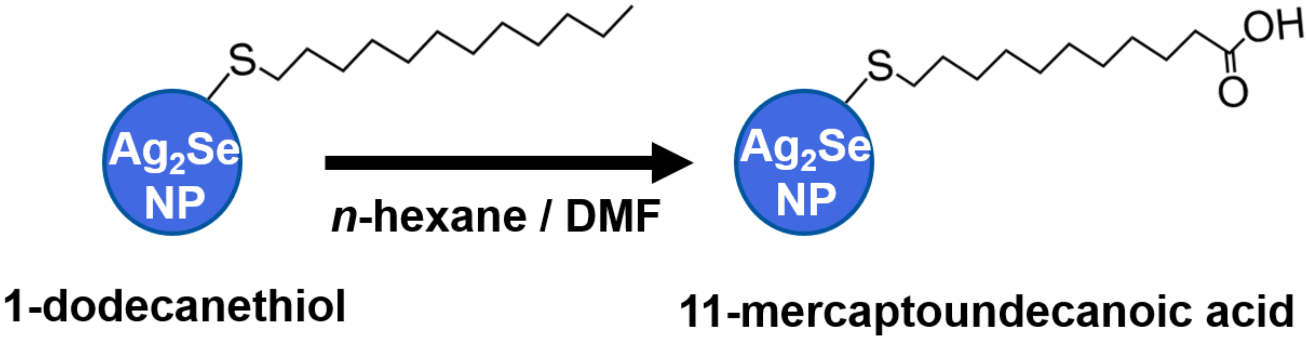

Figure 1-5. Ligand exchange from 1-dodecanethiol to 11-mercaptoundecanoic acid on the surface of Ag_2Se NPs in two-phase system [45].

1-1-3 Printed Electronics for Fine Metal Patterning

Printed electronics have attracted much interest for the fabrication of fine conductive metal patterns on flexible substrates. Recently, flexible electrodes are demanded for the development of flexible display and electronic paper. Moreover, ultra-fine metal patterns are required for the downsizing and lightening of electrical device [46]. The fine patterns are fabricated by conventional printing technology such as inkjet printing, gravure offset printing, and blade coating. In these methods, metal precursors (e.g. metal NP and metal salt) and catalysts are printed on the substrate, and then they are changed to the conductive metal pattern by the post-printing process. For example, the fabrication of fine metal pattern is performed by (1) electroless plating of the printed catalyst-pattern, (2) reduction of the printed metal salt-pattern, and (3) sintering of the printed metal NP-pattern.

The plating of metal is a traditional method for deposition of metal on the flexible substrate (Figure 1-6). In particular, the electroless plating of metal is widely applicable to various kinds of substrates (e.g. plastic substrates) [47-49]. First, a catalyst is printed on the substrate. Here, Pd NPs or its complex ions are generally used as catalysts. Second, the substrate is dipped into a plating aqueous solution containing a target metal ion and a reducing agent. A target metal ion is reduced by a reducing agent in the vicinity of the catalyst and a metal film is deposited electrolessly on the substrate. Finally, this substrate is dried and sintered. Generally, as plating metal films are densely packed, the conductivity of plating metal film is very close to that of bulk metal. Although the plating is a good candidate for printed electronics due to low-temperature process (≤ ~80 °C), it is difficult to fabricate ultra-fine patterns by this method.

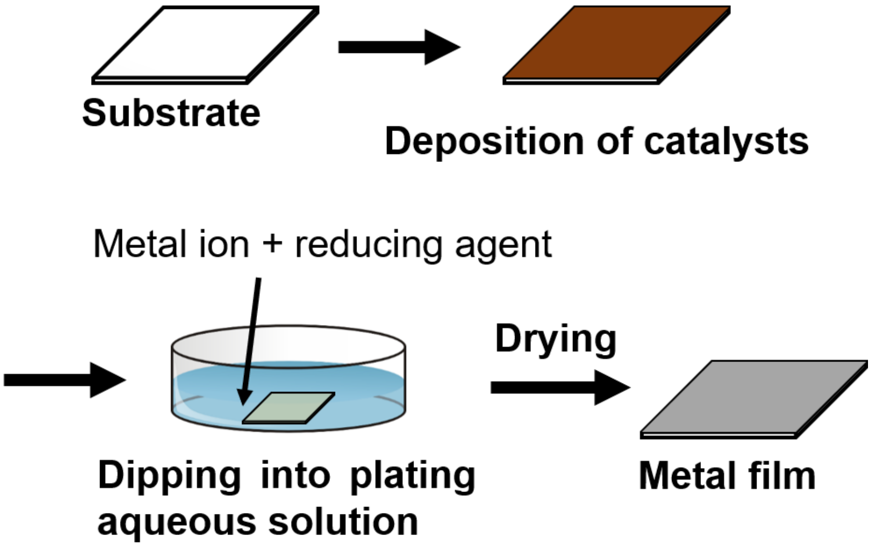

Figure 1-6. Fabrication of metal films by electroless plating.

The reduction of metal ion is performed by irradiating plasma or intense pulsed light to the printed metal salts or metal complexes (Figure 1-7) [57, 58]. The metal complexes are decomposed and reduced by the irradiation. The conductivity of obtained metal films comes up to the 50% value of bulk metal conductivity [58]. Generally, the bending resistance of fine metal patterns obtained by the reducing metal ion is significantly higher than that obtained by the electroless plating.

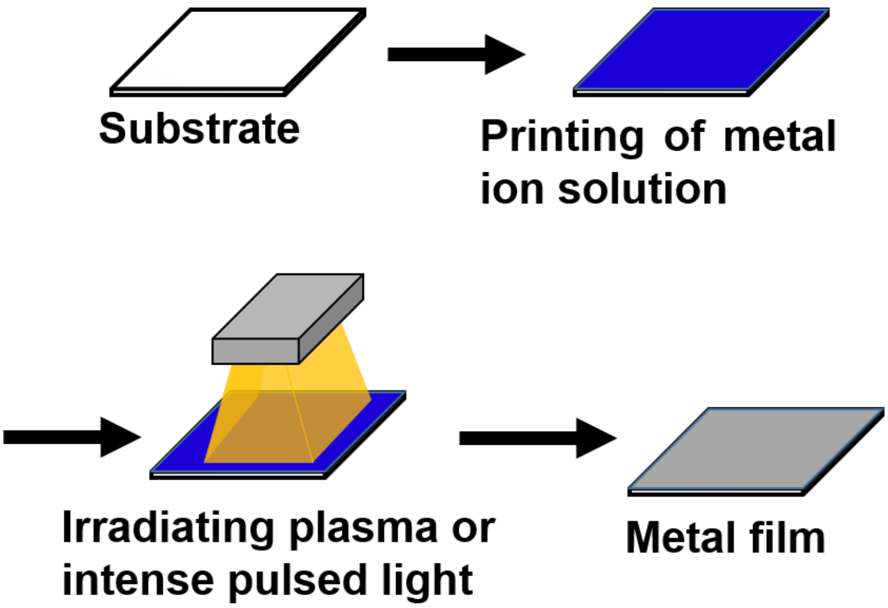

Figure 1-7. Fabrication of metal film by irradiating plasma or intense pulsed light to printed metal salt.

The other method is the deposition of conductive metal NPs. This method is based on the coalescence of metal NPs. As materials of metal NPs for conductive inks, Au [50], Ag [51], Cu [52], and Ni [53] are often used. Moreover, alloy metals are also used (e.g. Ag-Pd alloy NPs [54] and Cu-Ag core-shell NPs [55]). Among them, Ag is the most frequently adopted material for conductive ink and industrial products. Due to their high cost, Ag and other noble metals need to be replaced with cheaper metals such as Cu, Ni, and Al. The challenge in utilizing inexpensive metals such as Cu, Al, and Ni is developing, whereas they are easily oxidized in air due to the lower oxidation potential. A conductive film is obtained by the continuous coalescence of metal NPs (Figure 1-8). The obtained metal films have many voids due to the shape and misarrangement of metal NPs. The conductivity of obtained metal films comes up to the 60% value of bulk metal conductivity [56]. One of the advantages of coalescence of metal NPs is printing and sintering of multiple metal NP layers. In addition, the ligands on the surface of metal NPs should be removed for the effective coalescence of metal NPs after printing them on the substrate. Therefore, various physical sintering methods such as thermal treatment, microwave irradiation, plasma treatment, laser irradiation, and flash light irradiation have been developed so far for the fabrication of fine conductive metal patterns on the flexible substrate. Unfortunately, these methods often induce the damage and shrink of plastic substrates by locally heating based on electromagnetic irradiation. The shrinkage causes the resolution loss of fine patterning. Therefore, the coalescence of metal NPs under milder conditions is strongly desired. One of the candidates is RT chemical sintering.

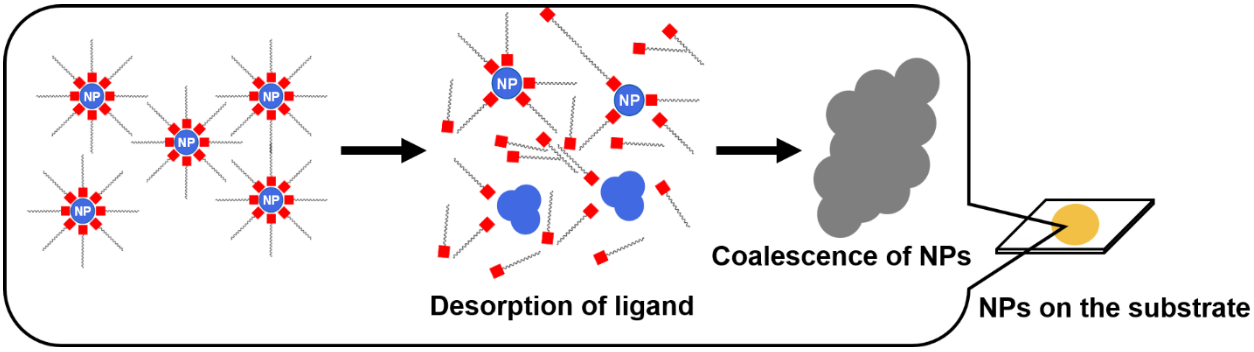

Figure 1-8. Fabrication of metal film by sintering of NPs.

Section 1-2: Sintering Technology of Metal NPs

1-2-1 Thermal Sintering

The various physical sintering of metal NPs for the fabricating fine metal patterns have been developed. The thermal sintering is the most traditional among the sintering processes [59-67]. Metal NPs generally melt and coalesce by heating. The heating is normally carried out in an electric furnace. There are two representative methods in the thermal sintering. Namely, they are the melting of metal NPs and the desorption of ligands (Figure 1-9).

Metal NPs have the advantage of melting-point depression as compared to their bulk metals. Melting-point depression is caused by the higher surface free energy based on the high surface-to-volume ratio. For example. the melting point of Ag NPs (diameter: 2.5 nm) is around 400 °C (bulk Ag: 962 °C) [17]. In the melting method (Figure 1-9a), a densely-packed metal film is obtained as the voids are filled with the melting metals. However, the sintering temperature is much higher than the glass transition temperature of commonplace plastic substrates.

On the other hand, the coalescence of metal NPs is also caused by the desorption or thermal decomposition of ligands (Figure 1-9). This desorption method is performed at lower temperature compared with the melting method. For example, Cu NPs were sintered at 80 °C under N_2 flow [64]. In this case, the conductivity of the Cu film was at most the 0.02 % value of bulk Cu conductivity (5.96×10^{7} S m^{-1} = 1.68×10^{-8} Ω m [68]). In this method, the sintering temperature is almost the same as the glass transition temperature of commonplace plastic substrates such as poly(ethylene terephthalate). Since NPs only coalesce each other, the voids generate (Figure 1-9b). As a result, the electrical resistivity of the metal film obtained by the desorption method is relatively higher compared with that obtained by the melting method.

In both cases, the damage and shrink of plastic substrates by heating are inevitable. Nevertheless, the thermal sintering is a major process in the industrial areas due to its large-scaling with ease.

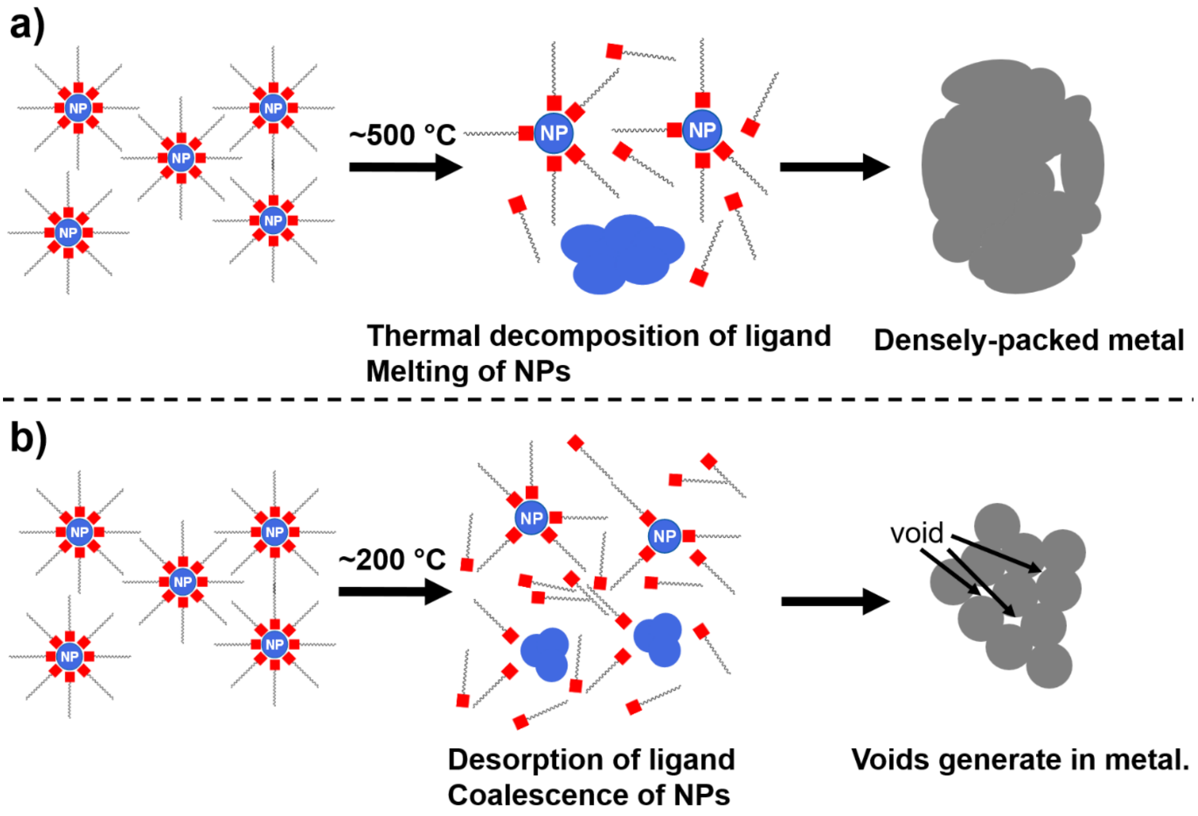

Figure 1-9. (a) Melting of NPs at high temperature (~500 °C) and (b) coalescence of NPs at low temperature (~200 °C) in the thermal sintering method.

1-2-2 Microwave Sintering

Metal NPs can also be sintered by microwave irradiation (Figure 1-10a) [69]. Metal NPs are locally heated by the vibration of free electrons caused by microwave (Figure 1-10b). However, the penetration depth of microwave radiation is very small (1~2 μm). Therefore, only the thin metal film can be obtained. The irradiation range of microwave is relatively wide. The conductivity comes up the 10-34 % value of bulk Ag conductivity (6.3×10^7 S m^{-1} = 1.6×10^{-8} Ω m, [68]) by irradiating and heating at 110 °C for 1-2 min [69]. Microwave sintering is often combined with other sintering processes such as thermal sintering and plasma sintering. Therefore, the damage and shrink of plastic substrates by heating often occur.

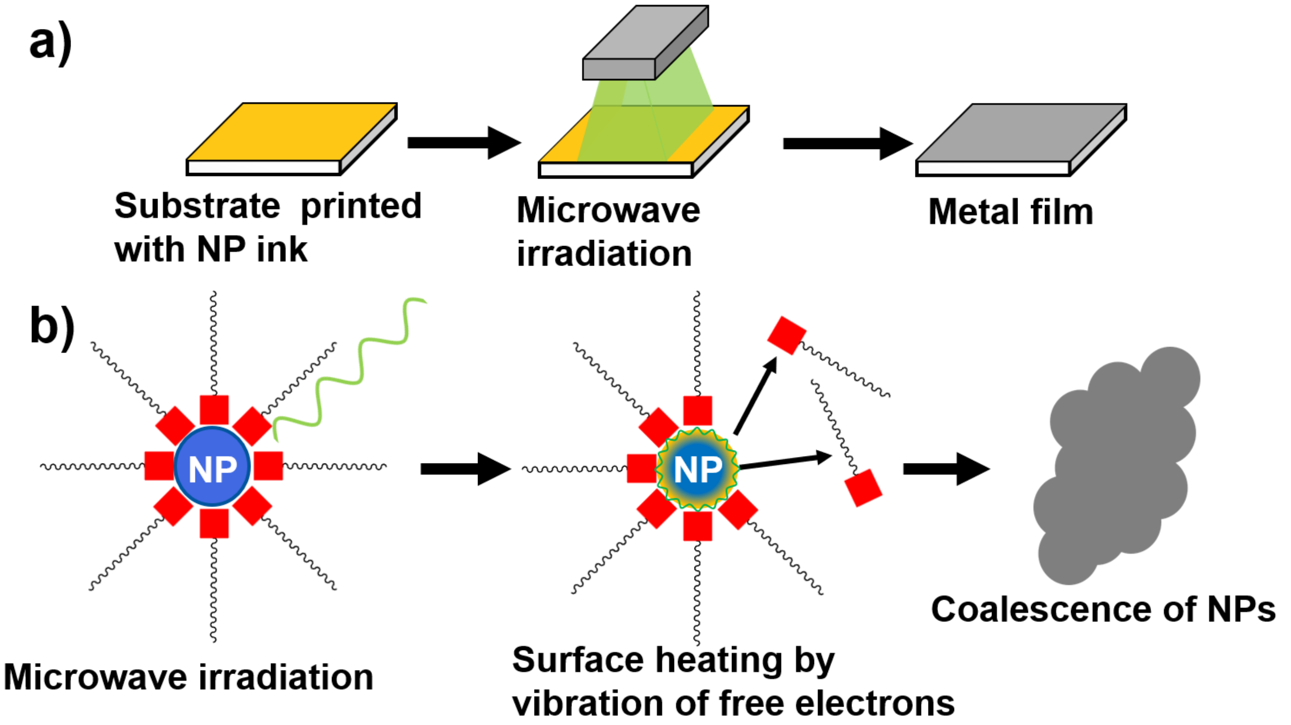

Figure 1-10. Illustration of (a) microwave sintering method and (b) coalescence process of metal NPs.

1-2-3 Plasma Sintering

Plasma sintering is generally performed by exposure of metal NPs to Ar plasma (Figure 1-11a) [56]. The sintering starts from the top layer of printed patterns (Figure 1-11b). Thus, if the plasma exposure time is not sufficient, the top layer can be easily peeled off by an adhesive tape. The conductivity of the obtained Ag thin film was the 40 % value of bulk Ag conductivity after 60 min exposure at 70 °C [56]. However, this approach requires the expensive and specific equipment.

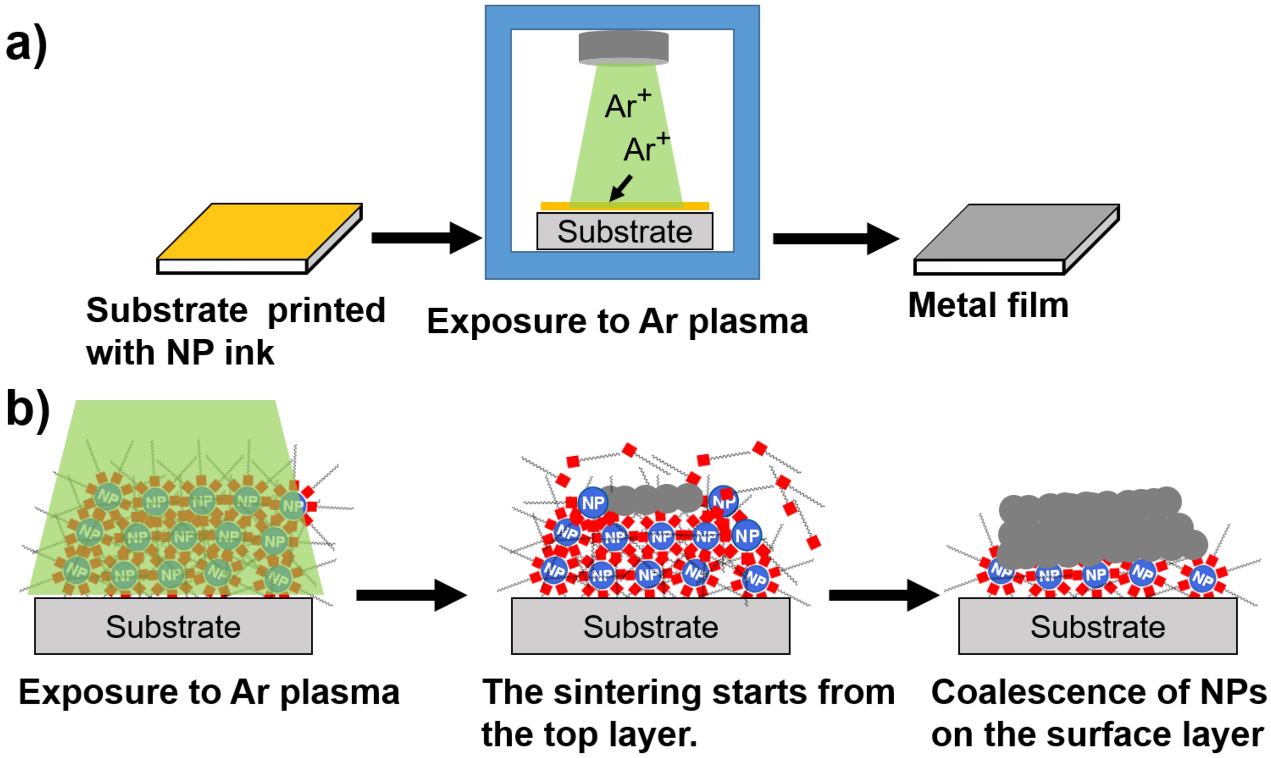

Figure 1-11. Illustration of (a) plasma sintering method and (b) coalescence process of metal NPs.

1-2-4 Laser Sintering

Laser sintering is a kind of photonic sintering. The sintering of metal NPs is performed at the spot irradiated with high energy-density light (continuous or pulsed laser operated in the visible light and infrared range) (Figure 1-12) [70-75]. The fine metal patterns are obtained with ease since laser can focus the spot with the extremely-small size. For example, the conductivity of the Ag line (line width: ~11 μm) was the 23 % value of bulk Ag conductivity by irradiating with 50 mW laser (scanning speed: 50 mm s^{-1}) [70]. The conductivity of metal thin films depends on the scanning speed of laser. If the scanning speed is too fast, the sintering of metal NPs is not sufficient. Therefore, this method is not suitable for large-scaling.

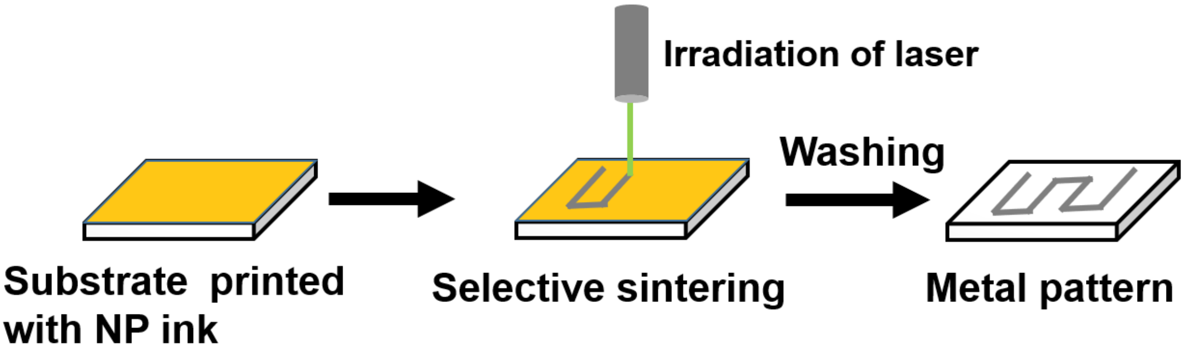

Figure 1-12. Illustration of laser sintering method.

1-2-5 Flash Light Sintering

Flash light sintering has attracted interest for rapid fabrication of fine metal patterns such as roll-to-roll manufacturing [76-80]. This method is performed by irradiating with high energy pulsed light for ≤ 100 ms using a xenon flash lamp (Figure 1-13). For example, conductive thin films were obtained from Cu NPs by irradiating with flash light (8 J cm^{-2}, 5 ms). The conductivity of this Cu film was the 24 % value of bulk Cu conductivity [77]. In this case, oxide shells of Cu NPs can be eliminated by the intermediate alcohol generated from the decomposition of poly(*N*-vinylpyrrolidone) under ambient conditions [77]. Generally, commonplace plastic substrates are damaged by heating. For example, the maximum temperature of the polyimide substrate irradiated with flash light (8 J cm^{-2}) was 274 °C [78].

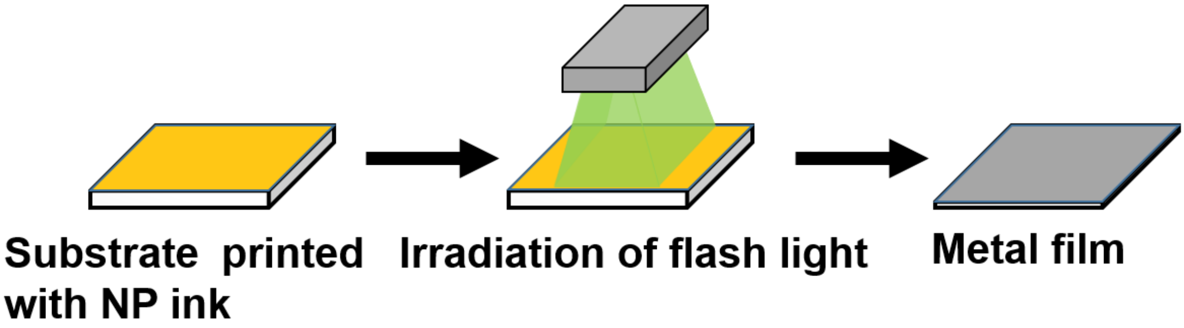

Figure 1-13. Illustration of flash light sintering method.

Section 1-3: Fabrication of Conductive Metal Films at Room-Temperature (RT)

1-3-1 Deposition of π-Junction Metal NPs

This method is performed by evaporating a solvent in the inks containing *π*-junction metal NPs. Kanehara *et al.* reported that Au electrodes were successfully fabricated by printing *π*-junction Au NPs at RT (~25 °C) [81, 82]. The conductivity of this electrode was the ~24 % value of bulk Au conductivity (4.42×10^7 S m^{-1} = 2.26×10^{-8} Ω m [68]). Here, Au NPs are capped by aromatic molecules having a large *π*-conjugated system as the conductive ligand. For example, 2,3,11,12,20,21,29,30-oktakis[2-(dimethylamino)ethylthio]naphthalocyanie (OTAN), is used as a large *π*-conjugated molecule (Figure 1-14). In these NPs, orbital hybridization between *π* orbitals of aromatic molecules and orbitals of metal core contributes to charge transport among metal NPs. Although this method is easy and useful for flexible electronics, printing and sintering of multiple metal NP layers is difficult.

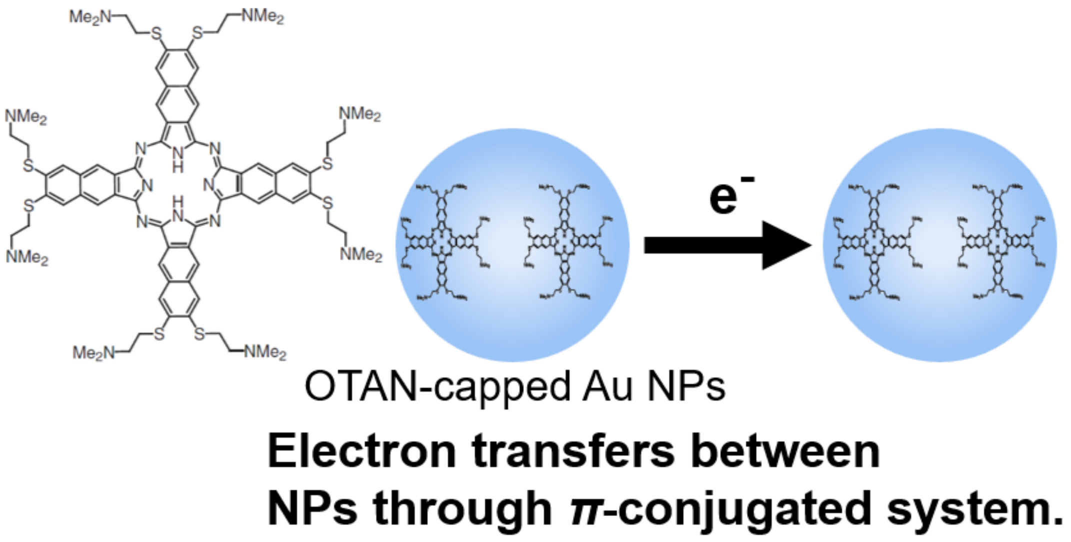

Figure 1-14. Illustration of deposition of *π*-junction metal NPs.

1-3-2 RT Chemical Sintering

The chemical sintering method is carried out by dipping into a solvent containing sintering agents at RT (Figure 1-15). This method is also called RT chemical sintering. In this method, sintering agents are used for the easy desorption of ligands from metal NPs. When ligands desorb from metal NP, metal NPs coalesce even at RT. The first achievement in this method is the Magdassi's report [83]. In that study, the conductive lines were prepared by depositing the aqueous dispersion of polypyrrole-capped Ag NPs on the glass substrate and RT sintering with $CaCl_2$. The conductivity of this line was the 14 % value of bulk Ag conductivity [83].

Chloride ion (by dipping into a solvent containing NaCl or exposing to a vapor such as HCl) [84-87] and hydroxide ion (by dipping into a solvent containing e.g., NaOH) [88] have been used as sintering agents for the RT chemical sintering of Ag NPs. The highest conductivity of the Ag film obtained by dipping into water containing Cl^- was the 41 % value of bulk Ag conductivity [85]. On the other hand, if the interaction between ligands and NPs is comparatively weak, sintering agents are not necessary for the desorption of ligands. Wakuda *et al*. reported that dodecylamine-capped Ag NPs could be sintered by dipping into methanol without a sintering agent [89, 90]. The conductivity of this Ag film was the 2.2 % value of bulk Ag conductivity [90].

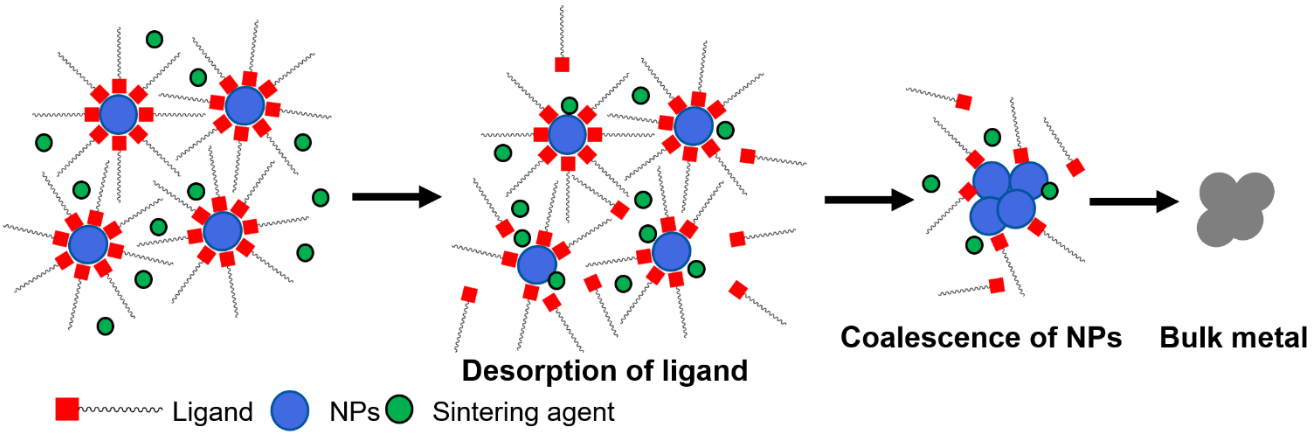

Figure 1-15. Illustration of RT chemical sintering method.

Section 1-4: Purpose of This Study

Although conductive metal films are obtained at RT, the conventional RT chemical sintering method has a problem that their conductivity is lower than that of the metal films obtained by sintering methods with more or less heating. In consideration of these backgrounds, the author aimed to develop a novel RT chemical sintering method by dipping metal NPs into an organic solvent containing a sintering agent in this thesis, because this method is easy, energy saving and applicable to the fabrication of flexible electrodes on commonplace plastic substrates. Conventionally, aqueous dispersion of metal NPs is used in the RT chemical sintering method. On the other hand, non-aqueous dispersion of metal NPs is better than aqueous dispersion in terms of easy viscosity control and stable solvent dispersion.

To the best of the author's knowledge, the RT chemical sintering in an organic solvent reported so far was only two examples. As mentioned in section 1-3-2, one is the study reported by Wakuda *et al* [89, 90]. However, Wakuda *et al.* did not use a sintering agent. The other is the study reported by Dai *et al* [91]. In that study, non-aqueous dispersion of 1-amino-2-propanol-capped Cu-Ag core-shell NPs (Cu@Ag NPs) was casted on the substrate and it was dipped into water containing NaOH as a sintering agent and $NaBH_4$ as a reducing agent at RT. In this case, the RT chemical sintering was not performed in organic solvents. Organic solvents allow for the use of various organic sintering agents. Therefore, the RT sintering of non-aqueous NP pastes with an organic solvent containing a sintering agent was investigated in detail in this study.

As the first step of this study, the interaction between ligands and metal NPs was systematically investigated under various conditions because the effect of ligands on the coalescence of metal NPs has not been sufficiently investigated yet. The investigation provides the optimal combination of ligand, sintering agent, and dipping solvent. The RT chemical sintering of Ag NPs, Cu@Ag NPs, and Pd NPs was performed in this thesis. Here, tri-*n*-octylphosphine oxide (TOPO), octanoic acid (OA), oleic acid, oleylamine and 1-dodecanethiol (DDT) were used as additive ligands. Their functional groups are well known as general adsorption moieties for metal nanoparticles. The coalescence of metal NPs was evaluated by crystallite sizes, the amount of ligand on the surface of NPs, and electron microscopic images. The crystal reconstruction and growth in the neck-like region of coalesced NPs was due to the surface diffusion of atoms. This is why coalescence of metal NPs causes the increase in crystallite size.

As the second step, the metal thin films were fabricated under the optimal conditions determined in the first step. The properties of metal thin films obtained by the RT chemical sintering method were examined. In particular, conductivity and catalytic ability were investigated.

The purpose of this study is to establish the RT chemical sintering method of metal NPs with an organic solvent containing a sintering agent. This study helps to clarify the coalescence behavior of metal NPs in an organic solvent containing a sintering agent. Therefore, the author expects that this sintering method would be adopted to the effective coalescence of various kinds of metal NPs.

Section 1-5: Composition of This Thesis

This thesis is constructed for the purpose described in the section 1-4. As for non-aqueous pastes of Ag NPs, Cu@Ag NPs, and Pd NPs, the RT chemical sintering was performed with an organic solvent containing a sintering agent. In this thesis, the coalescence behavior of metal NPs in an organic solvent and the properties of their precipitates were investigated.

In Chapter 1, general information of metal NPs and printed electronics was described for understanding this research deeply. Furthermore, various sintering methods of metal NPs developed so far were introduced.

In Chapter 2, the RT chemical sintering of Ag NPs was performed in an organic solvent containing a sintering agent. The experimental conditions such as sintering agent, dipping time, dipping solvent, and ligand of Ag NPs were examined for optimizing the coalescence of Ag NPs. Finally, the conductivity of the obtained metal thin films was examined.

In Chapter 3, the RT chemical sintering of Cu@Ag NPs was performed in an organic solvent containing a sintering agent and/or a reducing agent. Aiming at the application to conductive nanoinks having migration and oxidation resistance, oleylamine- and oleic-acid-capped Cu@Ag NPs were synthesized and their coalescence behavior was investigated in an organic solvent. The experimental conditions such as sintering agent, reducing agent, and ligand of Cu@Ag NP were examined for optimizing the coalescence of Cu@Ag NPs. Finally, the conductivity of the obtained metal thin films was examined.

In Chapter 4, the RT chemical sintering of Pd NPs was performed in an organic solvent containing a sintering agent for the fabrication of porous Pd structures. The experimental conditions such as sintering agent and organic sacrificial template were examined for optimizing the coalescence of Pd NPs. Furthermore, catalytic activities of porous Pd structure were evaluated using the Suzuki coupling reaction.

Reference

[1] Rao, J. P.; Geckeler, K. E. Polymer nanoparticles: Preparation techniques and size-control parameters. *Prog. Polym. Sci.* **2011**, *36*, 887–913.

[2] Deirram, N.; Zhang, C.; Kermaniyan, S. S.; Johnston, A. P. R.; Such, G. K. pH-responsive polymer nanoparticles for drug delivery. *Macromol. Rapid Commun.* **2019**, *40*, 1800917.

[3] Nakahara, Y.; Takeuchi, T.; Yokoyama, S.; Kimura, K. Quantitative ^{1}H NMR analysis of reacted silanol groups in silica nanoparticles chemically modified with monochlorosilanes. *Surf. Interface Anal.* **2011**, *43*, 809–815.

[4] Zhang, W.-H.; Hu, X.-X.; Zhang, X.-B. Dye-doped fluorescent silica nanoparticles for live cell and in vivo bioimaging. *Nanomaterials* **2016**, *6*, 81–97.

[5] Gubala, V.; Giovannini, G.; Kunc, F.; Monopoli, M. P.; Moore, C. J. Dye-doped silica nanoparticles: synthesis, surface chemistry and bioapplications. *Cancer Nanotechnol.* **2020**, *11*, 1.

[6] Nakahara, Y.; Nakajima, Y.; Okada, S.; Miyazaki, J.; Yajima, S. Synthesis of silica nanoparticles with physical encapsulation of near-infrared fluorescent dyes and their tannic acid coating. *ACS Omega* **2021**, *6*, 17651–17659.

[7] Farrell, Z. J.; Thrasher, C. J.; Flynn, A. E.; Tabor, C. E. Silanized liquid-metal nanoparticles for responsive electronics. *ACS Appl. Nano Mater.* **2020**, *3*, 6297–6303.

[8] Kalhapure, R. S.; Akamanchi, K. G.; Mocktar, C.; Govender, T. Synthesis and antibacterial activity of silver nanoparticles capped with a carboxylic acid-terminated generation 1 Oleodendrimer. *Chem. Lett.* **2014**, *43*, 1110–1112.

[9] Kyaw, K.; Harada, A.; Ichimaru, H.; Kawagoe, T.; Yahiro, K.; Morimura, S.; Ono, K.; Tsutsuki, H.; Sawa, T.; Niidome, T. Silver nanoparticles as potential antibiofilm agents against human pathogenic bacteria. *Chem. Lett.* **2017**, *46*, 594–596.

[10] Bhanumathi, R.; Manivannan, M.; Thangaraj, R.; Kannan, S. Drug-carrying capacity and anticancer effect of the folic acid- and berberine-loaded silver nanomaterial to regulate the AKT-ERK pathway in breast cancer.

ACS Omega **2018**, *3*, 8317–8328.

[11] Song, D. H.; Kim, H.-Y.; Kim, H.-S.; Suh, J. S.; Jun, B.-H.; Rho, W.-Y. Preparation of plasmonic monolayer with Ag and Au nanoparticles for dye-sensitized solar cells. *Chem. Phys. Lett.* **2017**, *687*, 152–157.

[12] Tan, H.; Santbergen, R.; Smets, A. H. M.; Zeman, M. Plasmonic light trapping in thin-film silicon solar cells with improved self-assembled silver nanoparticles. *Nano Lett.* **2012**, *12*, 4070–4076.

[13] Gao, C.; Lyu, F.; Yin Y. Encapsulated metal nanoparticles for catalysis. *Chem. Rev.* **2021**, *121*, 834–881.

[14] Sherry, L. J.; Chang, S.-H.; Schatz, G. C.; Duyne, R. P. V. Localized surface plasmon resonance spectroscopy of single silver nanocubes. *Nano Lett.* **2005**, *5*, 2034–2038.

[15] Wiley, B. J.; Im, S. H.; Li, Z.-Y.; Mclellan, J.; Siekkinen, A.; Xia, Y. Maneuvering the surface plasmon resonance of silver nanostructures through shape-controlled synthesis. *J. Phys. Chem. B* **2006**, *110*, 15666–15675.

[16] Aherne, D.; Ledwith, D. M.; Gara, M.; Kelly, J. M. Optical properties and growth aspects of silver nanoprisms produced by a highly reproducible and rapid synthesis at room temperature. *Adv. Funct. Mater.* **2008**, *18*, 2005–2016.

[17] Sun, Q.; Yu, H.; Ueno, K.; Kubo, A.; Matsuo, Y.; Misawa, H. Dissecting the few-femtosecond dephasing time of dipole and quadrupole modes in gold nanoparticles using polarized photoemission electron microscopy. *ACS Nano.* **2016**, *10*, 3835–3842.

[18] Kado, S.; Yokomine, S.; Kimura, K. Widely tunable plasmon resonances from visible to near-infrared of hollow silver nanoshells. *Bull. Chem. Soc. Jpn.* **2017**, *90*, 537–545.

[19] Buffat, Ph.; Borel, J-P. Size effect on the melting temperature of gold particles. *Phys. Rev. A* **1976**, *13*, 2287–2298.

[20] Xu, R.; Wang, D.; Zhang, J.; Li, Y. Shape-dependent catalytic activity of silver nanoparticles for the oxidation of styrene. *Chem. Asian J.* **2006**, *1*, 888–893.

[21] Zhou, X.; Xu, W.; Liu, G.; Panda, D.; Chen, P. Size-dependent catalytic activity and dynamics of gold

nanoparticles at the single-molecule level. *J. Am. Chem. Soc.* **2010**, *132*, 138–146.

[22] Ferrera, M.; Valle, G. D.; Sygletou, M.; Magnozzi, M.; Catone, D.; O'Keeffe, P.; Paladini, A.; Toschi, F.; Mattera, L.; Canepa, M.; Bisio, B. Thermometric calibration of the ultrafast relaxation dynamics in plasmonic Au nanoparticles. *ACS Photonics* **2020**, *7*, 959–966.

[23] Lu, J.; Guo, J.; Song, S.; Yu, G.; Liu, H.; Yang, X.; Lu, Z. Preparation of Ag nanoparticles by spark ablation in gas as catalysts for electrocatalytic hydrogen production. *RSC Adv.* **2020**, *10*, 38583–38587.

[24] Plodinec, M.; Nerl, H. C.; Girgsdies, F.; Schlögl, R.; Lunkenbein, T. Insights into chemical dynamics and their impact on the reactivity of Pt nanoparticles during CO oxidation by operando TEM. *ACS Catal.* **2020**, *10*, 3183–3193.

[25] Chen, D.; Yang, W.; Jiao, L.; Li, L.; Yu, S.-H.; Jiang, H.-L. Boosting catalysis of Pd nanoparticles in MOFs by pore wall engineering: the roles of electron transfer and adsorption energy. *Adv. Mater.* **2020**, *32*, 2000041.

[26] Reske, R.; Mistry, H.; Behafarid, F.; Cuenya, B. R.; Strasser, P. Particle size effects in the catalytic electroreduction of CO_2 on Cu nanoparticles. *J. Am. Chem. Soc.* **2014**, *136*, 6978–6986.

[27] Dash, A.; Blasiak, B.; Tomanek, B.; Banerjee, A.; Trudel, S.; Latta, P.; van Veggel, F. C. J. M. Colloidally stable monodisperse Fe nanoparticles as T_2 contrast agents for high-field clinical and preclinical magnetic resonance imaging. *ACS Appl. Nano Mater.* **2021**, *4*, 1235–1242.

[28] Shin, H.; Oh, S.; Jun, H.; Oh, M. Porous composites embedded with Cu and Co nanoparticles for efficient catalytic reduction of 4-nitrophenol. *Bull. Korean Chem. Soc.* **2021**, *42*, 303–308.

[29] Kumar, R.; Kumar, A.; Verma, N.; Khopkar, V.; Philip, R.; Sahoo, B. Ni nanoparticles coated with nitrogen-doped carbon for optical limiting applications. *ACS Appl. Nano Mater.* **2020**, *3*, 8618–8631.

[30] Cui, Y.; Huang, D.; Li, Y.; Huang, W.; Liang, Z.; Xu, Z.; Zhao, S. Aluminum nanoparticles synthesized by a novel wet chemical method and used to enhance the performance of polymer solar cells by the plasmonic effect. *J. Mater. Chem. C* **2015**, *3*, 4099–4103.

[31] Wang, L.; Kafshgari, M. H.; Meunier, M. Optical properties and applications of plasmonic-metal nanoparticles.

Adv. Funct. Mater. **2020**, *30*, 2005400.

[32] Reier, T.; Oezaslan, M.; Strasser, P. Electrocatalytic oxygen evolution reaction (OER) on Ru, Ir, and Pt catalysts: a comparative study of nanoparticles and bulk materials. *ACS Catal.* **2012**, *2*, 1765–1772.

[33] Dong, P.; Fisher, E. A.; Meli, M.-V.; Trudel, S. Tuning the magnetism of gold nanoparticles by changing the thiol coating. *Nanoscale* **2020**, *12*, 19797–19803.

[34] Yamamoto, M.; Kashiwagi, Y.; Nakamoto, M. Size-controlled synthesis of monodispersed silver nanoparticles capped by long-chain alkyl carboxylates from silver carboxylate and tertiary amine. *Langmuir* **2006**, *22*, 8581–8586.

[35] Chen, M.; Feng, Y.-G.; Wang, X.; Li, T.-C.; Zhang, J.-Y.; Qian, D.-J. Silver nanoparticles capped by oleylamine: formation, growth, and self-organization. *Langmuir* **2007**, *23*, 5296–5304.

[36] Son, S. U.; Jang, Y.; Yoon, K. Y.; Kang, E.; Hyeon, T. Facile synthesis of various phosphine-stabilized monodisperse palladium nanoparticles through the understanding of coordination chemistry of the nanoparticles. *Nano Lett.* **2004**, *4*, 1147–1151.

[37] Saponjic, Z. D.; Csencsits, R.; Rajh, T.; Dimitrijevic, N. M. Self-assembly of TOPO-derivatized silver nanoparticles into multilayered film. *Chem. Mater.* **2003**, *15*, 4521–4526.

[38] Ienaga, T.; Nakahara, Y.; Yajima, S.; Kimura, K. Effect of protective agents on silver nanoparticle preparation by vacuum evaporation on running hydrocarbon solution. *J. Nanosci. Nanotechnol.* **2018**, *18*, 2547–2554.

[39] Ienaga, T.; Okada, S.; Nakahara, Y.; Watanabe, M.; Tamai, T.; Yajima, S.; Kimura, K. Comparison of physical adsorption strength of protective agents via ligand exchange of silver nanoparticles prepared by vacuum evaporation on running oil substrate. *Bull. Chem. Soc. Jpn.* **2017**, *90*, 1251–1258.

[40] Brown, L. O.; Hutchison, J. E. Controlled growth of gold nanoparticles during ligand exchange. *J. Am. Chem. Soc.* **1999**, *121*, 882–883.

[41] Keum, C.-D.; Ishii, N.; Michioka, K.; Wulandari, P.; Tamada, K.; Furusawa, M.; Fukushima, H. A gram scale synthesis of monodispersed silver nanoparticles capped by carboxylates and their ligand exchange. *J.*

Nonlinear Opt. Phys. Mater. **2008**, *17*, 131–142.

[42] Liu, Y.; Wang, C.; Wei, Y.; Zhu, L.; Li, D.; Jiang, J. S.; Markovic, N. M.; Stamenkovic, V. R.; Sun, S. Surfactant-induced postsynthetic modulation of Pd nanoparticle crystallinity. *Nano Lett.* **2011**, *11*, 1614–1617.

[43] Ansar, S. M.; Mohammed, F. S.; von White, G.; Budi, M.; Powell, K. C.; Mefford, O. T.; Kitchens, C. L. Effect of postsynthesis purifications on gold and silver nanoparticle ligand coverage. *J. Phys. Chem. C* **2016**, *120*, 6842–6850.

[44] Dong, A.; Ye, X.; Chen, J.; Kang, Y.; Gordon, T.; Kikkawa, J. M.; Murray, C. B. A Generalized ligand-exchange strategy enabling sequential surface functionalization of colloidal nanocrystals. *J. Am. Chem. Soc.* **2011**, *133*, 998–1006.

[45] Nakahara, Y.; Kunitsu, Y.; Ozaki, N.; Tanaka, M.; Yajima, S. Preparation of Ag_2Se QDs with excellent aqueous dispersion stability by organic coating with aqueous ATRP. *Polym. Bull.* **2019**, *76*, 4753–4768.

[46] Wang, P.; Hu, M.; Wang, H. Chen, H.; Feng, Y.; Wang, J.; Ling, W.; Huang, Y. The evolution of flexible electronics: from nature, beyond nature, and to nature. *Adv. Sci.* **2020**, *7*, 2001116.

[47] Ma, S.; Liu, L.; Bromberg, V.; Singler, T. J. Electroless copper plating of inkjet-printed polydopamine nanoparticles: a facile method to fabricate highly conductive patterns at near room temperature. *ACS Appl. Mater. Interfaces.* **2014**, *6*, 19494–19498.

[48] Tamai, T.; Watanabe, M.; Kobayashi, Y.; Nakahara, Y.; Yajima, Surface modification of PEN and PET substrates by plasma treatment and layer-by-layer assembly of polyelectrolyte multilayer thin films and their application in electroless deposition. *RSC Adv.* **2017**, *7*, 33155–33161.

[49] Tamai, T.; Watanabe, M.; Kobayashi, Y.; Kobata, J.; Nakahara, Y.; Yajima, Surface modification of PEN and PET substrates by plasma treatment and layer-by-layer assembly of polyelectrolyte multilayer thin films and their application in electroless deposition. *Colloids Surf., A* **2019**, *575*, 230–236.

[50] Wu, Y.; Li, Y.; Liu, P.; Gardner, S.; Ong, B. S. Studies of gold nanoparticles as precursors to printed conductive features for thin-film transistors. *Chem. Mater.* **2006**, *18*, 4627–4632.

[51] Wang, F.; Nie, N.; He, H.; Tang, Z.; Chen, Z.; Zhu, W. Ultrasonic-assisted sintering of silver nanoparticles for flexible electronics. *J. Phys. Chem. C* **2017**, *121*, 28515–28519.

[52] Dai, X.; Zhang, T.; Shi, H.; Zhang, Y.; Wang, T. Reactive sintering of Cu nanoparticles at ambient conditions for printed electronics. *ACS Omega* **2020**, *5*, 13416–13423.

[53] Park, S.-H.; Kim, H.-S. Flash light sintering of nickel nanoparticles for printed electronics. *Thin solid Films* **2014**, *550*, 575–581.

[54] Yamamoto, M.; Kakiuchi, H.; Kashiwagi, Y.; Yoshida, Y.; Ohno, T.; Nakamoto, M. Synthesis of Ag–Pd alloy nanoparticles suitable as precursors for ionic migration-resistant conductive film. *Bull. Chem. Soc. Jpn.* **2010**, *83*, 1386–1391.

[55] Yu, X.; Li, J.; Shi, T.; Cheng, C.; Liao, G.; Fan, J.; Li, T.; Tang, Z. A green approach of synthesizing of Cu-Ag core-shell nanoparticles and their sintering behavior for printed electronics. *J. Alloys Compd.* **2017**, *724*, 365–372.

[56] Perelaer, J.; Jani, R.; Grouchko, M.; Kamyshny, A.; Magdassi, S.; Schubert, U. S. Plasma and microwave flash sintering of a tailored silver nanoparticle ink, yielding 60% bulk conductivity on cost-effective polymer foils. *Adv. Mater.* **2012**, *24*, 3993–3998.

[57] Knapp, C. E.; Chemin, J.-B.; Douglas, S. P.; Ondo, D. A.; Guillot, J.; Choquet, P.; Boscher, N. D. Room-temperature plasma-assisted inkjet printing of highly conductive silver on paper. *Adv. Mater. Technol.* **2018**, 1700326.

[58] Wang, B.-Y.; Yoo, T.-H.; Song, Y.-W.; Lim, D.-S.; Oh, Y.-J. Cu ion ink for a flexible substrate and highly conductive patterning by intensive pulsed light sintering. *ACS Appl. Mater. Interfaces.* **2013**, *5*, 4113–4119.

[59] Zhang, Y.; Zhu, P.; Li, Gang; Zhao, T.; Fu, X.; Sun, R.; Zhou, F.; Wong, C.-P. Facile preparation of monodisperse, impurity-free, and antioxidation copper nanoparticles on a large scale for application in conductive ink. *ACS Appl. Mater. Interfaces.* **2014**, *6*, 560–567.

[60] Yang, H.-J.; He, S.-Y.; Chen, H.-L.; Tuan, H.-Y. Monodisperse copper nanocubes: synthesis, self-assembly,

and large-area dense-packed films. *Chem. Mater.* **2014**, *26*, 1785–1793.

[61] Hokita, Y.; Kanzaki, M.; Sugiyama, T.; Arakawa, R.; Kawasaki, H. High-concentration synthesis of sub-10-nm copper nanoparticles for application to conductive nanoinks. *ACS Appl. Mater. Interfaces.* **2015**, *7*, 19382–19389.

[62] Liu, J.; Chen, H.; Ji, H.; Li, M. Highly Conductive Cu–Cu joint formation by low-temperature sintering of formic acid-treated Cu nanoparticles. *ACS Appl. Mater. Interfaces.* **2016**, *8*, 33289–33298.

[63] Yokoyama, S.; Motomiya, K.; Takahashi, H.; Tohji, K. Green synthesis of Cu micro/nanoparticles for low-resistivity Cu thin films using ascorbic acid in aqueous solution. *J. Mater. Chem. C* **2016**, *4*, 7494–7500.

[64] Kanzaki, M.; Kawaguchi, Y.; Kawasaki, H. Fabrication of conductive copper films on flexible polymer substrates by low-temperature sintering of composite Cu ink in air. *ACS Appl. Mater. Interfaces.* **2017**, *9*, 20852–20858.

[65] Kamikoriyama, Y.; Imamura, H.; Muramatsu, A.; Kanie, K. Ambient aqueous-phase synthesis of copper nanoparticles and nanopastes with low-temperature sintering and ultra-high bonding abilities. *Sci. Rep.* **2019**, *9*, 899.

[66] Lee, C.; Kim, N. R.; Koo, J.; Lee, Y. J.; Lee, H. M. Cu-Ag core-shell nanoparticles with enhanced oxidation stability for printed electronics. *Nanotechnology* **2015**, *26*, 455601.

[67] Tian, Y.; Jiang, Z.; Wang, C.; Ding, S.; Wen, J.; Liu, Z.; Wang, C. Sintering mechanism of the Cu–Ag core–shell nanoparticle paste at low temperature in ambient air. *RSC Adv.* **2016**, *6*, 91783–91790.

[68] Kamyshny, A.; Magdassi, S. Conductive nanomaterials for printed electronics. *Small* **2014**, *10*, 3515–3535.

[69] Jung, S.; Chun, S. J.; Shon, C.-H. Rapid cellulose-mediated microwave sintering for high-conductivity Ag patterns on paper. *ACS Appl. Mater. Interfaces* **2016**, *8*, 20301–20308.

[70] Hong, S.; Yeo, J.; Kim, G.; Kim, D.; Lee, H.; Kwon, J.; Lee, H.; Lee, P.; Ko, S. H. Nonvacuum, maskless fabrication of a flexible metal grid transparent conductor by low-temperature selective laser sintering of nanoparticle ink. *ACS Nano* **2013**, *7*, 5024–5031.

[71] Lee, D.; Paeng, D.; Park, H. K.; Grigoropoulos, C. P. Vacuum-Free, Maskless patterning of Ni electrodes by laser reductive sintering of NiO nanoparticle ink and its application to transparent conductors. *ACS Nano* **2014**, *8*, 9807–9814.

[72] Suh, Y. D.; Kwon, J.; Lee, J.; Lee, H.; Jeong, S.; Kim, D.; Cho, H.; Yeo, J.; Ko, S. H. Maskless fabrication of highly robust, flexible transparent Cu conductor by random crack network assisted Cu nanoparticle patterning and laser sintering. *Adv. Electron. Mater.* **2016**, *2*, 1600277.

[73] Kwon, J.; Cho, H.; Eom, H.; Lee, H.; Suh, Y. D.; Moon, H.; Shin, J.; Hong, S.; Ko, S. H. Low-temperature oxidation-free selective laser sintering of Cu nanoparticle paste on a polymer substrate for the flexible touch panel applications. *ACS Appl. Mater. Interfaces.* **2016**, *8*, 11575–11582.

[74] Balliu, E.; Andersson, H.; Engholm, M.; Öhlund, T.; Nilsson, H.-E.; Olin, H. Selective laser sintering of inkjet-printed silver nanoparticle inks on paper substrates to achieve highly conductive patterns. *Sci. Rep.* **2018**, *8*, 10408.

[75] Ahn, H.-S.; Oh, A.-S.; Kim, D.-H.; Choi, Y.; Kim, K.-H.; Bae, H.-C. Fabrication of Cu wiring touch sensor via laser sintering of Cu nano/microparticle paste on 3D-printed substrate. *Adv. Eng. Mater.* **2021**, *23*, 2000688.

[76] Joo, S.-J.; Park, S.-H.; Moon, C.-J.; Kim, H.-S. A highly reliable copper nanowire/nanoparticle ink pattern with high conductivity on flexible substrate prepared via a flash light-sintering technique. *ACS Appl. Mater. Interfaces.* **2015**, *7*, 5674–5684.

[77] Hwang, Y.-T.; Chung, W.-H.; Jang, Y.-R.; Kim, H.-S. Intensive plasmonic flash light sintering of copper nanoinks using a band-pass light filter for highly electrically conductive electrodes in printed electronics. *ACS Appl. Mater. Interfaces.* **2016**, *8*, 8591–8599.

[78] Son, Y.-H.; Jang, J.-Y.; Kang, M. K.; Ahn, S.; Lee, C. S. Application of flash-light sintering method to flexible inkjet printing using anti-oxidant copper nanoparticles. *Thin solid Films* **2018**, *656*, 61–67.

[79] Dai, X.; Xu, W.; Zhang, T.; Wang, T. Self-reducible Cu nanoparticles for conductive inks. *Ind. Eng. Chem. Res.* **2018**, *57*, 2508–2516.

[80] Hwang, H.-J.; Malhotra, R. Shape-tuned junction resistivity and self-damping dynamics in intense pulsed light sintering of silver nanostructure films. *ACS Appl. Mater. Interfaces.* **2019**, *11*, 3536–3546.

[81] Kanehara, M.; Takeya, J.; Uemura, T.; Murata, H.; Takimiya, K.; Sekine, H.; Teranishi, T. Electroconductive π-junction Au nanoparticles. *Bull. Chem. Soc. Jpn.* **2012**, *85*, 957–961.

[82] Minari, T.; Kanehara, Y.; Liu, C.; Sakamoto, K.; Yasuda, T.; Yaguchi, A.; Tsukada, S.; Kashizaki, K.; Kanehara, M. Room-temperature printing of organic thin-film transistors with π-junction gold nanoparticles. *Adv. Funct. Mater.* **2014**, *24*, 4886–4892.

[83] Magdassi, S.; Michael, G.; Toker, D.; Kamyshny, A.; Balberg, I.; Millo, O. Ring stain effect at room temperature in silver nanoparticles yields high electrical conductivity. *Langmuir.* **2005**, *21*, 10264–10267.

[84] Magdassi, S.; Grouchko, M.; Berezin, O.; Kamyshny, A. Triggering the sintering of silver nanoparticles at room temperature. *ACS Nano* **2010**, *4*, 1943–1948.

[85] Grouchko, M.; Kamyshny, A.; Mihailescu, C. F.; Anghel, D. F.; Magdassi, S. Conductive inks with a “Built-In” mechanism that enables sintering at room temperature. *ACS Nano* **2011**, *5*, 3354–3359.

[86] Shi, L.; Layani, M.; Cai, X.; Zhao, H.; Magdassi, S.; Lan, M. An inkjet printed Ag electrode fabricated on plastic substrate with a chemical sintering approach for the electrochemical sensing of hydrogen peroxide. *Sensors and Actuators B* **2018**, *256*, 938–945.

[87] Peng, P.; Li, L.; Guo, W.; Hui, Z.; Fu, J.; Jin, C; Liu, Y.; Zhu, Y. Room-temperature joining of silver nanoparticles using potassium chloride solution for flexible electrode application. *J. Phys. Chem. C* **2018**, *122*, 2704–2711.

[88] Xiao, Y.; Zhang, Z. H.; Yang, M.; Yang, H. F.; Li, M. Y.; Cao, Y. The effect of NaOH on room-temperature sintering of Ag nanoparticles for high-performance flexible electronic application. *Materials Letters* **2018**, *222*, 16–20.

[89] Wakuda, D.; Hatamura, M.; Suganuma, K. Novel method for room temperature sintering of Ag nanoparticle paste in air. *Chem. Phys. Lett.* **2007**, *441*, 305–308.

[90] Wakuda, D.; Kim, K.; Suganuma, K. Room-temperature sintering of Ag nanoparticles paste. *IEEE Trans. Compon., Packag. Technol.* **2009**, *32*, 627–632.

[91] Dai, X.; Xu, W.; Zhang, T.; Shi, H.; Wang, T. Room temperature sintering of Cu-Ag core-shell nanoparticles conductive inks for printed electronics. *Chem. Eng. J.* **2019**, *364*, 310–319.

Chapter 2: RT Chemical Sintering of Ag NPs and Their Conductivity

Section 2-1: Introduction

Printed electronics have recently been drawing many people's attention from a viewpoint of applications to wearable device and flexible display [1]. In printed electronics, particularly, Ag NPs are highly expected as nanoinks for fine pattern preparation by direct inkjet printing owing to low melting point, stable solvent dispersion, and high electric conductivity of their film. In this field, a fine metal patterning is fabricated by traditional printing technology. Normally, Ag NPs are covered with ligands to prevent the aggregation in the paste. After printing them on the substrate, the high conductivity is obtained by heating at very high temperature (> 250 °C) based on the removal of the ligands and the subsequent coalescence of Ag NPs. On the other hand, flexibility and transparency are required for the substrate of flexible electrodes. Plastic substrates satisfy the properties but shrink by the thermal treatment. The shrinkage causes the loss of resolution of fine patterning. Therefore, the development of sintering methods without the high temperature heating is highly desirable.

There are various sintering methods except for the simple thermal heating [2] nowadays, as mentioned in Chapter 1. Microwave irradiation [3-6], plasm treatment [5], laser irradiation [7-9], and flash light irradiation [10-12] have been well known as physical sintering methods. Although the process temperature in most of these methods is much lower than that in the thermal heating, the substrate is locally heated by electromagnetic irradiation. Local heating induces the damage and shrink of plastic substrates. Therefore, some chemicals (sintering agents) have been used for the assist of the sintering process. As these methods are carried out at room-temperature (RT), they are called RT chemical sintering. In the RT chemical sintering, Ag NPs are dipped into a solvent containing a sintering agent, which induces the desorption of ligands and then the coalescence of Ag NPs. These methods are mostly performed with aqueous Ag NP pastes in water because chloride salts such as sodium chloride [13-15], hydrogen chloride [13, 16], and poly(diallyldimethylammonium) chloride

[17] known as sintering agents of Ag NPs are extremely soluble in water. On the other hand, the RT chemical sintering with organic solvents was reported by Wakuda *et al* [18, 19]. In this report, dodecylamine-capped Ag NPs were prepared and sintered at RT by dipping into methanol. The affinity of the ligand to organic solvents is essential and therefore aqueous pastes of Ag NPs modified with polyionic compounds (e.g. sodium citrate and polyvinyl pyrrolidone) cannot be applied to the RT chemical sintering with organic solvents. The electrical resistivity of the Ag thin film obtained by this method was about 10^{-6} Ω m. As no sintering agent was used in the Wakuda's study, there is a possibility that more excellent conductivity can be achieved by adding a sintering agent. Non-aqueous Ag NP pastes are better than aqueous pastes in terms of easy control of viscosity and stable solvent dispersion of NPs. However, the RT chemical sintering of Ag NPs with organic solvents has been rarely performed because it is difficult to design a non-aqueous Ag NP paste fitted for this objective. In other words, Ag NPs need to stably disperse in the paste and to easily coalesce by the addition of sintering agents. In this chapter, aiming at the development of non-aqueous Ag NP pastes for RT chemical sintering, the combinations of ligand, dipping solvent, sintering agent were optimized.

First, oleic-acid-capped Ag NPs were adopted as the starting material for some ligand exchanges. Here, tri-*n*-octylphospine oxide (TOPO), octanoic acid (OA), and 1-dodecanethiol (DDT) were used as additive ligands. Their functional groups are well known as general adsorption moieties for Ag NPs [20-22]. Although amine ligands are also often used [23], the ligand exchange from oleic acid to *n*-octylamine did not proceed at all in the previous study performed in my laboratory [24]. Therefore, amine ligands were not used here. The crystallite sizes of Ag NPs and the amounts of ligands existing on the particle surface after ligand exchanges and subsequent washing process with methanol as an antisolvent were evaluated by powder X-ray diffraction (PXRD) and thermogravimetric analysis (TGA), respectively, in order to investigate desorption performance of ligands from Ag NPs (Figure 2-1).

Second, the non-aqueous paste consisting of Ag NPs capped with optimized ligands was prepared and the RT chemical sintering was carried out by dipping into organic solvents such as methanol (Figure 2-2). Sintering agents such as cetyltrimethylammonium chloride (CTAC) and cetyltrimethylammonium bromide (CTAB) for organic solvents were added into a dipping solvent. After the RT chemical sintering, the morphology and electrical resistivity of the obtained Ag thin films were investigated. The chemical composition of the Ag thin films after the RT chemical sintering was analyzed in detail by PXRD and X-ray photoelectron spectroscopy (XPS) measurements. In addition, the author considered the formation mechanism of Ag thin films from Ag NPs capped with optimized ligands in the RT chemical sintering with the aid of the sintering agents.

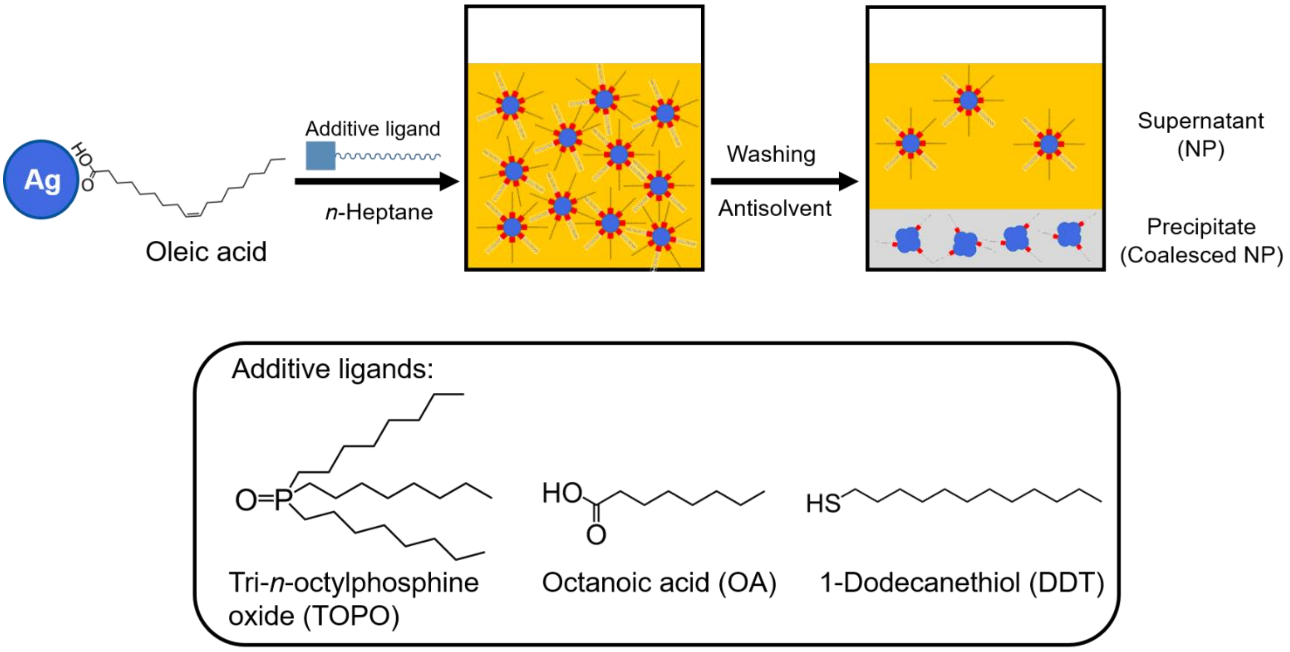

Figure 2-1. Ligand exchanges from oleic acid to TOPO, OA, and DDT on the surface of Ag NP and subsequent washing process with antisolvent.

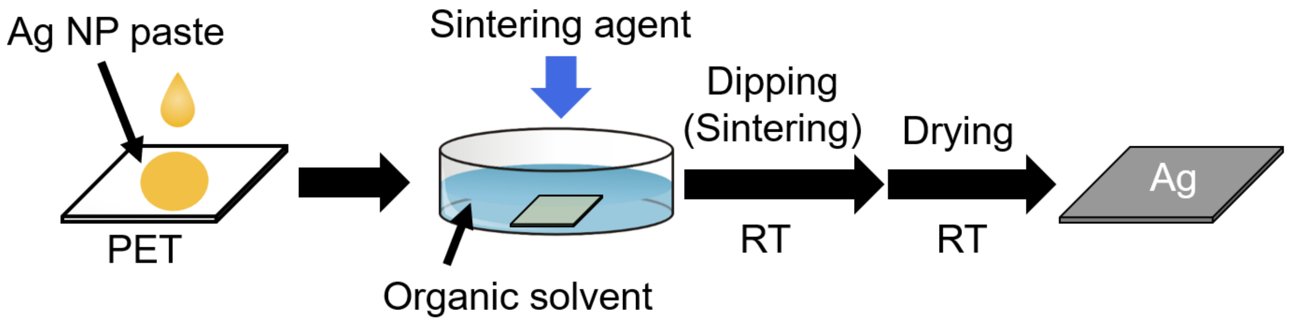

Figure 2-2. RT chemical sintering of the Ag NP paste by dipping into an organic solvent containing a sintering agent.

Section 2-2: Results and Discussion

2-2-1 Ag NPs after Ligand Exchange

Oleic-acid-capped Ag NPs prepared by the improved vacuum evaporation on running oil substrate (VEROS) method, which is one of the physical synthetic method of metal NPs, were used as starting materials. The improved VEROS method uses a cylindrical chamber for the formation of the oil film containing protective agents [25, 26]. The thin oil film is exposed to metal vapor many times with the rotation of the cylindrical chamber. Then, metal NPs with high purity can be obtained in the single step. The oleic-acid-capped Ag NPs are advantageous over dodecylamine-capped Ag NPs used in the Wakuda's study [18, 19] in terms of the below-mentioned points. Several tens of grams of Ag NPs can be produced even in a day in the laboratory scale equipment. Oleic acid adsorbs on Ag NPs more firmly than amine ligands, therefore, oleic-acid-capped Ag NPs can be completely isolated in air [24]. It takes only a few hours to prepare the paste from oleic-acid-capped Ag NPs.

As prepared Ag NPs after ligand exchanges and before the washing process, Transmission electron microscopy (TEM) observation was carried out (Figure 2-3). By the image analysis, average diameters of Ag NPs as prepared after ligand exchanges with TOPO, OA, and DDT were determined to be 5.8 ± 2.0 nm (Figure 2-3b), 5.3 ± 1.5 nm (Figure 2-3c), and 5.4 ± 1.4 nm (Figure 2-3d), respectively. The average diameters of Ag NPs as prepared after ligand exchanges were almost the same as that before ligand exchanges (6.3 ± 1.5 nm, Figure 2-3a). These results demonstrate that the coalescence of NPs is not induced by ligand exchanges, meaning that the additive ligands exist on the particle surface. Furthermore, the reaction solutions were diluted with *n*-heptane at the same ratio and 20 h later their plasmonic absorption peak derived from Ag NPs was measured (Figure 2-4). In the cases of ligand exchanges with OA and DDT, the bathochromic shift and broadening of the plasmonic absorption peak were observed compared with that of original Ag NPs before ligand exchanges. Generally, aggregation of Ag NPs induces long wavelength shift and broadening of the original plasmon peak [27]. On the other hand, such events were hardly observed in the case of the ligand exchange with TOPO. These facts suggest that TOPO-capped Ag NPs can disperse more stably in the solution than OA-capped and DDT-capped Ag NPs. In other words, TOPO firmly adsorbs on the Ag surface in a nonpolar solvent such as *n*-heptane.

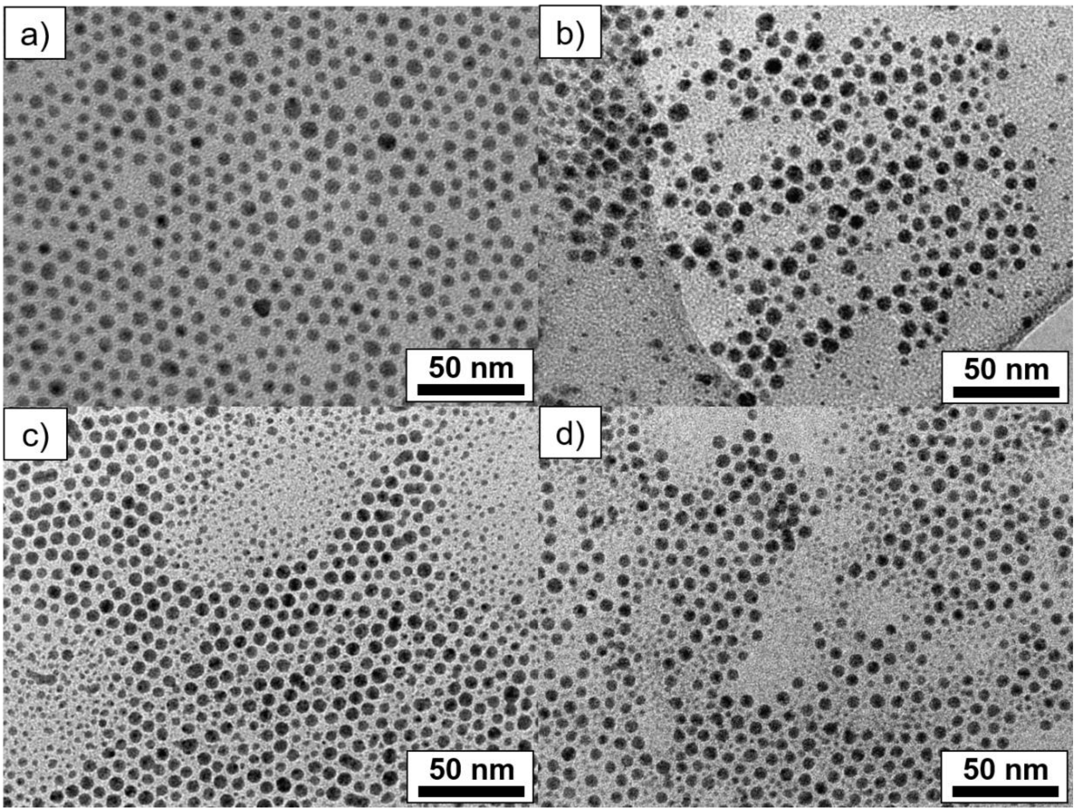

Figure 2-3. TEM images of Ag NPs a) before and after ligand exchanges with b) TOPO, c) OA, and d) DDT.

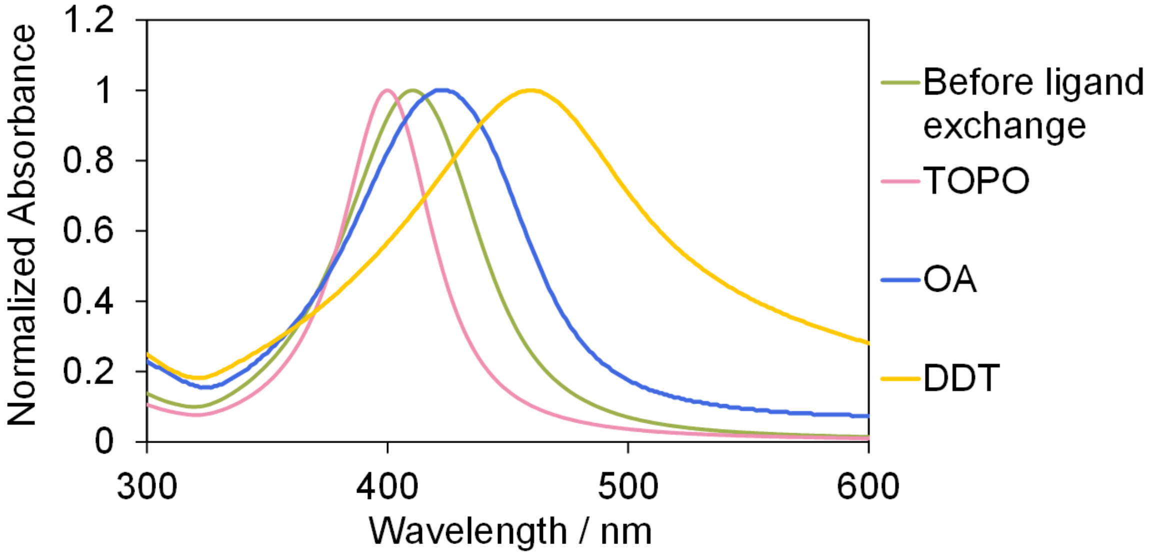

Figure 2-4. Absorption spectra of Ag NPs in *n*-heptane before and after ligand exchanges with TOPO, OA, and DDT.

Furthermore, the storage stability of the TOPO-capped Ag NP paste was investigated for 0 day (just after the fabrication) and 50 days. The Ag NP paste was diluted with *n*-heptane before measurements. The absorption spectra are shown in Figure 2-5. The absorption peaks and their full width at half maximum (FWHM) are summarized in Table 2-1. Even after the storage of the Ag NP paste for 50 days at RT, the bathochromic shift and broadening were hardly observed in absorption spectra. Similarly, from TEM observations (Figure 2-6), average diameters of Ag NPs hardly changed from 0 day (7.3 ± 1.5 nm) to 50 days (7.1 ± 1.2 nm). These results clearly indicate that the morphology and dispersion of Ag NPs remained unchanged after the storage and that the Ag NP paste can be stored stably for at least 50 days.

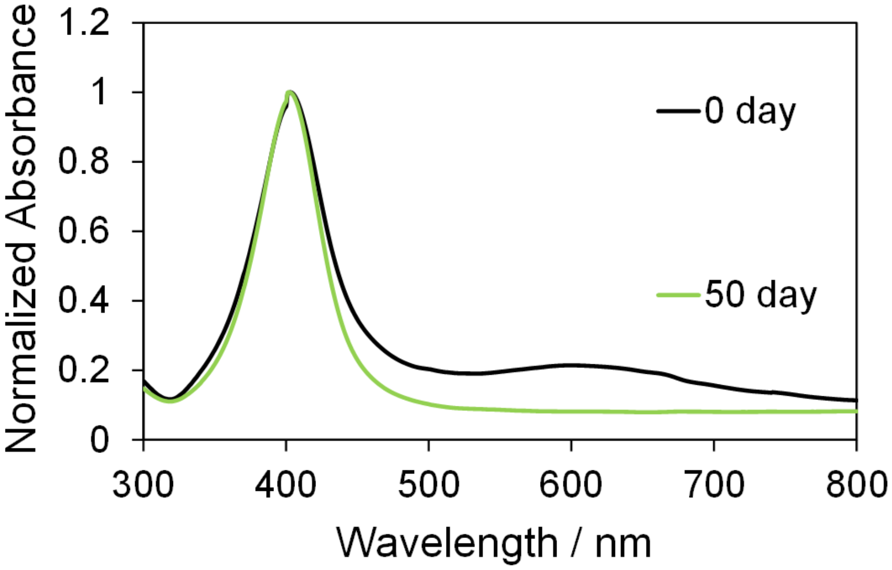

Figure 2-5. Absorption spectra of TOPO-capped Ag NPs stored for 0 day and 50 days at RT in *n*-heptane.

Table 2-1. Absorption peak and FWHM of TOPO-capped Ag NPs stored for 0 day and 50 days at RT.

Elapsed days	Absorption peak (nm)	FWHM (nm)
0	403	63
50	402	55

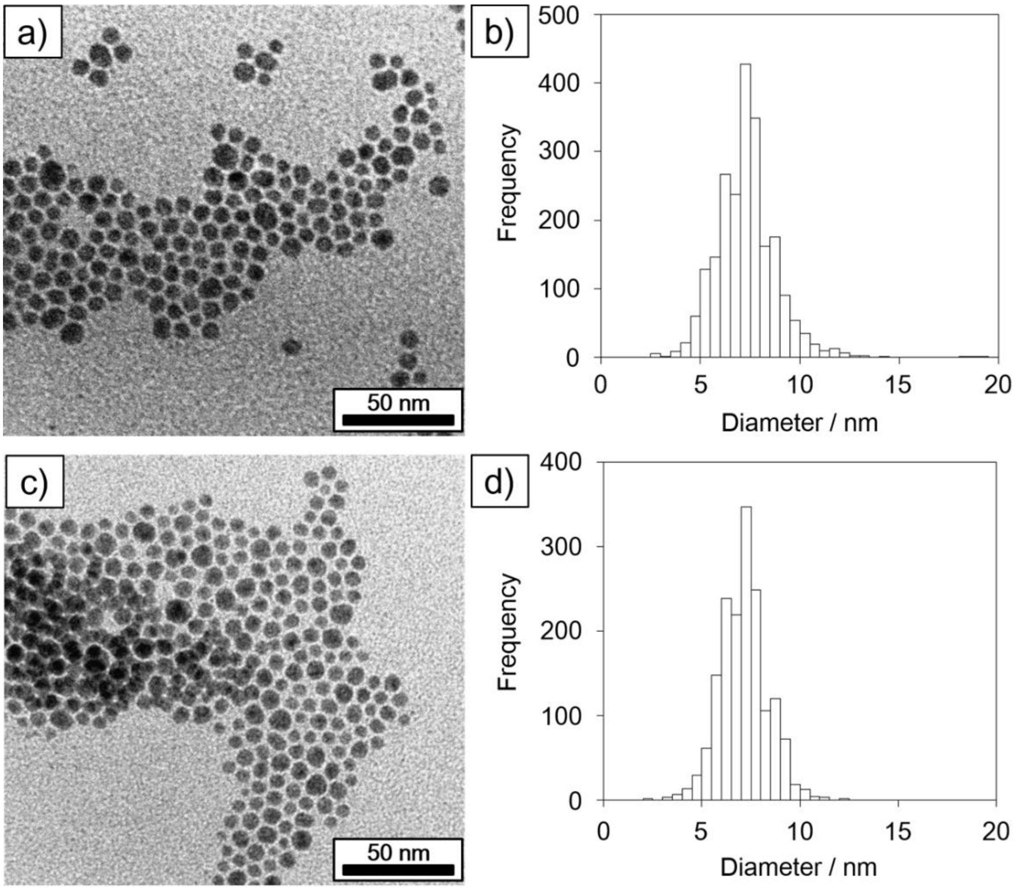

Figure 2-6. (a), (c) TEM images and (b), (d) particle size distributions of TOPO-capped Ag NPs stored for (a), (b) 0 day and (c), (d) 50 days at RT in TOPO.

2-2-2 Ag Precipitates after Ligand Exchange and Subsequent Washing Process

The Ag precipitates dried in vacuum after the washing process with methanol were analyzed by pyrolysis GC-MS to investigate the progress of ligand exchanges. Figure 2-7 shows total ion chromatograms (TICs) of the additive ligands and Ag NPs before and after ligand exchanges. After ligand exchanges, the peak of oleic acid at around 21 min (Figure 2-7a) was not detected in Ag NPs (Figure 2-7 e-g). These results show that oleic acid was completely removed during ligand exchanges. If not so, oleic acid should be detected like in the previous study performed in my laboratory [24]. Alternatively, in the case of the ligand exchange with OA, the peak of OA (Figure 2-7c) was clearly detected (Figure 2-7f). As for DDT, the peak of di-*n*-dodecyl sulfide originated from DDT in the pyrolysis process [28] was detected at around 26 min (Figure 2-7g), instead of the peak of DDT (Figure 2-7d). On the other hand, no peak was observed in the case of the ligand exchange with TOPO (Figure 2-7e) although the peak of TOPO was expected to be detected at around 28 min (Figure 2-7b).

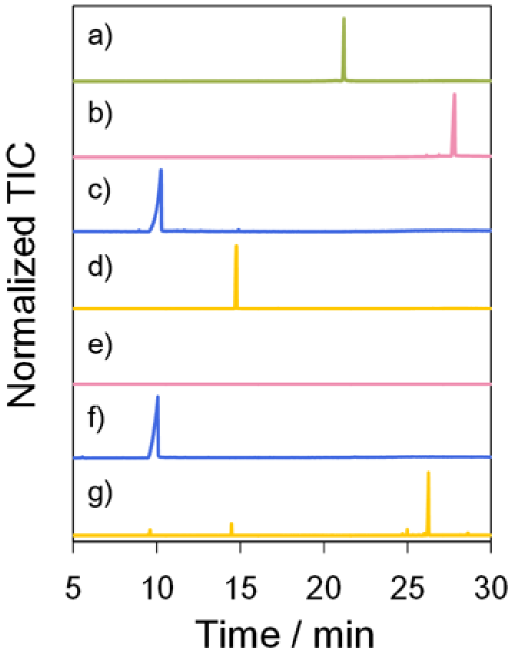

Figure 2-7. TICs of a) Ag NPs before ligand exchanges (capped with oleic acid), b) TOPO, c) OA, d) DDT, and Ag NPs after ligand exchanges with e) TOPO, f) OA, g) DDT.

The Ag precipitates were also used for TGA (Figure 2-8). Heating was performed in a helium atmosphere at a rate of 10 °C min^{-1} in the temperature range from 30 to 500 °C. The weight losses at 500 °C of oleic-acid-capped Ag NPs (before ligand exchanges) and Ag precipitates capped with TOPO, OA and DDT were 17 wt %, 4.4 wt %, 11 wt %, and 17 wt %, respectively, which assumes the loss of ligands on the particle surface. The molar amounts calculated from the weight losses in the cases of OA (7.6×10^{-4} mol g^{-1}) and DDT (8.4×10^{-4} mol g^{-1}) were almost equal to that of oleic acid (6.6×10^{-4} mol g^{-1}) adsorbed on the surface of the original NP. In the case of TOPO, the molar amount on the particle surface (1.1×10^{-4} mol g^{-1}) significantly decreased. This result indicates that TOPO was mostly removed from the particle surface in the washing process with methanol. In addition, the desorption temperature of TOPO from the Ag surface (350 °C) estimated from the TGA curve was significantly higher than the thermal decomposition temperature of TOPO (295 °C), demonstrating that TOPO on the Ag surface may be decomposed during the pyrolysis before its vaporization. Therefore, it is reasonable that TOPO was not detected in the pyrolysis GC-MS as shown above.

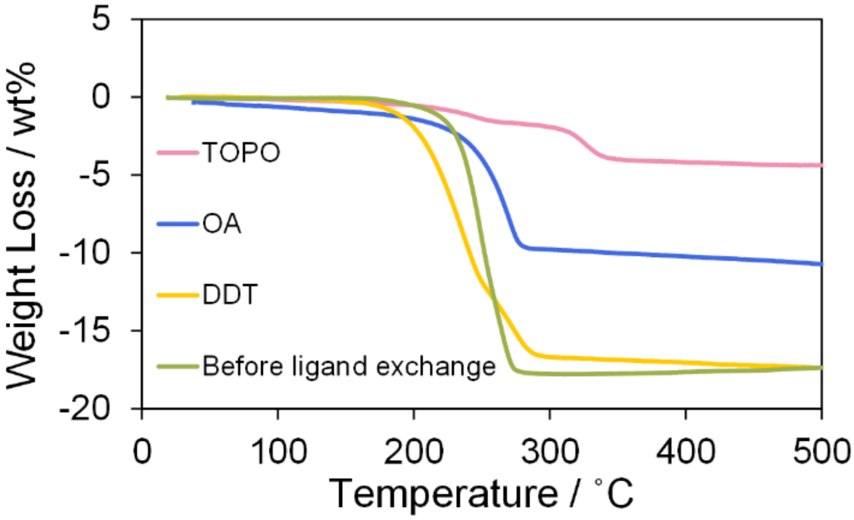

Figure 2-8. TGA curves of oleic-acid-capped Ag NPs (before ligand exchanges) and Ag NPs after ligand exchanges with TOPO, OA, and DDT in a helium atmosphere.

Next, Ag precipitates derived from Ag NPs after the washing process with methanol were evaluated by PXRD and TEM measurements. In order to dissociate NPs and their coalesced particles, *n*-hexane was added to the precipitates after the washing process, and the dispersion was separated into the supernatant (NPs) and precipitate (coalesced particle) after the centrifugation at 1000 rpm for 10 min. The precipitates were used for PXRD measurements (Figure 2-9). The crystallite sizes were calculated based on the Scherrer equation using FWHM of the diffraction peaks at 2° ≈ 38° [29-31]. The crystallite sizes after ligand exchanges with TOPO, OA, and DDT were 18.1 ± 0.4 nm (Figure 2-9b), 4.5 ± 0.1 nm (Figure 2-9c), 3.2 ± 0.1 nm (Figure 2-9d), respectively. The crystallite size increased in all the cases compared with that of the original Ag NPs (2.4 ± 0.1 nm, Figure 2-9a). Particularly, the crystallite size significantly increased in the case of the ligand exchange with TOPO.

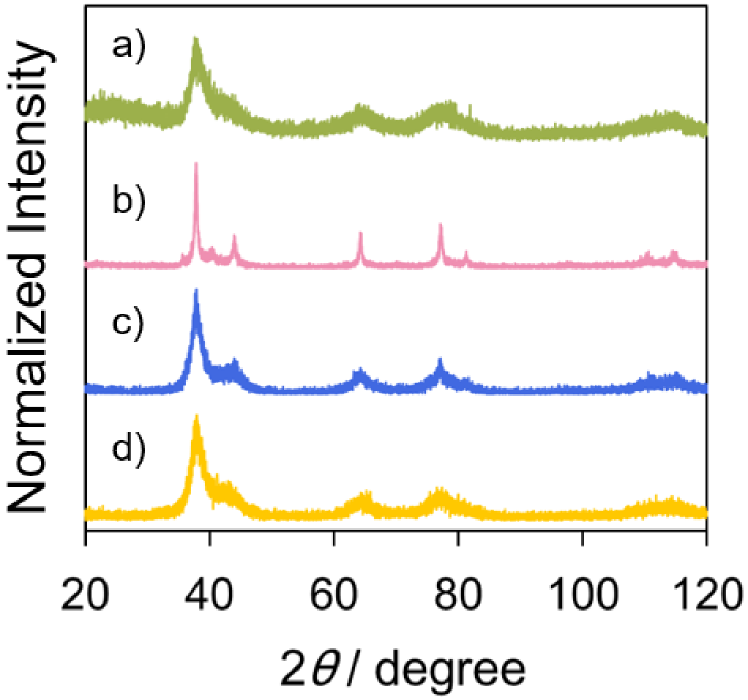

Figure 2-9. PXRD patterns of a) Ag NPs before ligand exchanges (capped with oleic acid) and precipitates separated after ligand exchanges with b) TOPO, c) OA, and d) DDT.

This tendency was also observed in the TEM images of the precipitates (Figure 2-10). In the precipitate separated after the ligand exchange with TOPO (Figure 2-10a), most of NPs were angular shape (red arrow points), showing that NPs coalesced each other to form larger and angular nanoparticles. In contrast, less angular NPs were observed in the precipitates separated after ligand exchanges with OA and DDT (Figure 2-10b and 2-10c). These results indicate that TOPO-capped Ag NPs coalesce in the washing process with methanol more effectively than OA- and DDT-capped Ag NPs. In order to confirm the effect of methanol in the washing process on the crystallite size, PXRD measurements for TOPO-capped Ag NPs were performed before and after the addition of methanol in the washing process (Figure 2-11). The crystallite size before and after the addition of methanol were 2.0 ± 0.1 nm and 19.1 ± 0.9 nm, respectively. Consequently, it was shown that the addition of methanol after the ligand exchange with TOPO induced the significant increase of the crystallite size.

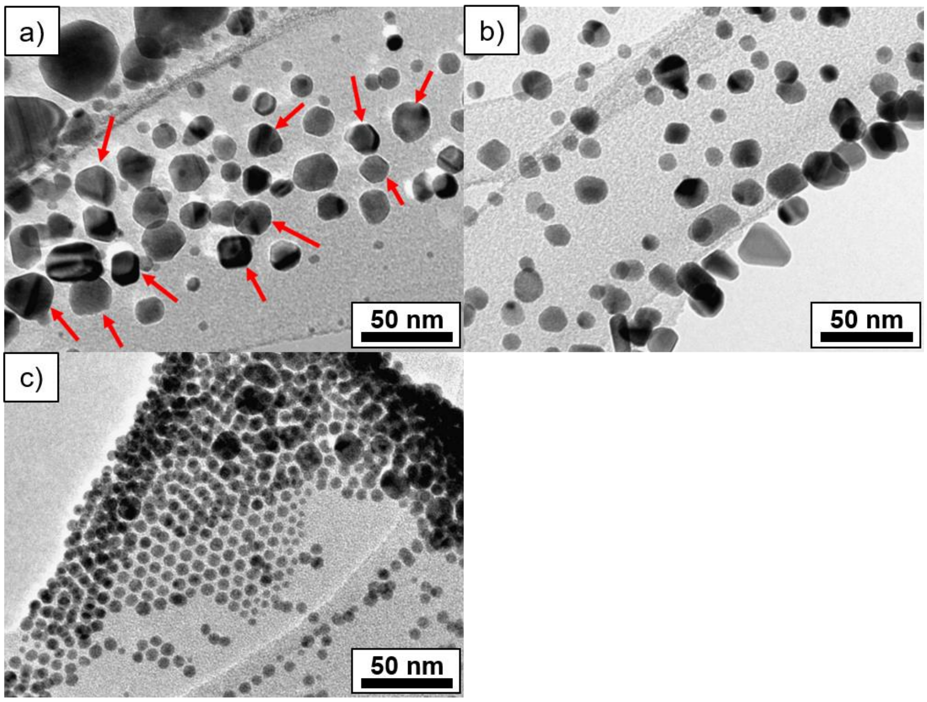

Figure 2-10. TEM images of precipitates separated after ligand exchanges with a) TOPO, b) OA, and c) DDT.

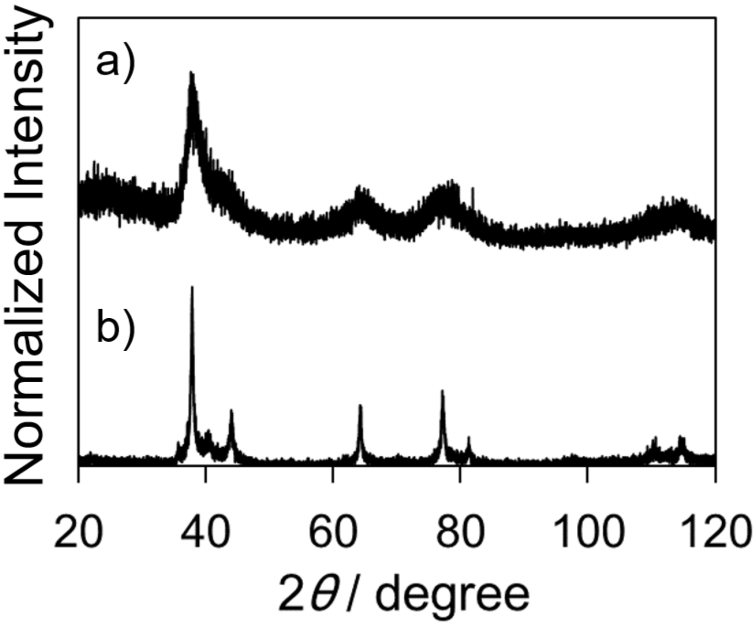

Figure 2-11. PXRD patterns of Ag NPs in the case of the ligand exchange with TOPO a) before and b) after the addition of methanol in the washing process.

2-2-3 Effect of Antisolvents on Coalescence of Ag NPs

In the previous section, the author found the following interesting experimental results. When TOPO was used for the ligand exchange of oleic-acid-capped Ag NPs, TOPO existed on the surface of as-prepared Ag NP after the ligand exchange. Then, TOPO desorbed from the NP surface in the washing process with methanol as an antisolvent. At this time, the crystallite size significantly increased, which shows that some NPs coalesced each other [32]. For increasing the crystallite size, methanol seems to play a crucial role. In order to verify this hypothesis, ethanol and 1-propanol were also adopted as antisolvents. In the washing process with antisolvent, the more hydrophobic the antisolvent was, the smaller the increase degree of the crystallite size became (Table 2-2). Furthermore, TGA measurements indicate that the molar amounts of TOPO remaining on the NP surface became larger in the cases of ethanol and 1-propanol than that in the case of methanol. These results show that methanol weakens the interaction between TOPO and the Ag surface most effectively. On the other hand, the interaction between ligands and the Ag surface in methanol is enough strong in the cases of OA and DDT as shown above. The interactions between ligands and the Ag surface are different among three additive agents. Namely, the main bonding forces of TOPO, OA, and DDT are dipole interaction, ionic interaction, and covalent bond, respectively. The dipole interaction between TOPO and the Ag surface would be weakened most effectively in a polar solvent. Therefore, TOPO-capped Ag NPs most effectively coalesced by the addition of methanol and the crystallite size increased at the maximum in all the cases.

Table 2-2. Molar amounts of ligands on the Ag NP surface and crystallite sizes of Ag precipitates after the ligand exchange with TOPO.

Antisolvent	Molar amount (× 10^{-4} mol g^{-1})[a]	Crystallite size ± standard error (nm)[b]
Methanol	1.1	18.1 ± 0.4
Ethanol	1.9	10.4 ± 0.4
1-Propanol	1.9	3.3 ± 0.1

a) By TGA. b) By PXRD.

2-2-4 Effect of Sintering Agent Concentration on Coalescence of Ag NPs

As mentioned in the previous section, TOPO firmly adsorbed on the Ag surface in *n*-heptane but tended to desorb in methanol, unlike OA and DDT. This interesting property of TOPO motivated the author to think that TOPO-capped Ag NPs are suitable for Ag nanoink in the RT chemical sintering with organic solvents. Thus, the non-aqueous paste consisting of TOPO and TOPO-capped Ag NPs was prepared and the RT chemical sintering was carried out by dipping into organic solvents such as methanol and ethanol. The fabricated Ag nanoink was cast onto the PET substrate. The RT chemical sintering was carried out by dipping the substrate into an organic solvent containing a sintering agent under an air atmosphere.

At first, CTAC and methanol were used as a sintering agent and dipping solvent, respectively. The reason is that CTAC has a chloride ion and it is freely soluble in methanol. The TOPO-capped Ag NP paste cast on the substrate was sintered at RT by dipping into methanol containing the different concentrations of CTAC. Figure 2-12 demonstrates the change of electrical resistivity of the Ag thin films as a function of the CTAC concentration in methanol. Here, the dipping time was fixed at 120 min. In the absence of CTAC, no conductivity was obtained. The SEM image of the Ag thin film shows that organic residues cover Ag NPs and inhibit their coalescence (Figure 2-13a). From the energy dispersive X-ray spectrum (EDS) (Figure 2-14a), the organic moistures were determined to be a compound containing the P atom, which would be assumed as TOPO. Therefore, the addition of chloride salt is necessary for obtaining a conductive Ag thin film in this RT chemical sintering. The result is apparently different from the Wakuda's result [19]. In the Wakuda's study, sintering agents were not necessary for the RT sintering. This difference may be due to the fact that TOPO adsorbs on Ag NPs more firmly than amine ligands. According to Figure 2-12, the increase of the CTAC concentration contributed to the decrease of electrical resistivity. In the cases of more than 0.20 mM CTAC, the electrical resistivity reached an almost constant value. In fact, most of Ag NPs coalesced in the corresponding SEM images (Figure 2-13c and 2-13d). In the cases of more than 0.20 mM CTAC, the organic residues were mostly removed from the Ag thin films, which was confirmed by the EDS spectrum (Figures 2-14c and 2-14d). On the other hand, some organic moistures remained in the case of 0.040 mM CTAC (Figure 2-13b). In fact, the small peak originated from the P atom of TOPO was detected in the EDS spectrum (Figure 2-14b). Here, the author can say that the addition of more than 0.20 mM of chloride salt is preferred. In addition, the cross sectional SEM image of this thin film revealed that the coalescence of Ag NPs proceeded up to 1 μm depth at least by dipping into 0.20 mM CTAC methanol solution at RT for 120 min (Figure 2-15).

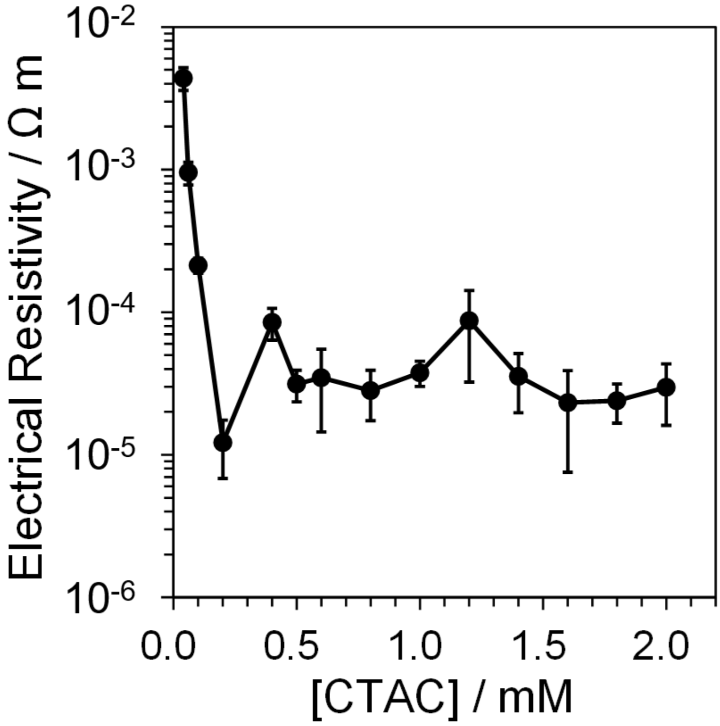

Figure 2-12. Change of electrical resistivity of the Ag thin films as a function of the CTAC concentration in methanol (dipping time: 120 min).

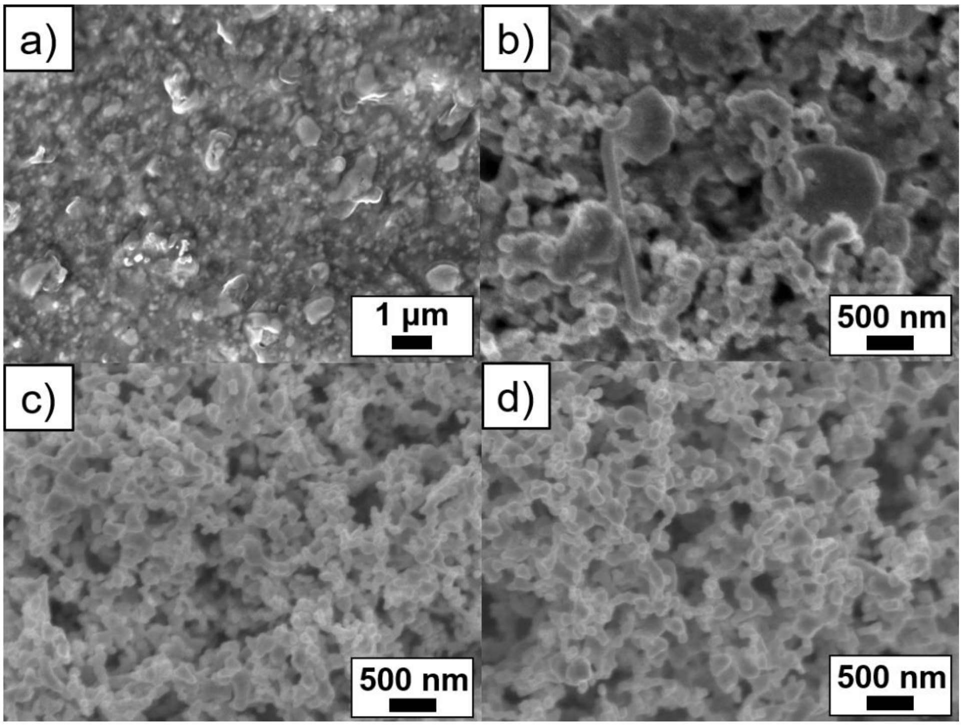

Figure 2-13. SEM images of the Ag thin films prepared from the TOPO-capped Ag NP paste by dipping into methanol (a) without and with (b) 0.040 mM, (c) 0.20 mM, (d) 1.0 mM CTAC.

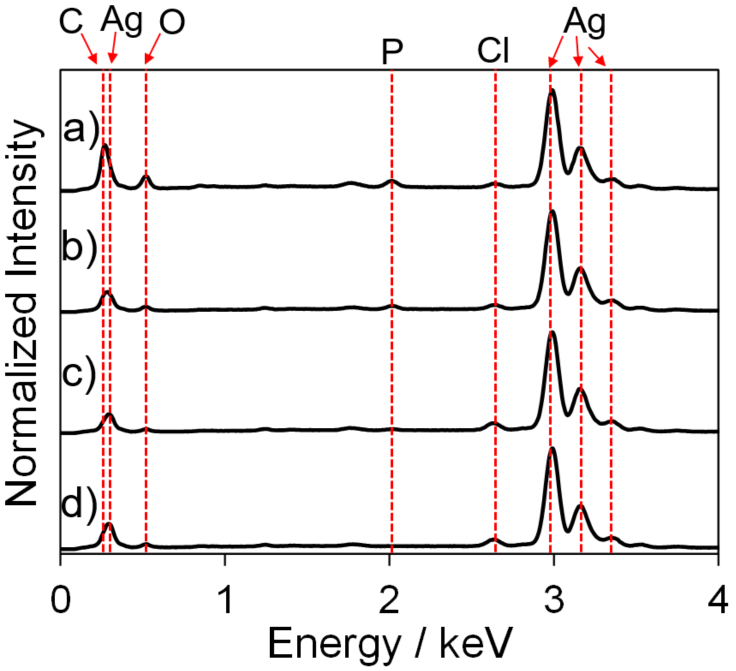

Figure 2-14. EDS spectra of the Ag thin films prepared from the TOPO-capped Ag NP paste by dipping into methanol (a) without and with (b) 0.040 mM, (c) 0.20 mM, (d) 1.0 mM CTAC.

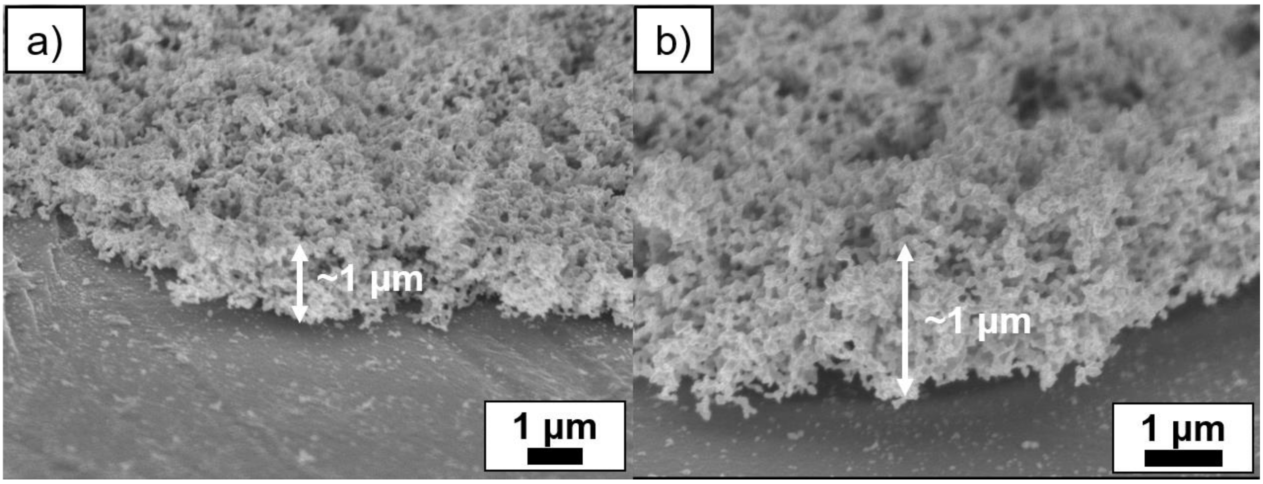

Figure 2-15. Cross sectional SEM images of the Ag thin film prepared from Ag NPs by dipping into the 0.20 mM CTAC methanol solution observed at (a) 10 000-fold magnification and (b) 15 000-fold magnification.

.

2-2-5 Effect of Dipping Time on Coalescence of Ag NPs

Next, the effect of dipping time in the RT chemical sintering was investigated using the TOPO-capped Ag NP paste. The concentration of CTAC was set to 1.0 mM in methanol. The dipping time was changed in the range of 1-120 min. Figure 2-16 and 2-17 show the change of electrical resistivity of the Ag thin films as a function of dipping time and their SEM images, respectively. Before the dipping (Figure 2-17a) and after 1 min of dipping (Figure 2-17b), the organic moistures were observed in almost all of the area. The organic moistures were determined to be a compound containing the P atom from the EDS spectrum (Figure 2-18a). Even after 2 min of dipping, organic moistures were still left in some parts (Figure 2-17c, 2-18b). Actually, the electrical resistivity was relatively high at that time. The electrical resistivity gradually decreased with the increase of the dipping time in the range of 1-10 min. The electrical resistivity of the Ag thin film after 10 min of dipping was $(6.0 \pm 2.5) \times 10^{-5}$ Ω m. After 10 min of dipping, the organic moistures were completely removed and the coalescence of Ag NPs was clearly observed (Figure 2-17d). From these results, it is concluded that more than 10 min of dipping is required for obtaining the conductivity in the RT chemical sintering.

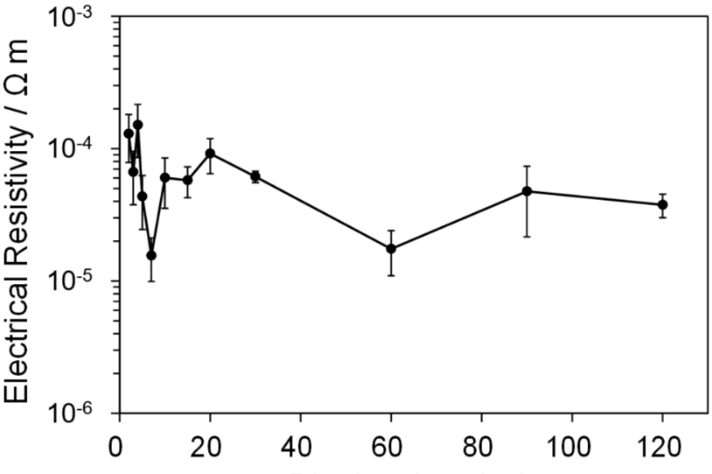

Figure 2-16. Change of electrical resistivity of the Ag thin films as a function of dipping time into the 1.0 mM CTAC methanol solution.

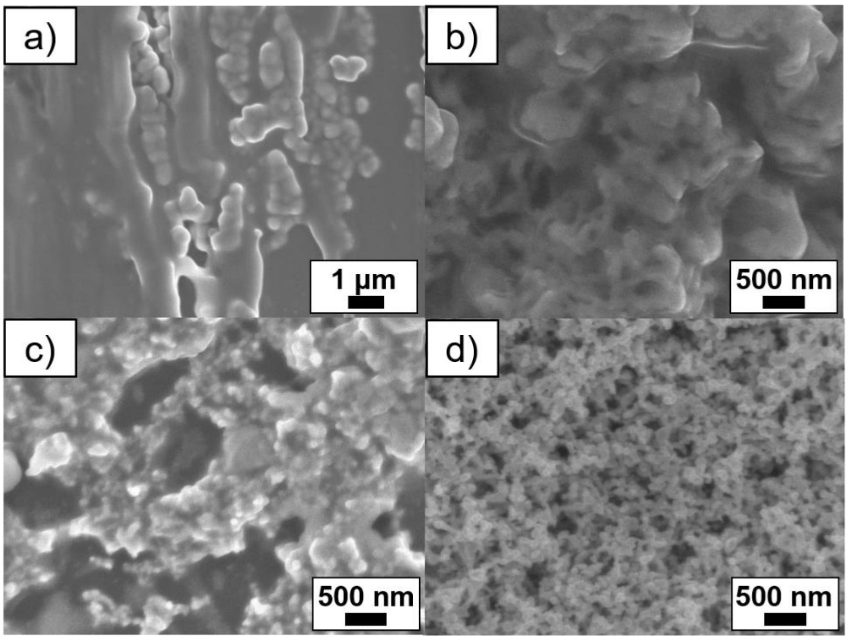

Figure 2-17. SEM images of (a) cast film of the TOPO-capped Ag NP paste and the Ag thin films prepared from the TOPO-capped Ag NP paste by dipping into the 1.0 mM CTAC methanol solution for (b) 1 min, (c) 2 min, and (d) 10 min.

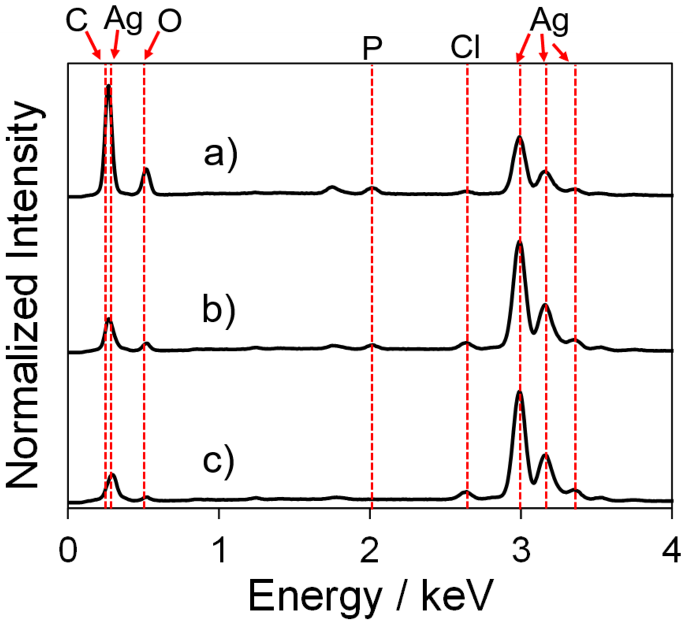

Figure 2-18. EDS spectra of the Ag thin films prepared from the TOPO-capped Ag NP paste by dipping into the 1.0 mM CTAC methanol solution for (a) 1 min, (b) 2 min, and (c) 120 min.

2-2-6 Effect of Dipping Solvent on Coalescence of Ag NPs

Following, the effect of dipping solvent on electrical resistivity was investigated using the TOPO-capped Ag NP paste and CTAC (Figure2-19). The dipping time was fixed at 120 min. Here, ethanol and 1-propanol were used instead of methanol. In the case of ethanol, the similar profile to methanol was observed. Coalescence of Ag NPs was observed in the SEM image in the same way as the case of methanol (Figure 2-20a). The lowest electrical resistivity was $(1.1 \pm 0.7) \times 10^{-5}$ Ω m. In the case of 1-propanol, the electrical resistivity was totally higher than that in the case of ethanol. The electrical resistivity was too high to be measured in the range of more than 0.80 mM CTAC (0.80 mM, 1.0 mM, and 1.2 mM). The high electrical resistivity was attributed to incomplete coalescence of Ag NPs (Figure 2-20b). In such cases, many cracks were generated in the film due to the low adhesion strength between Ag NPs and the PET substrate in 1-propanol. In summary, the more hydrophilic the dipping solvent was, the lower the electrical resistivity was. This result nicely corresponded to that in the section 2-2-4. Therein, it was mentioned that the more hydrophilic the washing solvent was, the larger the crystallite size of Ag NPs was in the washing process with centrifugation after the ligand exchange from oleic acid to TOPO. This phenomenon may be due to the desorption of TOPO from Ag NPs based on the significant lowering of the interaction between TOPO and the Ag surface in a hydrophilic solvent. In addition, the solubility of the ligand affects the desorption from the metal surface. In the Wakuda's study, oleylamine on the surface of Ag NPs easily desorbed in the good solvent of the ligand [19]. As TOPO is highly soluble in methanol and ethanol, it is similarly thought that most of TOPO desorbs from Ag NPs in methanol and ethanol, which induces the effective coalescence of Ag NPs.

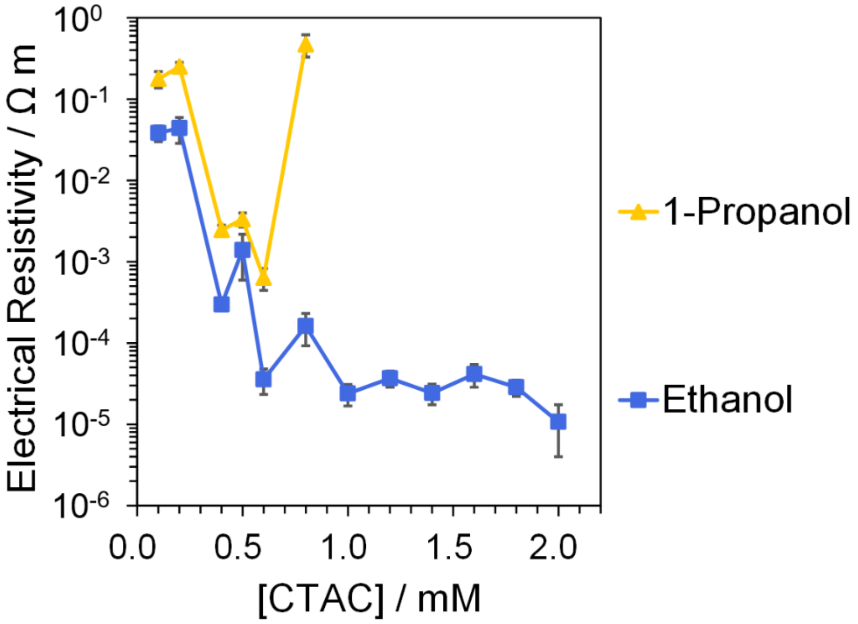

Figure 2-19. Change of electrical resistivity of the Ag thin films as a function of the CTAC concentration in various dipping solvents (dipping time: 120 min).

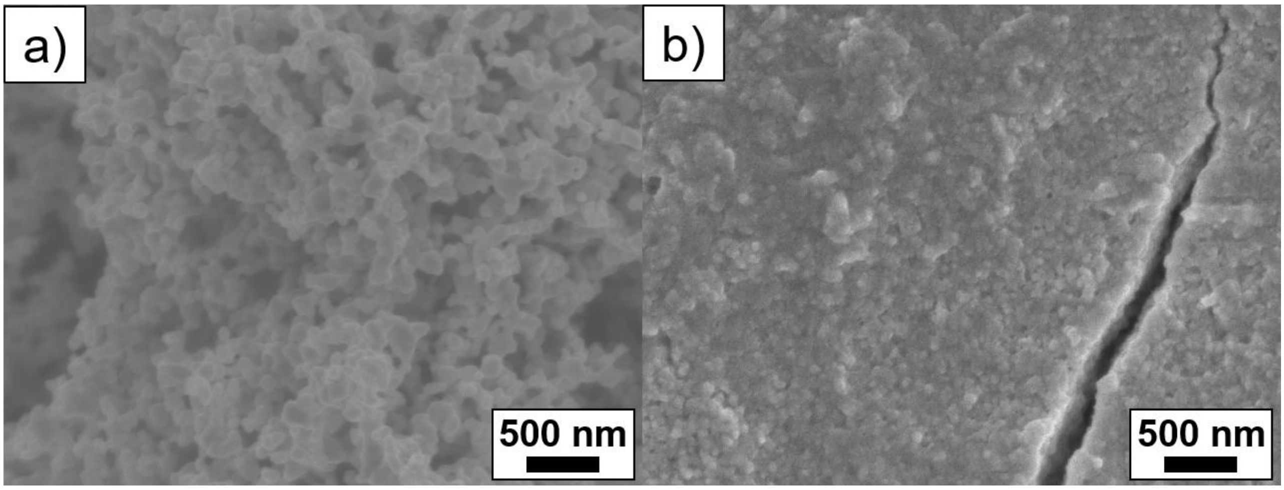

Figure 2-20. SEM images of the Ag thin films prepared from the TOPO-capped Ag NP paste by dipping into the 1.0 mM CTAC (a) ethanol and (b) 1-propanol solution for 120 min.

2-2-7 Effect of Sintering Agents on Coalescence of Ag NPs

Other types of sintering agents, which are NaCl, CH_3COONa, and hexadecyltrimethylammonium bromide (CTAB), were also examined using the TOPO-capped Ag NP paste and methanol. The concentration of sintering agents and dipping time were fixed at 1.0 mM and 120 min, respectively. Table 2-3 shows the lowest electrical resistivity in each case. The electrical resistivity in the case of NaCl and CTAB was comparable to that in the case of CTAC. In the case of CH_3COONa, the Ag thin film with the high electrical resistivity was obtained. In the cases of halide salts, the organic residues were completely removed and the coalescence of Ag NPs was clearly observed (Figure 2-21a and 2-21b). In the case of CH_3COONa, however, the organic moistures were observed in almost all of the area (Figure 2-21c). These results may be explained by solubility of generated silver salts (AgCl, AgBr, and $AgCH_3COO$). The solubility of silver acetate to methanol is significantly higher than silver halides (Table 2-4). Therefore, the interaction between the Ag surface and halide ion seems to be stronger than that between the Ag surface and acetate ion. The halide ion adsorbs on the Ag surface, and then TOPO desorbs from Ag NPs. This event induces the coalescence of Ag NPs (Figure 2-22). Thus, sintering agents possessing halide ion showed the strong sintering ability towards Ag NPs. As it is relatively time-consuming and laborious to dissolve NaCl in methanol, CTAC and CTAB are more suitable for this RT chemical sintering due to the high solubility in methanol.

Table 2-3. Electrical resistivity of the Ag thin films after the RT chemical sintering using various sintering agents.

Sintering agent	Electrical resistivity (Ω m)
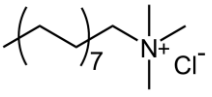 CTAC	(3.8 ± 0.8) × 10^{-5}
NaCl	(2.6 ± 0.7) × 10^{-5}
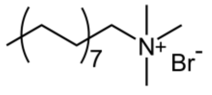 CTAB	(2.6 ± 0.8) × 10^{-5}
CH_3COONa	(3.3 ± 2.2) × 10^{-3}

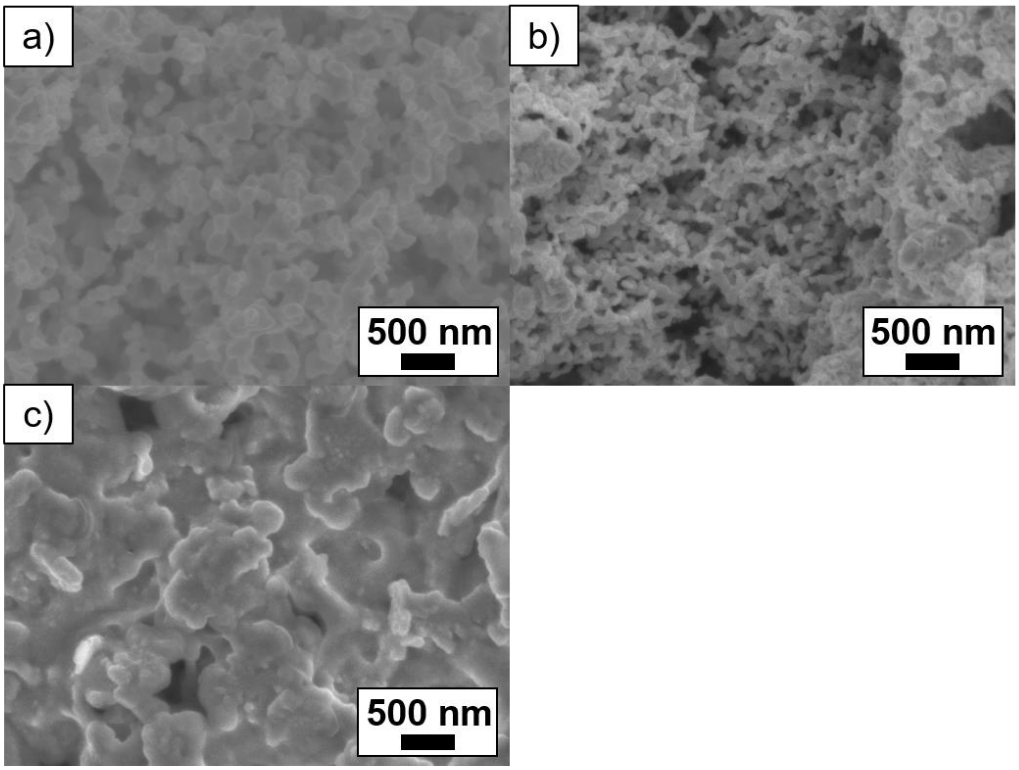

Figure 2-21. SEM images of the Ag thin films prepared from the TOPO-capped Ag NP paste by dipping into the 1.0 mM (a) NaCl, (b) CTAB, and (c) CH_3COONa methanol solution for 120 min.

Table 2-4. Solubility product constants of silver salts in methanol.

Silver salts	Solubility product constants	Temperature (°C)	Ref.
AgCl	$10^{-13.0}$	23	31
AgBr	$10^{-15.2}$	23	31
$AgCH_3COO$	$10^{-5.59}$	25	32

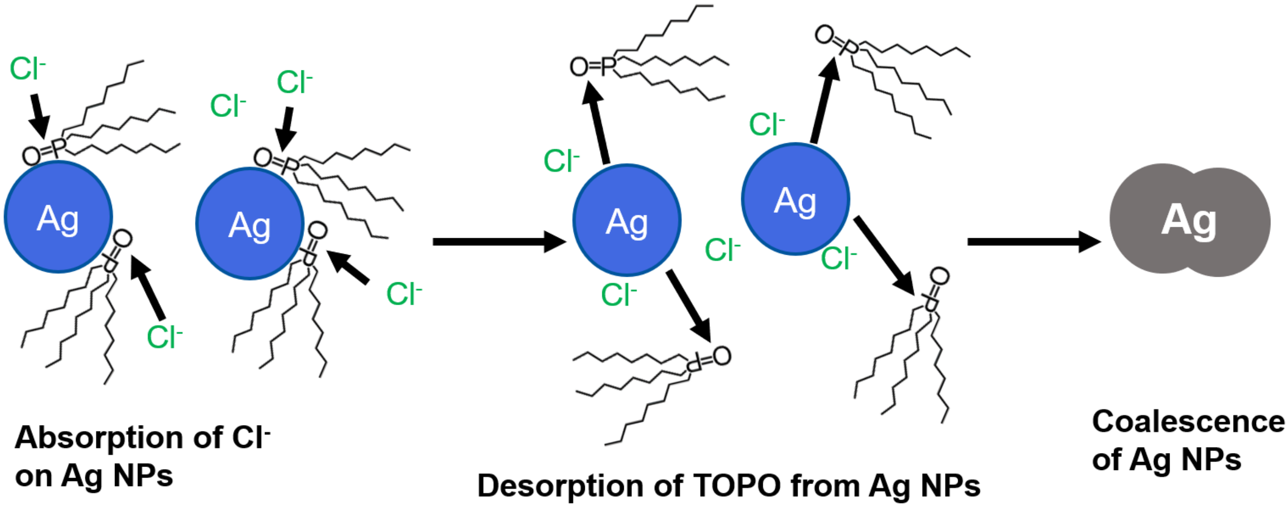

Figure 2-22. Plausible schematic illustration of the RT chemical sintering of TOPO-capped-Ag NPs by dipping into methanol containing Cl^-.

2-2-8 Effect of Ligands on RT Chemical Sintering of Ag NPs

To confirm the necessity of the ligand exchange from oleic acid to TOPO, oleic-acid-capped Ag NPs were also used as Ag nanoink. The obtained Ag thin film was not conductive even under the best sintering conditions (dipping solvent: methanol, dipping time: 120 min, and sintering agent: 1.0 mM CTAC). Moreover, it was observed in the SEM image that Ag NPs were partially coalesced (Figure 2-23). Thus, TOPO is more suitable than oleic acid in this RT chemical sintering.

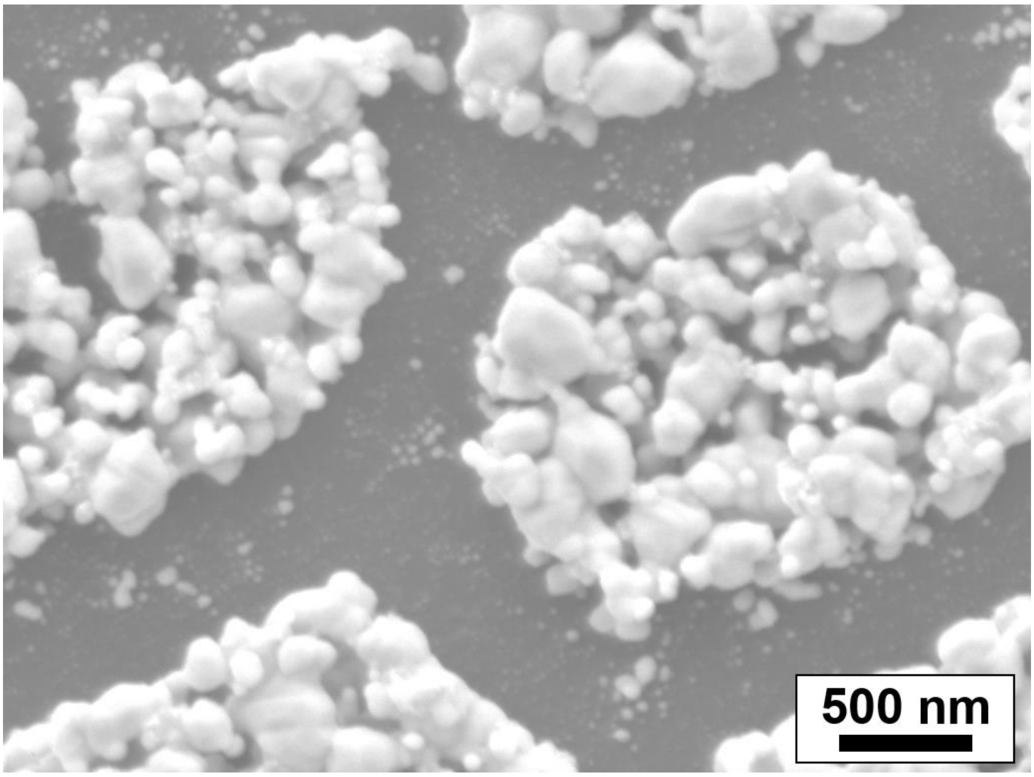

Figure 2-23. SEM image of the Ag thin film prepared from the oleic-acid-capped Ag NP paste by dipping into the 1.0 mM CTAC methanol solution for 120 min.

2-2-9 Characterization of Ag Thin Films Prepared by RT Chemical Sintering

The Ag thin film was prepared from the TOPO-capped Ag NP paste by dipping into the 1.0 mM CTAC methanol solution for 120 min. The PXRD pattern is shown in Figure 2-24, in addition to bulk Ag and the PET substrate. The diffraction peaks at $2\theta = 38°$, 44°, 64°, and 77° are identified as the (111), (200), (220), and (311) planes of face-centered cubic Ag, respectively [31]. The diffraction pattern also had $2\theta = 23°$ and 26°. These peaks refer to the (110) and (100) planes of PET [35]. The diffraction pattern of the Ag thin film was almost consistent with the sum of bulk Ag (face centered cubic structure) and PET substrate. The crystallite sizes of the Ag thin films are calculated based on the Scherrer equation using FWHM of the diffraction peaks at $2\theta \approx 38°$ [31]. The crystallite size in the case of Figure 2-24c determined to be 26 nm. The crystallite size significantly increased compared with that of the original NP (4.4 nm). This result shows the coalescence of Ag NPs. Slightly, the peak originated from Ag_2O or AgCl ($2\theta = 32°$) was also observed (red arrow point) [36, 37]. Next, the Ag thin film was evaluated by TGA (Figure 2-25). The weight loss at 500 °C was 3.4 wt%, which assumes the loss of organic residues in the Ag thin film. Namely, organic compounds such as TOPO and CTAC hardly existed in the Ag thin film. This result demonstrates that the purity of the Ag thin film obtained in this method is relatively high.

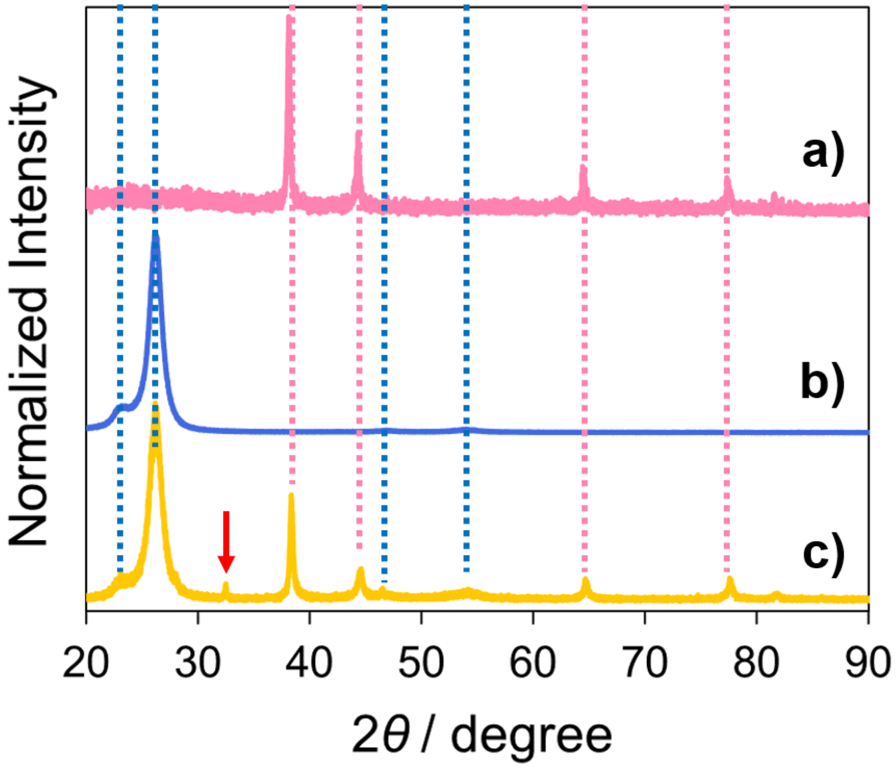

Figure 2-24. PXRD patterns of (a) bulk Ag, (b) PET substrate, and (c) the Ag thin film prepared from the TOPO-capped Ag NP paste by dipping into the 1.0 mM CTAC methanol solution for 120 min.

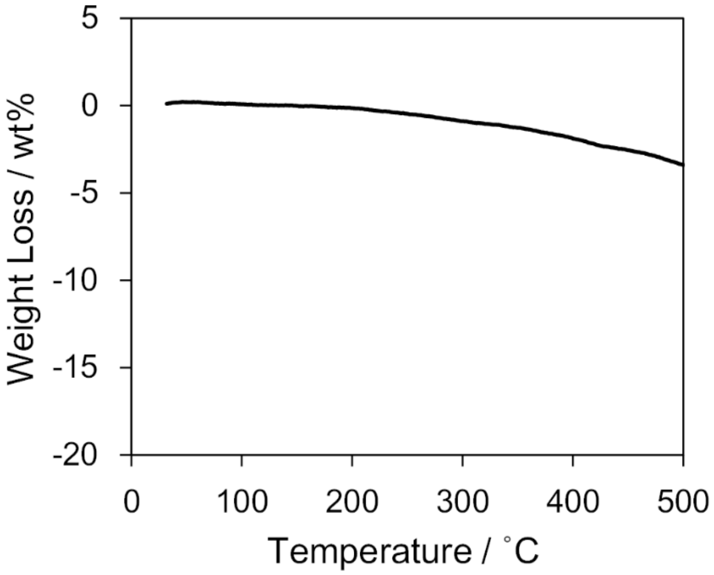

Figure 2-25. TGA curve of the Ag thin film prepared from the TOPO-capped Ag NP paste by dipping into the 1.0 mM CTAC methanol solution for 120 min.

The chemical composition of the Ag thin films after the RT chemical sintering was analyzed by XPS, as shown in Figure 2-26. Three kinds of concentrations (0.040 mM, 0.20 mM, and 1.0 mM) of the CTAC methanol solutions were used and the dipping time was fixed at 120 min. Particularly, the peaks of Ag 3d were noted here, and the peaks of 368.5 eV and 374.5 eV were identified as Ag $3d_{5/2}$ and Ag $3d_{3/2}$, respectively [36-41]. In the cases of the 0.040 mM and 0.20 mM CTAC methanol solutions, only above-mention peaks were observed. The experimental facts show that the pure Ag thin film was formed in these cases. On the other hand, in the cases of the 1.0 mM CTAC methanol solution, the peaks of 367.9 eV and 373.9 eV were observed. They were identified as Ag $3d_{5/2}$ at and Ag $3d_{3/2}$ in Ag_2O or AgCl, respectively [36-41]. In the case of the high CTAC concentration, TOPO rapidly desorbs from Ag NPs and the Ag surface may be oxidized by O_2 in the unprotected area of Ag NPs. In the case of the low CTAC concentration, the Ag surface is protected with TOPO during the RT chemical sintering. Accordingly, the appropriate concentration of sintering agents should be used for the RT chemical sintering.

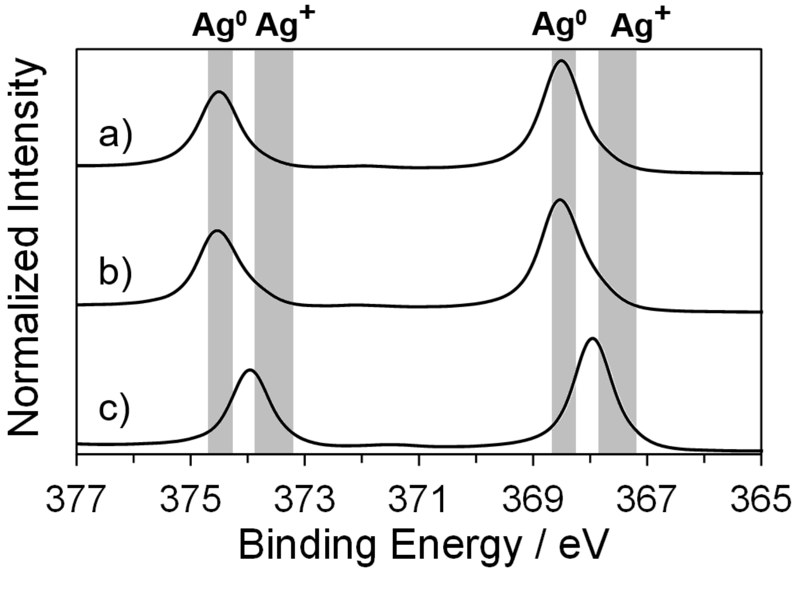

Figure 2-26. XPS spectra of Ag 3d in the Ag thin films prepared from the TOPO-capped Ag NP paste by dipping into the a) 0.040 mM, b) 0.20 mM, and c) 1.0 mM CTAC methanol solutions for 120 min.

2-2-9 Comparison between RT Chemical Sintering and Thermal Sintering

For comparison, the thermal sintering was carried out at 350 °C for 120 min on the glass substrate using the oleic-acid-capped Ag NP paste. The SEM image showed that Ag NPs significantly coalesced each other and formed a continuous film after the thermal sintering (Figure 2-27). In the case of the thermal sintering, much larger grains of Ag NPs than those prepared by the RT chemical sintering were observed (Figure 2-13 and 2-17) because Ag NPs partially melted by heating at 350 °C. The organic residue rarely remained in the Ag thin film, which was confirmed by the EDS spectrum (Figure 2-28). The electrical resistivity of the Ag thin film, which was $(7.8 \pm 3.4) \times 10^{-6}$ Ω m, is slightly lower than those of the Ag thin films prepared by the RT chemical sintering. The electrical resistivity of this Ag thin film obtained by the thermal sintering seems to be the lowest value under my experimental conditions. Therefore, it was shown that the RT chemical sintering examined in this study has the almost similar film-formation ability to that of the normal thermal sintering.

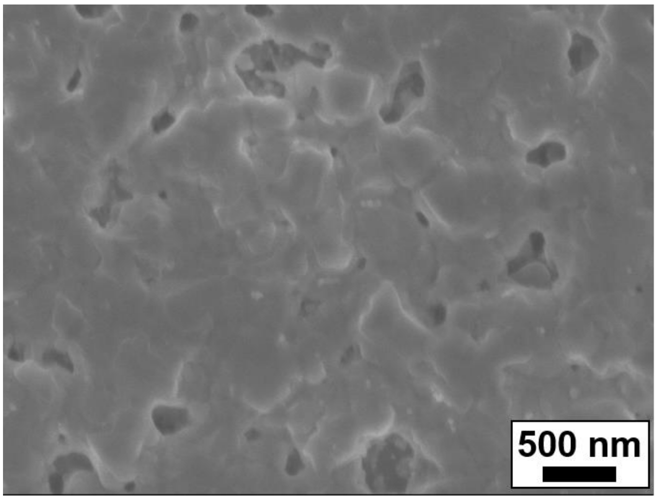

Figure 2-27. SEM image of the Ag thin film prepared from the oleic-acid-capped Ag NP paste by the thermal sintering (350 °C, 120 min).

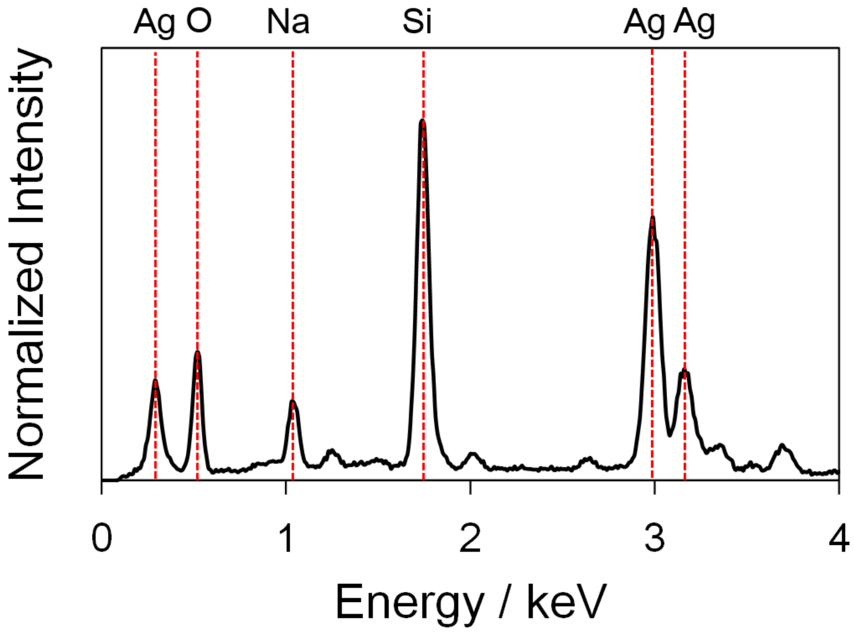

Figure 2-28. EDS spectrum of the Ag thin film prepared from the oleic-acid-capped Ag NP paste by the thermal sintering (350 °C, 120 min).

Section 2-3: Summary

On the surface of Ag NP, ligand exchanges from oleic acid to the additive ligands were carried out and the NPs were washed with methanol as an antisolvent after the reactions. In the case of the ligand exchange with TOPO, most of ligands desorbed from the particle surface and the crystallite size significantly increased. In contrast, the crystallite sizes of Ag NPs capped with OA and DDT less increased. Although TOPO firmly adsorbed on the Ag surface in a nonpolar solvent such as *n*-heptane, the adsorption strength was dramatically weakened in methanol. Therefore, in application of Ag NPs to nanoinks for writing fine pattern, sintering temperature of the written pattern could be lowered extremely by using the TOPO-capped Ag NPs and their subsequent washing process with methanol.

Based on the above-mentioned results, the author can say that pure Ag thin films were prepared from the TOPO-capped Ag NP paste by dipping into an organic solvent containing a sintering agent. The lowest electrical resistivity in this study was $(1.2 \pm 0.5) \times 10^{-5}$ Ω m under the conditions of the RT chemical sintering (dipping time: 120 min, CTAC concentration: 0.20 mM, and dipping solvent: methanol). The electrical resistivity could be decreased by increasing the concentration of Ag NPs in the paste. The author revealed that electrical resistivity of the Ag thin films was dependent on sintering agent, its concentration, dipping time, ligand of Ag NP, polarity of dipping solvent, and solubility of ligand for dipping solvent. Notably, it is possible that the excess addition of sintering agents induced not only the formation of Ag thin film but also the generation of Ag_2O or AgCl. Therefore, the appropriate concentration of sintering agents should be added in the RT chemical sintering with organic solvents. The author expects that the knowledge obtained in this chapter will be a guideline in the fabrication of flexible electrodes by the RT chemical sintering of Ag NPs with organic solvents.

Section 2-4: Experiments

2-4-1 Materials

All the chemicals and solvents were obtained commercially and used without further purification. Tri-*n*-octylphosphine oxide (TOPO) was purchased from Aldrich. Octanoic acid (OA) was purchased from Tokyo Chemical Industries Co.,Ltd. 1-Dodecanethiol (DDT) was purchased from Merck. Sodium chloride (NaCl), cetyltrimethylammonium chloride (CTAC), and cetyltrimethylammonium bromide (CTAB) were obtained from Wako Pure Chemical Industries, Ltd. Sodium Acetate (CH_3COONa) was purchased from Nakarai Tesque, Inc. Oleic-acid-capped Ag nanoparticles (Ag NPs, Kishu-Giken Co.,LTD, Wakayama, Japan), which were synthesized by the improved vacuum evaporation on running oil substrate (VEROS) method [25, 26], were used for fabrication of Ag nanoink. The average diameter of oleic-acid-capped Ag NPs used here was 6.3 ± 1.5 nm (Figure 2-3a).

2-4-2 Ligand Exchange and Subsequent Washing Process

Oleic-acid-capped Ag NPs were dispersed in *n*-heptane at a concentration of 0.50 g L^{-1}. The *n*-heptane solution of the additive ligand (0.12 M) was added to the dispersion of Ag NPs. The molar amount of the additive ligands was 40 times as large as that of oleic acid adsorbed on the surface of the original nanoparticle. The concentrations after mixing were adjusted to 0.45 g L^{-1} (Ag NP) and 1.1×10^{-2} M (additive ligand), respectively. The mixture was stirred at 40 °C for an hour. After the reaction, Ag NPs were purified by the following washing process with antisolvent. The reaction solution was somewhat concentrated by a rotary evaporator. This concentrated solution was used as Ag paste. Methanol as an antisolvent was then added to the dispersion. The volume ratio of the solvent containing nanoparticles to the antisolvent was more than four. The dispersion was then centrifuged at 14 500 rpm for 10 min. After the removal of the supernatant, antisolvent was added to the residue again. The centrifugation at 5000 rpm for 10 min was then carried out. The same procedure was repeated three times. The obtained nanoparticles were dried in vacuum.

2-4-3 Preparation for Ag Thin Films

The ligand exchange of Ag NPs from oleic acid to TOPO was carried out as mentioned in the section 2-3-2. After the ligand exchange, *n*-heptane was removed by a rotary evaporator. Thus, the prepared paste mainly consists of TOPO and TOPO-capped-Ag NPs (TOPO-capped Ag NP paste). For comparison, the paste consisting of *n*-heptane and oleic-acid-capped Ag NPs was also prepared (oleic-acid-capped Ag NP paste). The concentration of Ag NPs was set to 7.4 wt% in the paste in both cases. These pastes were used as Ag nanoink.

Poly(ethylene terephthalate) (PET) substrate (Toray, Lumirror S10 250 μm) was first washed by acetone and methanol. The fabricated Ag nanoink was cast onto the PET substrate (20 mm x 20 mm). This substrate was dipped in an organic solvent (20 mL) containing a sintering agent at RT (about 25 °C) under an air atmosphere (Figure 2-2). After the RT chemical sintering, the obtained Ag thin films (thickness ~5 μm) were dried in air for 120 min at RT before measurements such as SEM and electrical resistivity. For comparison, the Ag thin film was also prepared on the glass substrate from the oleic-acid-capped Ag NP paste by heating at 350 °C for 120 min in an electrical furnace (thermal sintering).

2-4-4 Characterization

TEM images were taken at 100 kV with a JEM-2100 (JEOL, Japan) for the observation of synthesized metal NPs. The diameter of NPs was evaluated by ImaegJ software. The morphology of Ag thin films was characterized by FE-SEM (JSM-6700F, JEOL, Japan). EDS was carried out by FE-SEM (JSM-7800F, JEOL, Japan) equipped with Octane Elect (AMETEK EDAX). Electrical resistivity was measured using a four-probe method (MCP-T370, Mitsubishi Chemical Analytech Co., Ltd., Japan). The thickness of Ag thin films was measured by laser microscopy (OLS4100, OLYMPUS, Japan). Electrical resistivity was evaluated to multiply sheet resistance by thickness. The absorption spectra were recorded by a UV-Vis spectrophotometer U-2010 (Hitachi, Japan) and V-730 (JASCO, Japan) at RT. The as-prepared after ligand exchanges (TOPO, OA, and DDT) were diluted to 0.018 g L^{-1}. The diluted samples were left to stand in quartz cell with PTFE cap for 20 h before measurements. The as-prepared samples after the ligand exchange were diluted with *n*-hexane for measurements of absorption spectra. TGA was carried out by a ThermoMass Photo (Rigaku, Japan). TICs for analysis of ligands adsorbed on Ag NPs were obtained from a GC-MS spectrometer, QP2010 Plus (Shimadzu, Japan). Here, Ultra ALLOY UA5-30M-0.25F (Frontier Laboratories Ltd., Japan) was used as a column. The samples for GC-MS were heated by a PY-3030D pyrolyzer (Frontier Laboratories Ltd., Japan) at 300 ˚C before injection. XRD patterns were recorded using a MiniFlexII (Rigaku, Japan, Cu Kα radiation) equipped with a Kα filter operating at 30 kV and 15 mA. The crystallite size was calculated by the Scherrer's equation: $D = 0.9\lambda/\beta\cos\theta$, where D is the crystallite size, λ is the wavelength of X-ray, β is the FWHM of diffraction peak, and θ is the diffraction angle. XPS measurements were carried out by a KRATOS AXIS Ultra DLD X-ray photoelectron spectrometer (Shimadzu, Japan).

Reference

[1] Wang, P.; Hu, M.; Wang, H. Chen, H.; Feng, Y.; Wang, J.; Ling, W.; Huang, Y. The evolution of flexible electronics: from nature, beyond nature, and to nature. *Adv. Sci.* **2020**, *7*, 2001116.

[2] Ankireddy, K.; Vunnam, S.; Kellar, J.; Cross, W. Highly conductive short chain carboxylic acid encapsulated silver nanoparticle based inks for direct write technology applications. *J. Mater. Chem. C* **2013**, *1*, 572–579.

[3] Perelaer, J.; de Gans, B.-J.; Schubert, U. S. Ink-jet printing and microwave sintering of conductive silver tracks. *Adv. Mater.* **2006**, *18*, 2101–2104.

[4] Perelaer, J.; Klokkenburg, M.; Hendriks, C. E.; Schubert, U. S. Microwave flash sintering of inkjet-printed silver tracks on polymer substrates. *Adv. Mater.* **2009**, *21*, 4830–4834.

[5] Perelaer, J.; Jani, R.; Grouchko, M.; Kamyshny, A.; Magdassi, S.; Schubert, U. S. Plasma and microwave flash sintering of a tailored silver nanoparticle ink, yielding 60% bulk conductivity on cost-effective polymer foils. *Adv. Mater.* **2012**, *24*, 3993–3998.

[6] Jung, S.; Chun, S. J.; Shon, C.-H. Rapid cellulose-mediated microwave sintering for high-conductivity Ag patterns on paper. *ACS Appl. Mater. Interfaces* **2016**, *8*, 20301–20308.

[7] Hong, S.; Yeo, J.; Kim, G.; Kim, D.; Lee, H.; Kwon, J.; Lee, H.; Lee, P.; Ko, S. H. Nonvacuum, maskless fabrication of a flexible metal grid transparent conductor by low-temperature selective laser sintering of nanoparticle ink. *ACS Nano* **2013**, *7*, 5024–5031.

[8] Theodorakos, I.; Zacharatos, F.; Geremia, R.; Karnakis, D.; Zergioti, I. Selective laser sintering of Ag nanoparticles ink for applications in flexible electronics. *Appl. Surf. Sci.* **2015**, *336*, 157–162.

[9] Suh, Y. D.; Kwon, J.; Lee, J.; Lee, H.; Jeong, S.; Kim, D.; Cho, H.; Yeo, J.; Ko, S. H. Maskless fabrication of highly robust, flexible transparent Cu conductor by random crack network assisted Cu nanoparticle patterning and laser sintering. *Adv. Electron. Mater.* **2016**, *2*, 1600277.

[10] Hwang, Y.-T.; Chung, W.-H.; Jang, Y.-R.; Kim, H.-S. Intensive Plasmonic Intensive plasmonic flash light sintering of copper nanoinks using a band-pass light filter for highly electrically conductive electrodes in

printed electronics. *ACS Appl. Mater. Interfaces* **2016**, *8*, 8591–8599.

[11] Park, S.-H.; Kim, H.-S. Flash light sintering of nickel nanoparticles for printed electronics. *Thin solid Films* **2014**, *550*, 575–581.

[12] Son, Y.-H.; Jang, J.-Y.; Kang, M.-K.; Ahn, S.; Lee, C. S. Application of flash-light sintering method to flexible inkjet printing using anti-oxidant copper nanoparticles. *Thin solid Films* **2018**, *656*, 61–67.

[13] Grouchko, M.; Kamyshny, A.; Mihailescu, C. F.; Anghel, D. F.; Magdassi, S. Conductive inks with a "Built-In" mechanism that enables sintering at room temperature. *ACS Nano* **2011**, *5*, 3354–3359.

[14] Peng, P.; Li, L.; Guo, W. F.; Hui, Z.; Fu, J.; Jin, C.; Liu, Y.; Zhu, Y. Room-temperature joining of silver nanoparticles using potassium chloride solution for flexible electrode application. *J. Phys. Chem. C* **2018**, *122*, 2704–2711.

[15] Hui, Z.; Liu, Y.; Guo, W.; Li, L.; Mu, N.; Jin, C.; Zhu, Y.; Peng, P. Chemical sintering of direct-written silver nanowire flexible electrodes under room temperature. *Nanotechnology* **2017**, *28*, 285703–28570.

[16] Shi, L.; Layani, M.; Cai, X.; Zhao, H.; Magdassi, S.; Lan, M. An inkjet printed Ag electrode fabricated on plastic substrate with a chemical sintering approach for the electrochemical sensing of hydrogen peroxide. *Sens. Actuators, B* **2018**, *256*, 938–945.

[17] Magdassi, S.; Grouchko, M.; Berezin, O.; Kamyshny, A. Triggering the sintering of silver nanoparticles at room temperature. *ACS Nano* **2010**, *4*, 1943–1948.

[18] Wakuda, D.; Hatamura, M.; Suganuma, K. Novel method for room temperature sintering of Ag nanoparticle paste in air. *Chem. Phys. Lett.* **2007**, *441*, 305–308.

[19] Wakuda, D.; Kim, K.-S.; Suganuma, K. Room-temperature sintering of Ag nanoparticles paste. *IEEE Trans. Compon., Packag. Technol.* **2009**, *32*, 627–632.

[20] Saponjic, Z. D.; Csencsits, R.; Rajh, T.; Dimitrijevic, N. M. Self-assembly of TOPO-derivatized silver nanoparticles into multilayered film. *Chem. Mater.* **2003**, *15*, 4521–4526.

[21] Yamamoto, M.; Kashiwagi, Y.; Nakamoto, M. Size-controlled synthesis of monodispersed silver nanoparticles

capped by long-chain alkyl carboxylates from silver carboxylate and tertiary amine. *Langmuir* **2006**, *22*, 8581–8586.

[22] Dong, P.; Fisher, E. A.; Meli, M.-V.; Trudel, S. Tuning the magnetism of gold nanoparticles by changing the thiol coating. *Nanoscale* **2020**, *12*, 19797–19803.

[23] Chen, M.; Feng, Y.-G.; Wang, X.; Li, T.-C.; Zhang, J.-Y.; Qian, D.-J. Silver nanoparticles capped by oleylamine: formation, growth, and self-organization. *Langmuir* **2007**, *23*, 5296–5304.

[24] Ienaga, T.; Okada, S.; Nakahara, Y.; Watanabe, M.; Tamai, T.; Yajima, S.; Kimura, K. Comparison of physical adsorption strength of protective agents via ligand exchange of silver nanoparticles prepared by vacuum evaporation on running oil substrate. *Bull. Chem. Soc. Jpn.* **2017**, *90*, 1251–1258.

[25] Ienaga, T.; Nakahara, Y.; Kimura, K. Synthesis and characterization of silver nanoparticles by vacuum evaporation on running hydrocarbon solution containing nonionic surfactant in cylindrical glass chamber. *Chem. Lett.* **2014**, *43*, 1893–1895.

[26] Ienaga, T.; Nakahara, Y.; Yajima, S.; Kimura, K. Effect of protective agents on silver nanoparticle preparation by vacuum evaporation on running hydrocarbon solution. *J. Nanosci. Nanotechnol.* **2018**, *18*, 2547–2554.

[27] Rycenga, M.; Cobley, C. M.; Zeng, J.; Li, W.; Moran, C. H.; Zhang, Q.; Qin, D.; Xia, Y. Controlling the synthesis and assembly of silver nanostructures for plasmonic applications. *Chem. Rev.* **2011,** *111*, 3669–3712.

[28] Gromova, M.; Lefrançois, A.; Vaure, L.; Agnese, F.; Aldakov, D.; Maurice, A.; Djurado, D.; Lebrun, C.; de Geyer, A.; Schülli, T. U.; Pouget, S.; Reiss, P. Growth mechanism and surface state of $CuInS_2$ nanocrystals synthesized with dodecanethiol. *J. Am. Chem. Soc.* **2017**, *139*, 15748–15759.

[29] Scherrer, P. *Göttinger Nachrichten 2* **1918**, 98–100.

[30] Klug, H. P.; Alexander, L. E. *X-ray Diffraction Procedures, 2nd ed.*; Wiley: New York, 1973.

[31] Yamamoto, M.; Kashiwagi, Y.; Nakamoto, M. Size-controlled synthesis of monodispersed silver nanoparticles capped by long-chain alkyl carboxylates from silver carboxylate and tertiary amine. *Langmuir* **2006**, *22*, 8581–8586.

[32] José-Yacamán, M.; Gutierrez-Wing, C.; Miki, M.; Yang, D.-Q.; Piyakis, K. N.; Sacher, E. Surface diffusion and coalescence of mobile metal nanoparticles. *J. Phys. Chem. B* **2005**, *109*, 9703–9711.

[33] Luehrs, D. C.; Iwamoto, R. T.; Kleinberg. J. Solubility of silver halides and stability of silver halide complexes in selected nonaqueous media. *Inorg. Chem.* **1966**, *5*, 201–204.

[34] Kogan, V. B.; Fridman, V. M.; Kafarov, V. V. *Solubility Handbook-T. 1, KH 1*; AH CCCP: Moscow, USSR, 1961.

[35] Nissen, K. E.; Stevens, M. G.; Stuart, B. H.; Baker, A. T. Characterization of PET films modified by tetraethylenepentamine (TTEPA). *J. Polym. Sci., Part B: Polym. Phy.* **2001**, *39*, 623–633.

[36] Wang, P.; Huang, B.; Zhang, X.; Qin, X.; Dai, Y.; Wang, Z.; Lou, Z. Highly efficient visible light plasmonic photocatalysts Ag@Ag(Cl, Br) and Ag@AgCl-AgI. *ChemCatChem* **2011**, *3*, 360–364.

[37] Gao, X.-Y.; Wang, S.-Y.; Li, J.; Zheng, Y.-X.; Zhang, R.-J.; Zhou, P.; Yang, Y.-M.; Chen, L.-Y. Study of structure and optical properties of silver oxide films by ellipsometry, XRD and XPS methods. *Thin solid Films* **2004**, *455-456*, 438–442.

[38] Zhu, M.; Chen, P.; Liu, M. Ag/AgBr/Graphene oxide nanocomposite synthesized via oil/water and water/oil microemulsions: A comparison of sunlight energized plasmonic photocatalytic activity. *Langmuir* **2012**, *28*, 3385–3390.

[39] Zhu, M.; Chen, P.; Liu, M. Graphene oxide enwrapped Ag/AgX (X = Br, Cl) nanocomposite as a highly efficient visible-light plasmonic photocatalyst. *ACS Nano* **2011**, *5*, 4529–4536.

[40] Zhang, H.; Wang, G.; Chen, D.; Lv, X.; Li, J. Tuning photoelectrochemical performances of Ag−TiO_2 nanocomposites via reduction/oxidation of Ag. *Chem. Mater*. **2008**, *20*, 6543–6549.

[41] Hoflund, G. B.; Hazos, Z. F.; Salaita, G. N. Surface characterization study of Ag, AgO, and Ag_2O using X-ray photoelectron spectroscopy and electron energy-loss spectroscopy. *Phys. Rev. B* **2000**, *62*, 11126–11133.

Chapter 3: RT Chemical Sintering of Cu-Ag Core-Shell NPs and Their Conductivity

Section 3-1: Introduction

Printed electronics have attracted much interest for the fabrication of fine conductive patterns on flexible substrates [1-4]. Metal NP pastes are often used as nanoinks in printed electronics [5]. The fine conductive patterns are obtained by the coalescence. The Ag NP ink is most frequently used because of its high conductivity and oxidation resistance. However, Ag is relatively expensive and short circuit often occurs in its fine patterns [6]. This phenomenon is called the electromigration effect and is a characteristic feature of Ag. These days, Ag is being replaced with copper (Cu), which is relatively inexpensive and shows less electromigration effect. The sintering of Cu NPs has to be carried out under an inert gas (e.g. Ar and N_2) and a reducing gas (e.g. formic acid and H_2) because Cu is easily oxidized by oxygen in air [7-11]. These problems can be simultaneously solved by using Cu-Ag core-shell (Cu@Ag) NPs [12-14] because Cu@Ag NPs have the properties of both migration and oxidation resistances originated from Cu and Ag, respectively.

The RT chemical sintering method can be carried out without heating, as shown in Chapter 2. In this method, sintering agents are used to desorb organic ligands easily from metal NPs. When organic ligands desorb from metal NP, metal NPs coalesce even at RT. To the best of the author's knowledge, the report by Dai *et al*. is the sole example of the RT chemical sintering of Cu@Ag NPs [15]. In the paper, oleylamine-capped Cu@Ag NPs were prepared and they were sintered at RT by dipping into water containing NaOH as a sintering agent and $NaBH_4$ as a reducing agent. However, the milder conditions for the RT chemical sintering are desirable from the viewpoint of the protection from metal oxidation and substrate denaturation.

In Chapter 2, the author reported that TOPO-capped Ag NPs were effectively coalesced by centrifugation with methanol. In addition, the RT chemical sintering of TOPO-capped Ag NPs was carried out by dipping into methanol containing a halide salt. The electrical resistivity of the obtained Ag thin films was comparable to that of the Ag thin film prepared by the heating at 350 °C. These results showed that a halide salt effectively worked as a sintering agent of TOPO-capped Ag NPs in methanol. On the basis of these backgrounds, the author created a new strategy for the fabrication of conductive thin films with both migration and oxidation resistances on the plastic substrate in this chapter. The outline of the strategy is shown in Figure 3-1. First, TOPO-capped Cu@Ag NPs were prepared by the ligand exchange. The obtained precipitate was dried in air and evaluated by transmission electron microscopy (TEM), field emission scanning electron microscopy (FE-SEM), X-ray diffraction (XRD), and X-ray photoelectron spectroscopy (XPS). Then, Cu/Ag thin films were fabricated at RT from TOPO-capped Cu@Ag NPs by dipping into methanol containing a sintering agent and/or a reducing agent. As TOPO easily desorbs from Ag NP in methanol, the coalescence of Cu@Ag NPs proceeds even at RT with the aid of a sintering agent. In addition, a reducing agent protects metals from the oxidation during the RT process. Here, various combinations of sintering agents such as cetyltrimethylammonium chloride (CTAC) and HCl, and/or reducing agents such as oxalic acid, malonic acid, and hydrazine were examined for the RT chemical sintering of Cu@Ag NPs. Mild reagents were selected for the protection from metal oxidation and substrate denaturation. As for the obtained Cu/Ag thin film under the optimal conditions, the morphology and electrical resistivity were investigated.

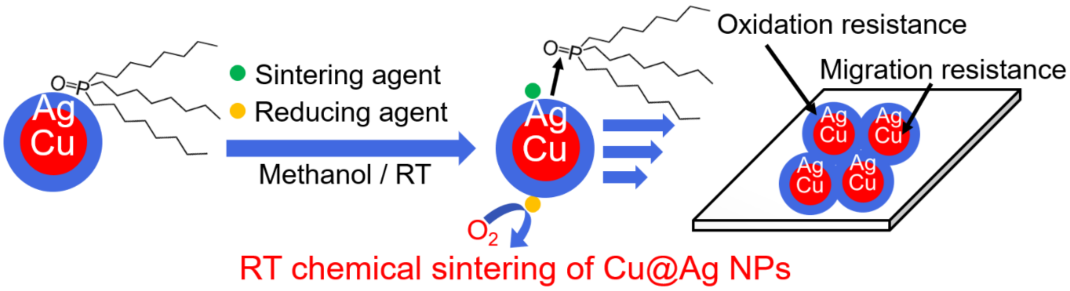

Figure 3-1. Preparation of conductive thin films with both migration and oxidation resistances on the plastic substrate by the RT chemical sintering of TOPO-capped Cu@Ag NPs in methanol containing a sintering agent and/or a reducing agent.

Section 3-2: Results and Discussion

3-2-1 Cu-Ag Core-Shell NPs before and after Ligand Exchange with TOPO

The synthesis of Cu@Ag NPs was carried out based on the method reported by Muzikansky *et al* [16]. First, oleylamine-capped Cu NPs were synthesized by the thermal decomposition method. Next, oleylamine/oleic-acid-capped Cu@Ag NPs were synthesized by the galvanic replacement method. Then, the ligand exchange from oleylamine/oleic acid to TOPO were performed on the NP surface (Figure 3-2). As for Cu@Ag NPs before and after the ligand exchange, TEM observation was carried out (Figure 3-3). From the analysis of TEM images, the average diameters of Cu@Ag NPs before (Figure3-3a) and after (Figure3-3c) the ligand exchange were determined to be 5.8 ± 2.6 nm (Figure 3-3b) and 5.5 ± 1.9 nm (Figure 3-3d), respectively. These results indicate that the morphology of Cu@Ag NPs remained unchanged before and after the ligand exchange. Although some bigger NPs were also observed before and after the ligand exchange, they already existed before the galvanic replacement reaction (Figure 3-4). Noticeably, about 15 nm of NPs decreased and about 10 nm of NPs increased instead after the ligand exchange. The fact may be due to the size decrease of bigger Cu@Ag NPs based on the partial dissolution, judging from the fact that the supernatant in the washing process after the ligand exchange was a blue color originated from Cu^{2+}. The elemental molar ratio Cu/Ag of synthesized Cu@Ag NPs was determined to be 95/5 mol/mol% by X-ray fluorescence (XRF) analysis.

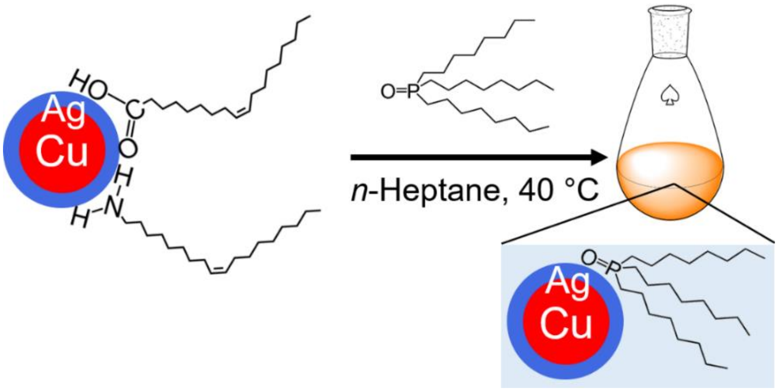

Figure 3-2. Ligand exchange of Cu@Ag NP from oleylamine/oleic acid to TOPO.

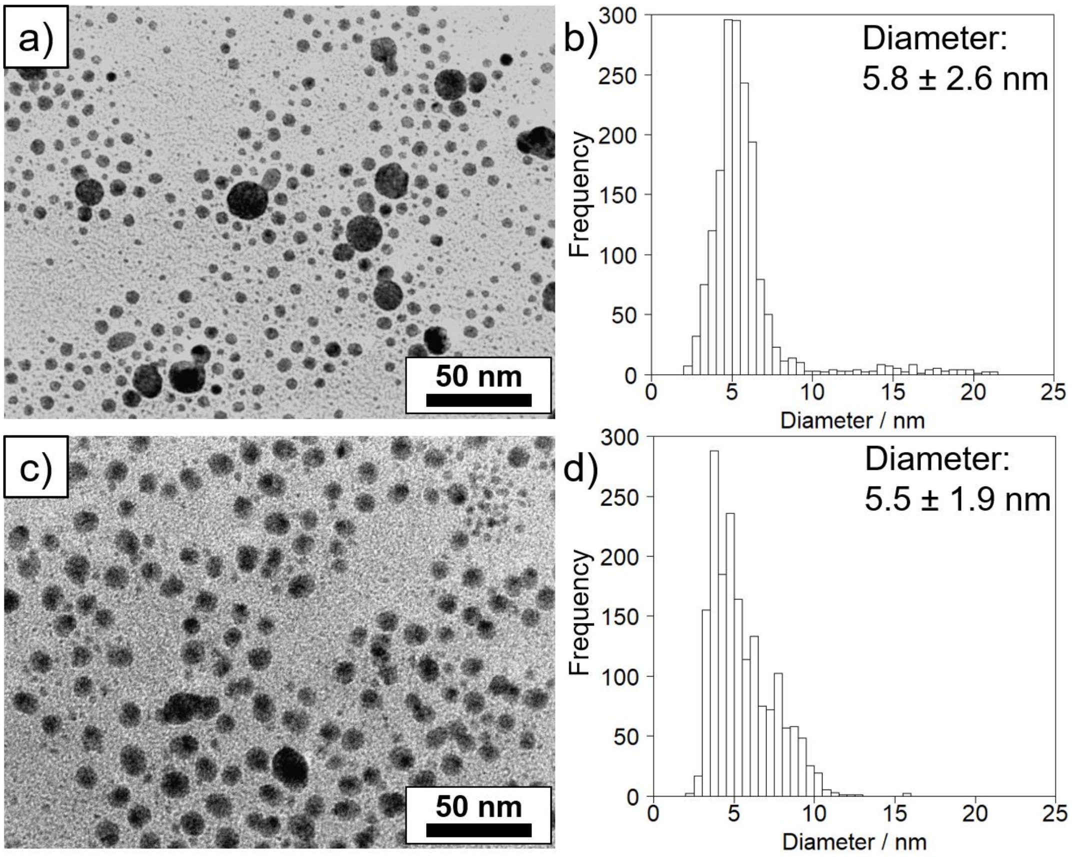

Figure 3-3. (a), (c) TEM images and (b), (d) particle size distributions of (a), (b) oleylamine/oleic-acid-capped Cu@Ag NPs and (c), (d) TOPO-capped Cu@Ag NPs.

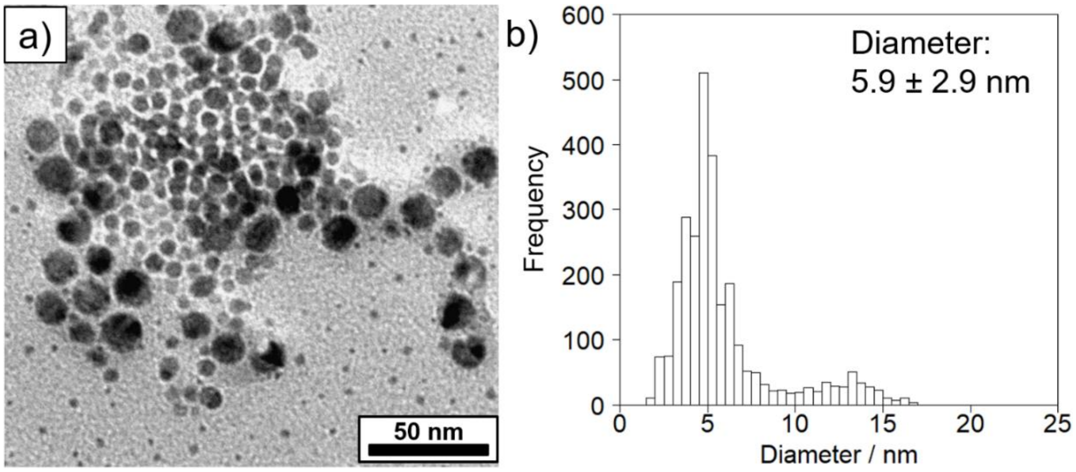

Figure 3-4. (a) TEM image and (b) particle size distribution of oleylamine-capped Cu NPs.

The absorption spectra of Cu@Ag NPs were measured before and after the ligand exchange with TOPO. The as-prepared samples after the ligand exchange were diluted with *n*-heptane. As a reference, oleylamine-capped Cu NPs was also measured under the same conditions. Their absorption spectra are shown in Figure 3-5. The absorption peaks at around 420 nm and 566 nm were originated from localized surface plasmon resonance of Ag and Cu, respectively [16]. On the other hand, the absorption peak of oleylamine-capped Cu NPs was observed at 579 nm. The hypsochromic shift based on the covering of Cu with Ag has also been reported by Muzikansky *et al* [16]. Even after the ligand exchange with TOPO, broadening of absorption peaks based on the aggregation of NPs was hardly observed. This result shows that TOPO-capped Cu@Ag NPs stably dispersed in a nonpolar solvent.

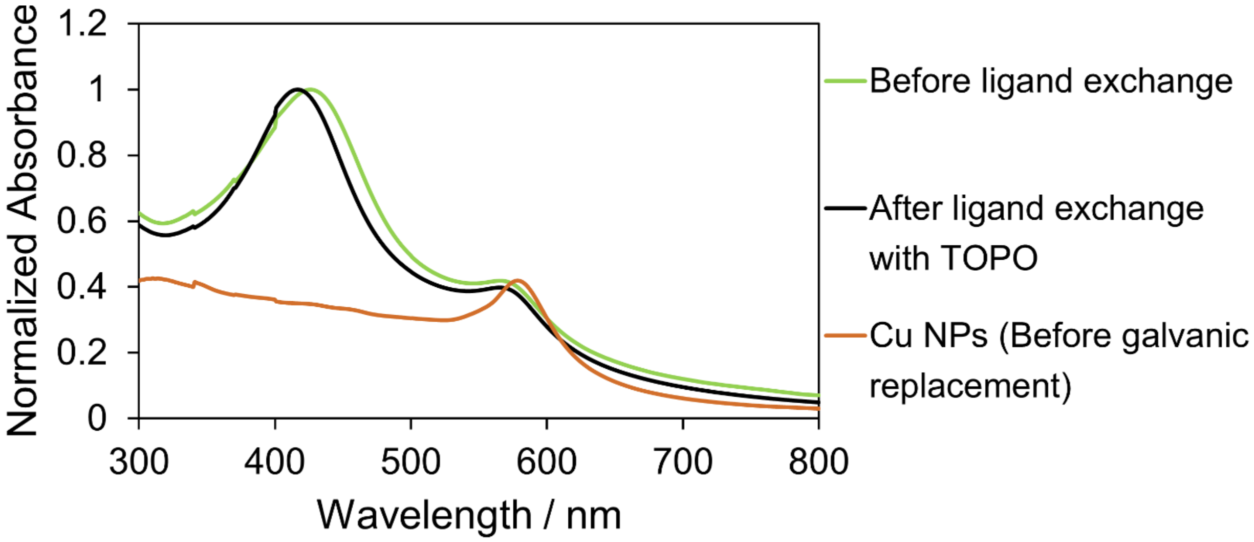

Figure 3-5. Absorption spectra of Cu@Ag NPs before and after the ligand exchange from oleylamine/oleic acid to TOPO, and oleylamine-capped Cu NPs before the galvanic replacement.

The ligand exchange to TOPO was confirmed by pyrolysis gas chromatograph mass spectrometry (GC-MS) measurements of the precipitates of Cu@Ag NPs after the RT chemical sintering. Figure 3-6 shows total ion chromatographs (TICs) of the used ligands and Cu@Ag NPs before and after the ligand exchange. Although the peaks of oleylamine and oleic acid were clearly detected in the case of Cu@Ag NPs before the ligand exchange, they were not detected after the ligand exchange. This result indicates that the ligand exchange from oleylamine/oleic acid to TOPO proceeded on the surface of Cu@Ag NP. However, the peak of TOPO was not detected after the ligand exchange. In the section 2-2-3, the desorption temperature (350 °C) of TOPO from the Ag NP surface was significantly higher than the thermal decomposition temperature (295 °C) of TOPO. Therefore, TOPO on the Cu@Ag NP surface also may be decomposed before its vaporization. The removal of TOPO induces the coalescence of Cu@Ag NPs in the subsequent RT chemical sintering after the ligand exchange.

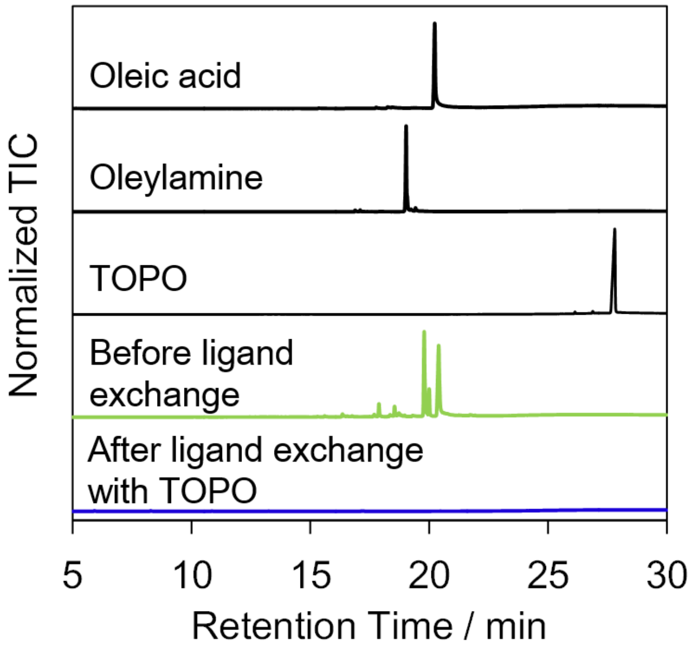

Figure 3-6. TICs of oleic acid, oleylamine, TOPO, and Cu@Ag NPs before and after the ligand exchange from oleylamine/oleic acid to TOPO.

Next, attenuated total reflection infrared (ATR-IR) spectra of oleic acid, oleylamine, TOPO, and Cu@Ag NPs before and after the ligand exchange with TOPO were measured to clarify the presence of TOPO on the surface of Cu@Ag NP (Figure 3-7). In the IR spectrum of Cu@Ag NPs after the ligand exchange, the peaks originated from oleylamine and oleic acid were not detected and the characteristic band associated with P=O was observed at around 1100 cm^{-1} instead. Furthermore, XPS spectra of Cu@Ag NPs before and after the ligand exchange with TOPO showed the existence of P atoms only after the ligand exchange (Figure 3-8). These experimental facts clearly demonstrate the progress of the ligand exchange. In Chapter 2, the author reported that adsorption strength of TOPO to the Ag surface was larger than those of oleylamine and oleic acid.

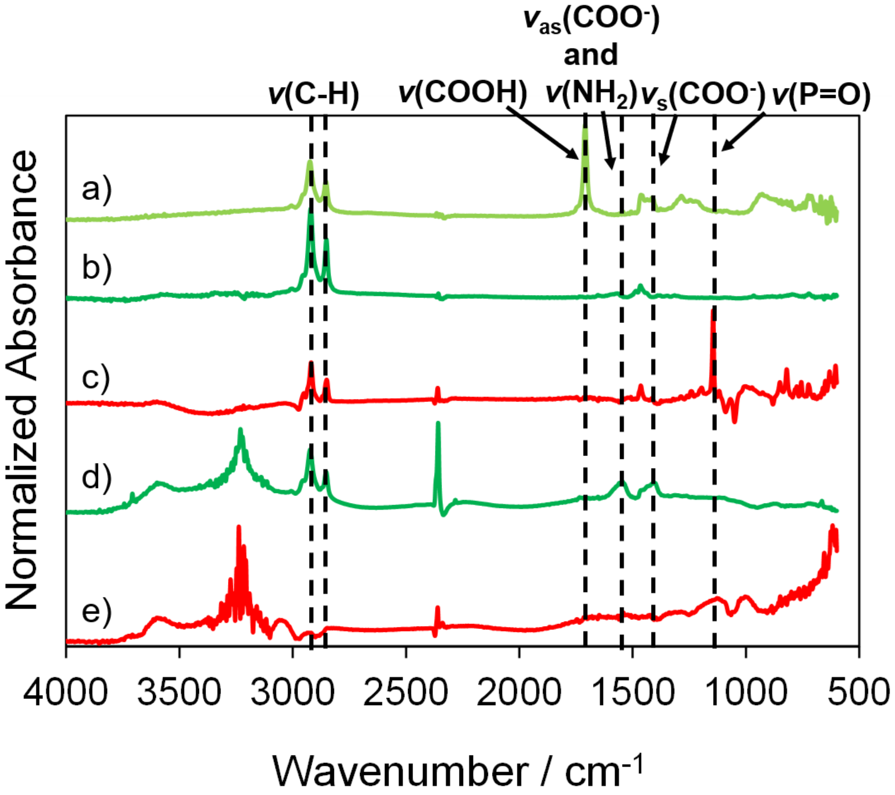

Figure 3-7. ATR-IR spectra of (a) oleic acid, (b) oleylamine, (c) TOPO, and Cu@Ag NPs (d) before and (e) after the ligand exchange from oleylamine/oleic acid to TOPO.

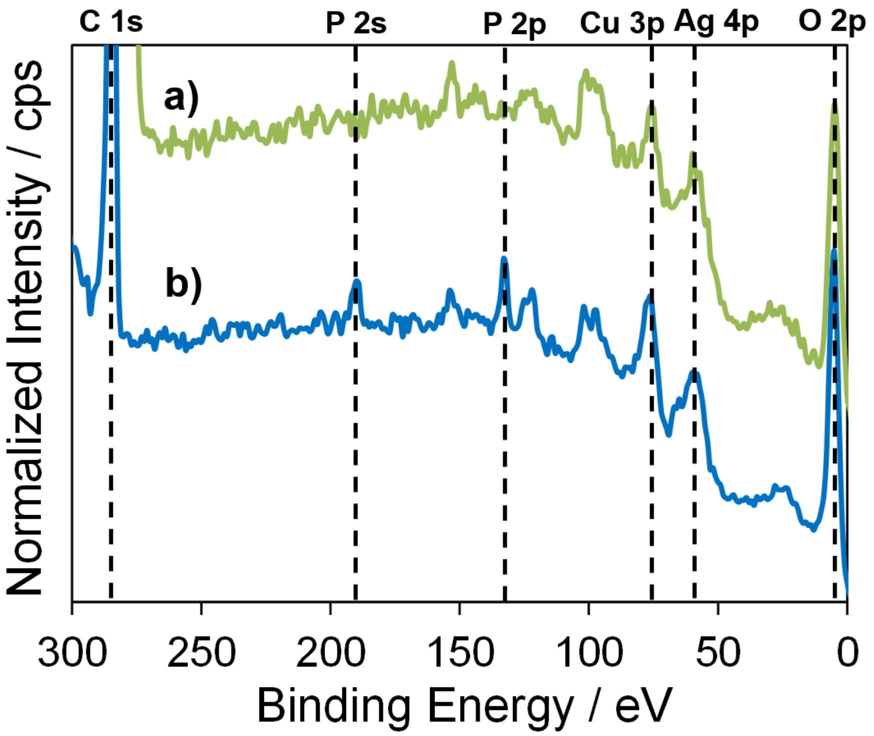

Figure 3-8. XPS spectra of Cu@Ag NPs (a) before and (b) after the ligand exchange from oleylamine/oleic acid to TOPO.

3-2-2 Cu-Ag Core-Shell Precipitates after Ligand Exchange and Subsequent Washing Process

The concentrated TOPO dispersion of Cu@Ag NPs was used without purification as the paste for the metal NP ink. The paste was also used to investigate the coalescence of Cu@Ag NPs as a model experiment for the actual RT sintering (Figure 3-9). In the model experiment, the methanol solution containing a sintering agent and/or a reducing agent was added to the paste. The precipitate was collected by centrifugation, which corresponds to the washing process in the actual RT sintering. After the ligand exchange and subsequent washing process, the precipitates of Cu@Ag NPs were used for pyrolysis GC-MS to investigate the progress of ligand exchanges. After the ligand exchange and subsequent washing process, TEM observation of the precipitate of Cu@Ag NPs was carried out. Figure 3-10 shows the neck-like structure formed by coalescence of Cu@Ag NPs (Figure 3-10a). The crystal reconstruction and growth in the neck was due to the surface diffusion of atoms (Figure 3-10b) [17, 18]. Thus, coalescence of NPs causes the increase in crystallite size.

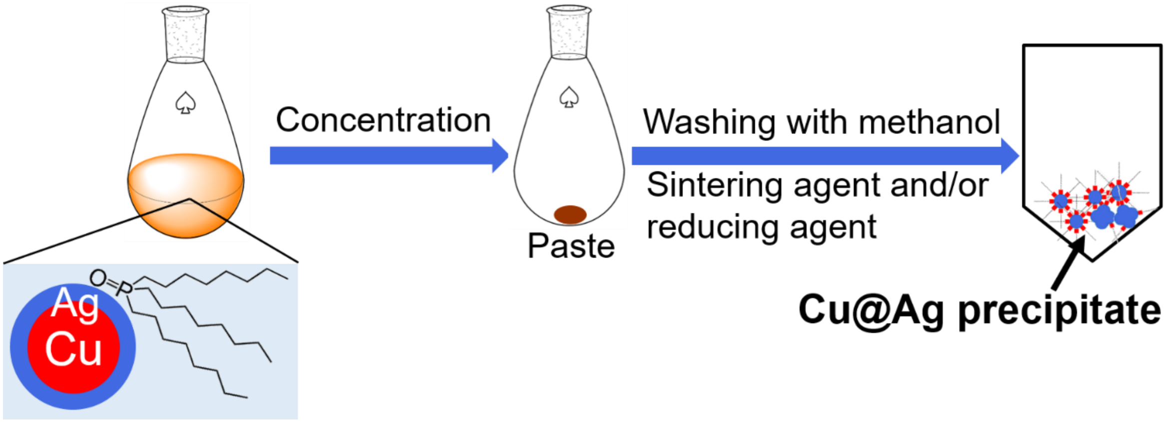

Figure 3-9. Ligand exchange and subsequent washing process of the paste of TOPO-capped Cu@Ag NPs with methanol containing a sintering agent and/or a reducing agent.

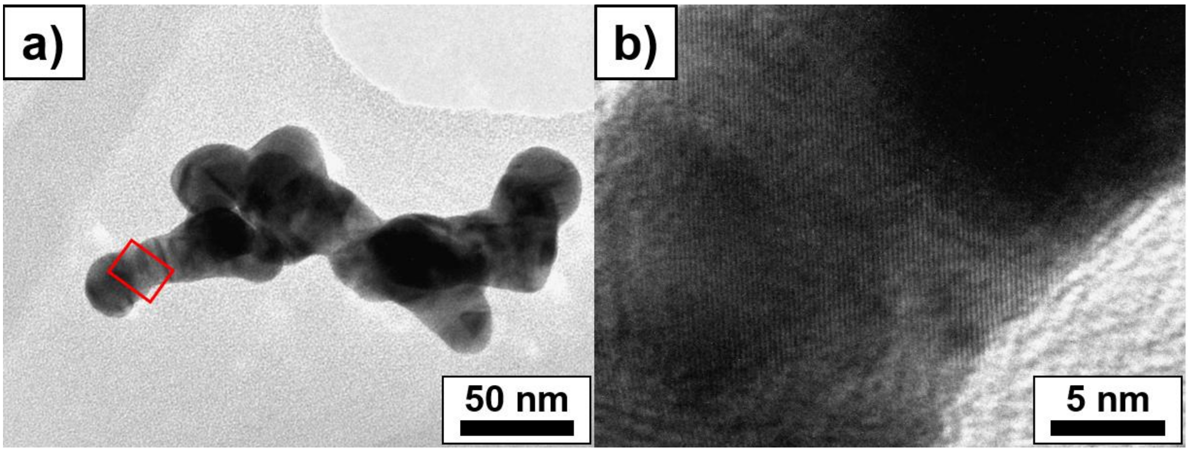

Figure 3-10. (a) TEM images of the precipitate of Cu@Ag NPs after the washing process using the 29 mM HCl methanol solution. (b) A high magnification image of the red square area in (a)

The crystallite sizes of the precipitates of Cu@Ag NPs were evaluated by PXRD (Figure 3-11A). For comparison, the precipitates of TOPO-capped Ag NPs prepared by the same method were also examined (Figure 3-11B). In the RT chemical sintering, various combinations of sintering agents and/or reducing agents were added into methanol during the washing process (Figure 3-12). Here, CTAC and HCl, which have a chloride ion, were used as sintering agents. Chloride ion has often been used as a sintering agent of Ag NPs [19-22]. Oxalic acid and malonic acid were used as an acidic reducing agent, and hydrazine was used as a basic reducing agent. In all the cases, the diffraction peaks at $2\theta = 38°$, 44°, 64°, and 77° were identified as the (111), (200), (220), and (311) planes of face-centered cubic Ag, respectively [23]. In addition, the diffraction peak of face-centered cubic Cu (111) ($2\theta = 43°$) overlapped that of Ag (200) [13]. The crystallite sizes were calculated based on the Scherrer equation using FWHM of the diffraction peaks at Ag (111) [23]. The calculated values of crystallite sizes are summarized in Table 3-1. In the absence of sintering agents and reducing agents, the crystallite size of the precipitate of Cu@Ag NPs slightly increased compared with that of Cu@Ag NPs before the ligand exchange. In the cases of CTAC, HCl, oxalic acid, and malonic acid, the crystallite sizes significantly increased. In the case of hydrazine, however, the crystallite size slightly increased. On the other hand, the crystallite sizes of the precipitates of Ag NPs significantly increased in all the cases. These contrasting results indicate that the interaction between TOPO and the metal NP surface changes with the existence of Cu. The interaction of TOPO with the Cu@Ag NP surface would be stronger than that with the Ag NP surface. In fact, the increase in the crystallite size of Cu@Ag NP was much smaller than that of Ag NPs in the cases of methanol only.

Table 3-1. Crystallite sizes of the precipitates of Cu@Ag NPs at Ag (111) and the precipitates of Ag NPs after the washing process using methanol containing a sintering agent and/or a reducing agent.

Added agents	Crystallite size ± standard error (nm)	
	Cu@Ag NPs	Ag NPs
Before ligand exchange	2.8 ± 0.1	4.2 ± 0.1
No addition (methanol only)	4.2 ± 0.3	12.6 ± 0.4
1.0 mM CTAC	13.4 ± 0.1	18.6 ± 0.3
29 mM HCl	12.2 ± 0.2	26.9 ± 0.3
100 mM oxalic acid + 1.0 mM CTAC	14.1 ± 0.4	20.4 ± 0.5
100 mM malonic acid + 1.0 mM CTAC	16.4 ± 0.1	25.8 ± 0.8
100 mM hydrazine + 1.0 mM CTAC	5.4 ± 0.1	17.7 ± 0.4

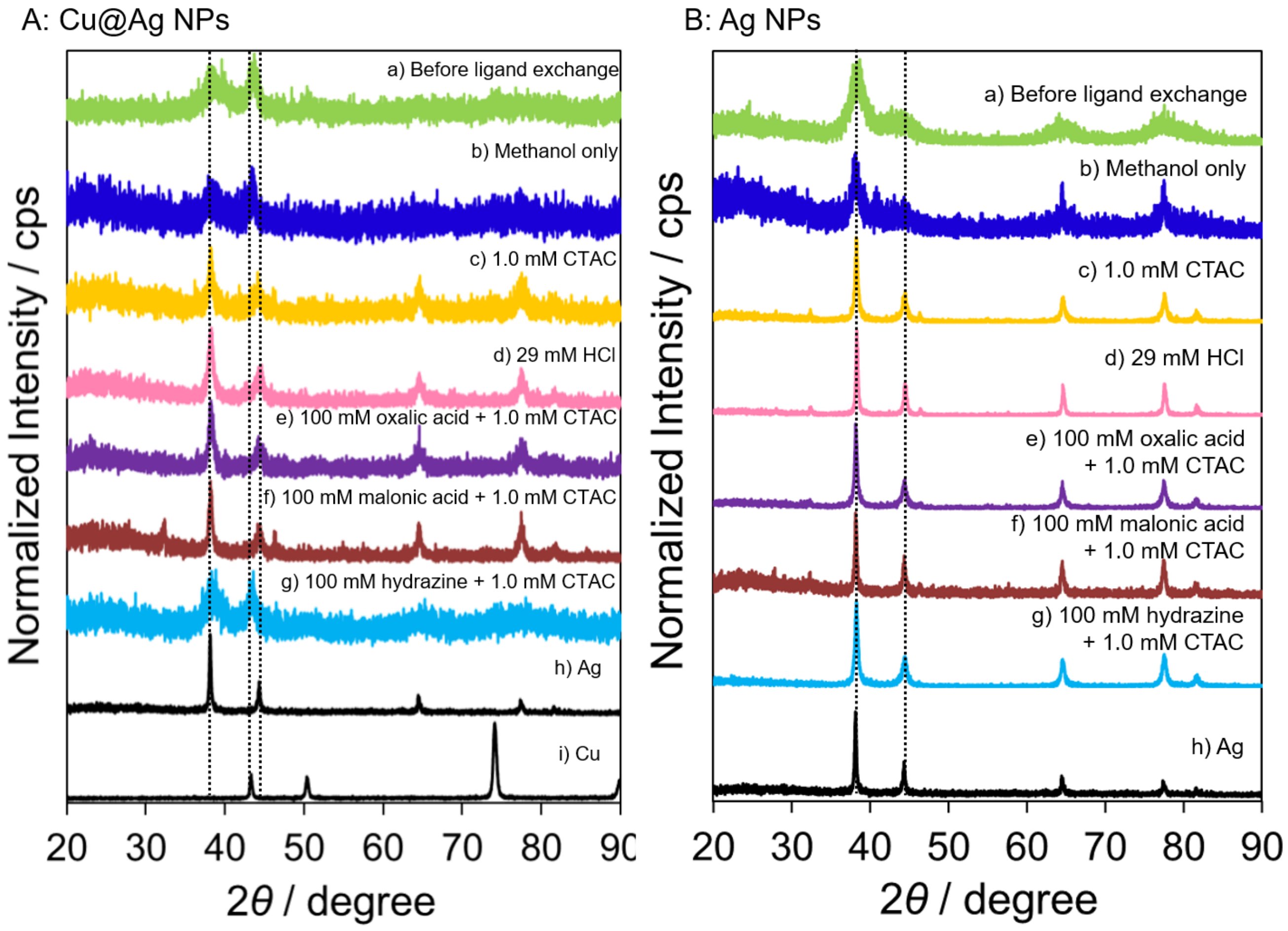

Figure 3-11. PXRD patterns of (A) Cu@Ag NPs and (B) Ag NPs (a) before the ligand exchange, and the precipitates of Cu@Ag NPs and Ag NPs after the washing process using methanol in the (b) absence and presence of (c) 1.0 mM CTAC, (d) 29 mM HCl, (e) 100 mM oxalic acid + 1.0 mM CTAC, (f) 100 mM malonic acid + 1.0 mM CTAC, and (g) 100 mM hydrazine + 1.0 mM CTAC. Reference patterns of (h) bulk Ag and (i) bulk Cu.

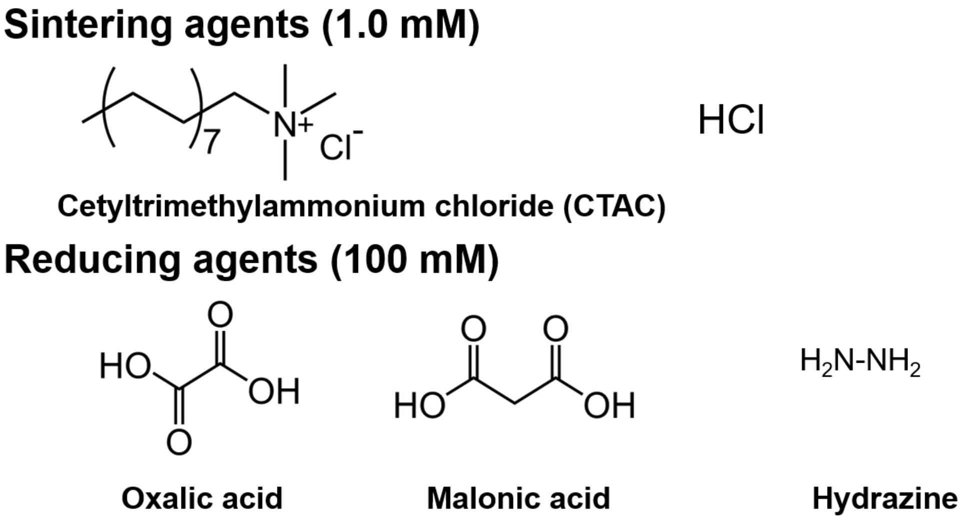

Figure 3-12. Chemical structures of sintering agents and/or reducing agents.

Next, SEM images of the precipitates after the washing process were observed (Figure 3-13). The significant coalescence of Cu@Ag NPs was observed only in the case of 29 mM HCl (Figure 3-13c). When CTAC, malonic acid, and hydrazine were added into methanol, the coalescence of Cu@Ag NPs moderately proceeded (Figure 3-13b, 3-13e, and 3-13f). In the SEM and TEM images for the washing process using methanol only (Figure 3-13a and 3-14), the NPs hardly coalesced. Organic acicular crystals (red arrow points) clearly remained in the case of oxalic acid (Figure 3-13d). To confirm the point, the amounts of organic compounds in the precipitates after washing process were evaluated by thermogravimetric analysis (TGA) (Figure 3-15). Heating was performed under helium atmosphere at a rate of 10 °C min^{-1} in the temperature range from 28 to 500 °C. When HCl and hydrazine were added into methanol, the weight loss significantly decreased compared with that of Cu@Ag NPs before the ligand exchange. This result shows that most of the organic compounds such as oleylamine, oleic acid and TOPO were removed during the washing process. In addition, HCl and hydrazine are volatile compounds and soluble in methanol and then may not remain in the precipitates. On the other hand, when oxalic acid was added, the weight loss was higher than that of Cu@Ag NPs before the ligand exchange. It seems that the thermal decomposition at 320 °C brought about the formation of Cu(II) oxalate because the characteristic TG curve in the case of 100 mM oxalic acid and 1.0 mM CTAC was in good agreement with that of Cu(II) oxalate [24].

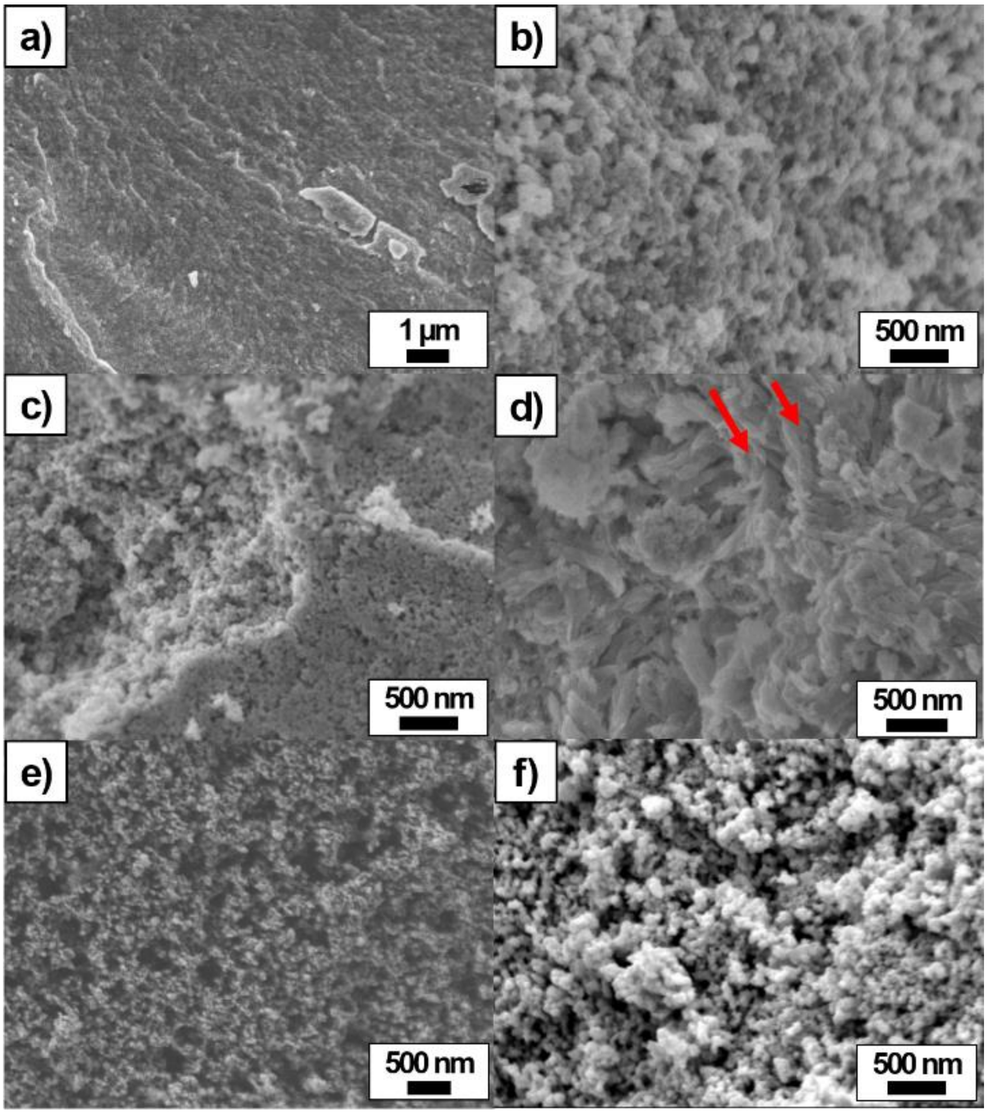

Figure 3-13. SEM images of Cu@Ag NPs after the washing process using methanol in the (a) absence and presence of (b) 1.0 mM CTAC, (c) 29 mM HCl, (d) 100 mM oxalic acid + 1.0 mM CTAC, (e) 100 mM malonic acid + 1.0 mM CTAC, and (f) 100 mM hydrazine + 1.0 mM CTAC.

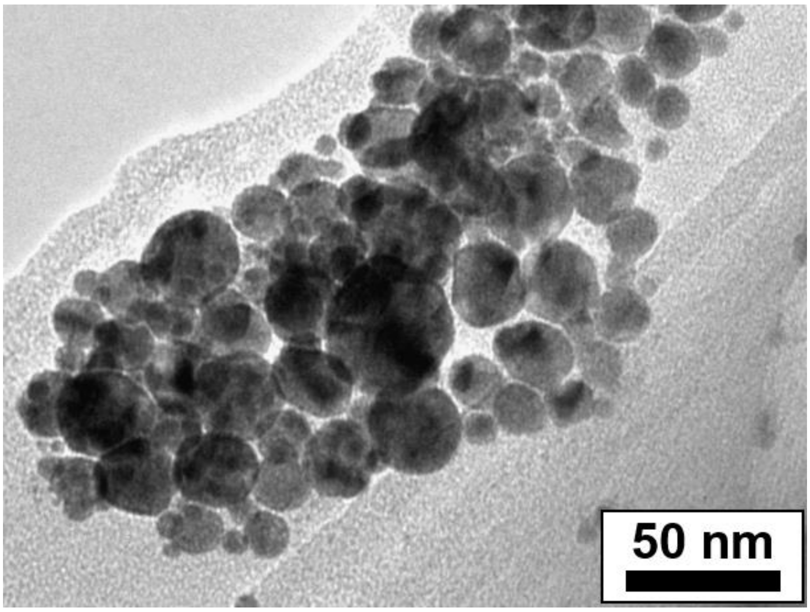

Figure 3-14. TEM image of the precipitates of Cu@Ag NPs after the washing process using methanol only.

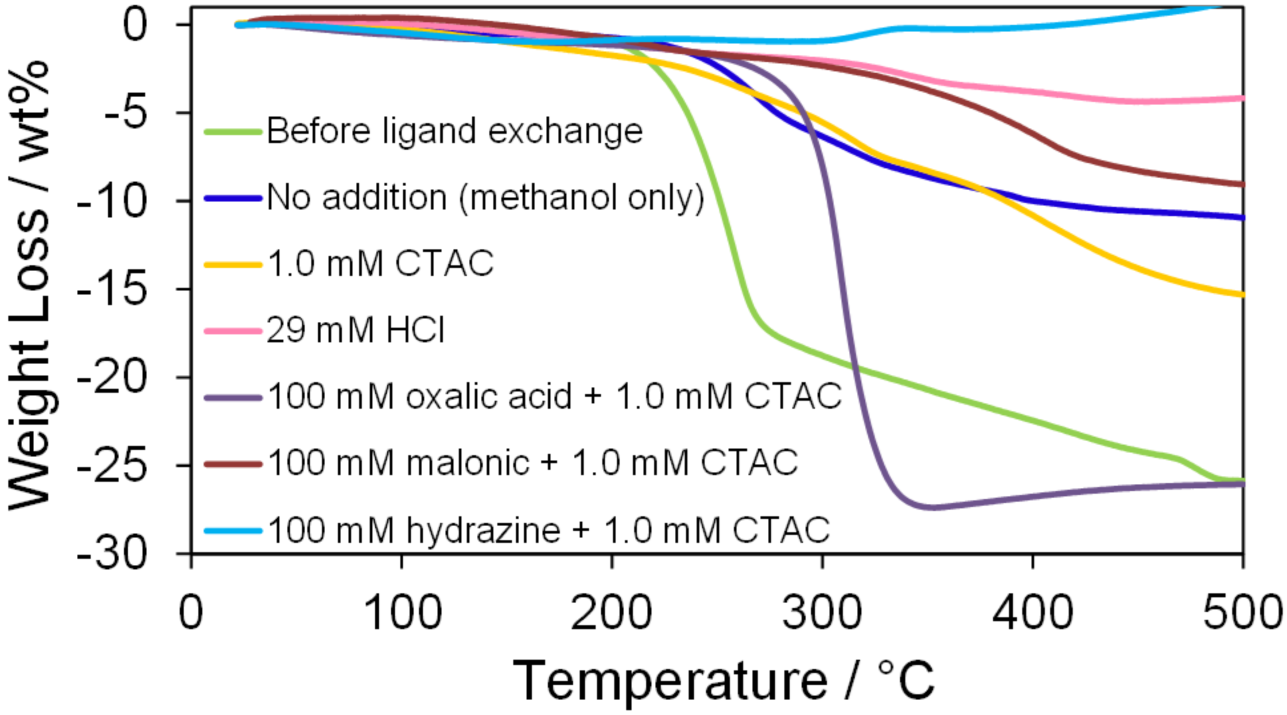

Figure 3-15. TGA curves of the precipitates of Cu@Ag NPs after the washing process using methanol containing a sintering agent and/or a reducing agent.

The elemental composition of the precipitates of Cu@Ag NPs after the RT chemical sintering was analyzed by XPS. The peaks at 368.5 eV and 374.5 eV were identified as Ag $3d_{5/2}$ and Ag $3d_{3/2}$ in Ag^0, respectively (Figure 3-16A). On the other hand, the peaks at 367.9 eV and 373.9 eV were identified as Ag $3d_{5/2}$ and Ag $3d_{3/2}$ in Ag^+, respectively [13, 25, 26]. In all the cases, the peaks of Ag^0 were observed. In the cases of 29 mM HCl and 100 mM hydrazine + 1.0 mM CTAC (Figure 3-16A d and g), the peaks of Ag^+ were not observed although the peaks were clearly detected in the other cases. The addition of HCl or hydrazine did not induce the oxidation of Ag. The peaks at 932.3 eV and 933.9 eV in Cu 2p were identified as Cu^0 or Cu_2O, and CuO, respectively (Figure 3-16B) [13, 27, 28]. In all the cases, the peaks of Cu^0 or Cu_2O, and CuO were observed. In the case of oxalic acid, the peak at 935.3 eV in Cu 2p was identified as $Cu(COO)_2$ (Figure 3-16B e) [29] because the C 1s peak originated from COO^- was detected at 289.1 eV (Figure 3-17) [30]. This result also supports the existence of Cu(II) oxalate, as shown in the SEM image (Figure 3-13d) and the TGA curve (Figure 3-15). It is noticeable that the peak of CuO existed before the ligand exchange. This fact demonstrates that a small part of Cu was already oxidized at the time of synthesis of Cu NPs, which are coexistence of Cu^0 or Cu_2O, and CuO. The further oxidation of Cu and Cu_2O slightly proceeded in all the cases. The result indicates that Cu NPs were almost covered with the Ag shell. The above-mentioned results show that HCl is the most suitable as a sintering agent for the RT chemical sintering of Cu@Ag NPs in terms of the increase of crystallite size, almost complete removal of organic compounds, and suppression of Ag and Cu significant oxidation.

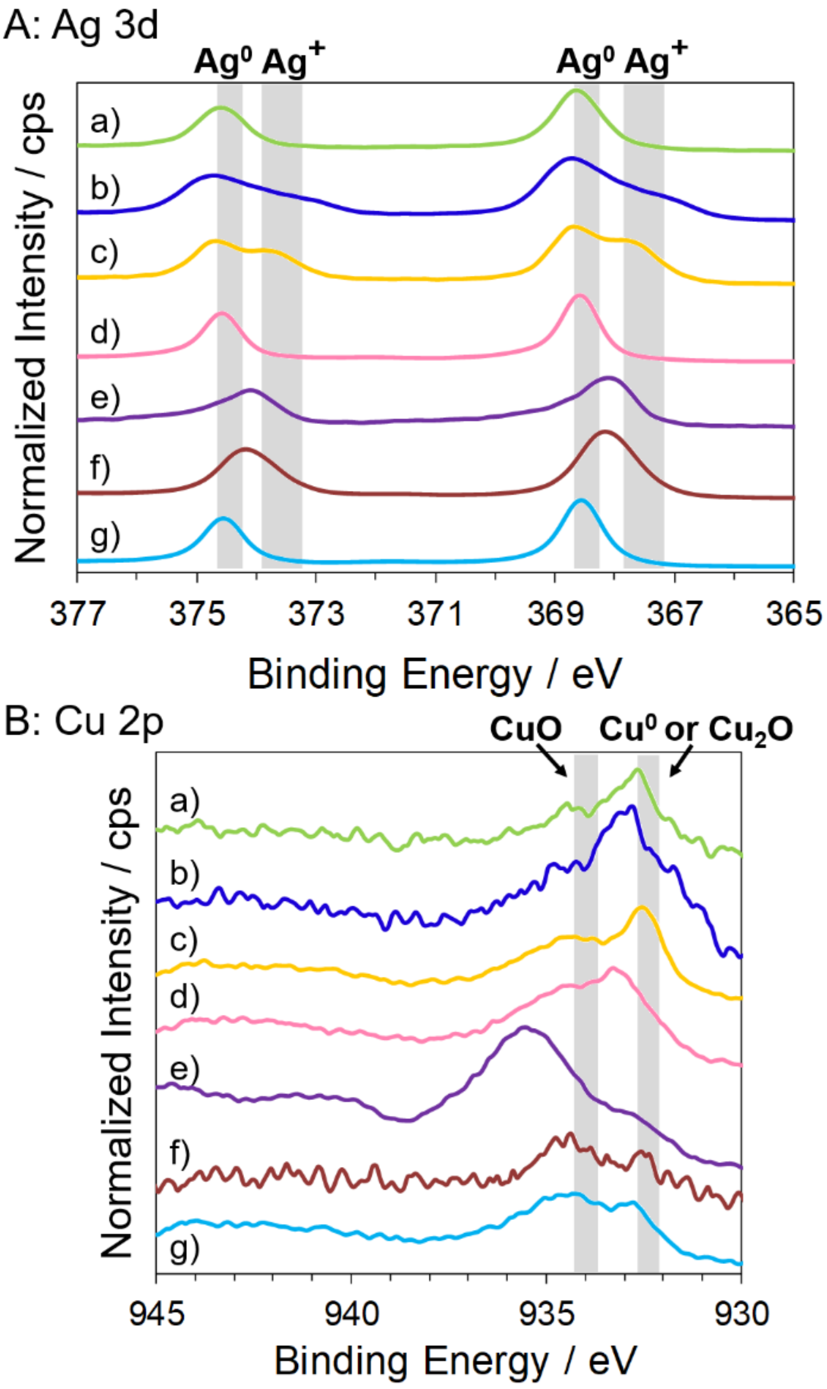

Figure 3-16. High resolution XPS spectra of (A) Ag 3d and (B) Cu 2p peaks obtained from (a) Cu@Ag NPs before the ligand exchange, and the precipitates of Cu@Ag NPs after the washing process using methanol in the (b) absence and presence of (c) 1.0 mM CTAC, (d) 29 mM HCl, (e) 100 mM oxalic acid + 1.0 mM CTAC, (f) 100 mM malonic acid + 1.0 mM CTAC, and (g) 100 mM hydrazine + 1.0 mM CTAC.

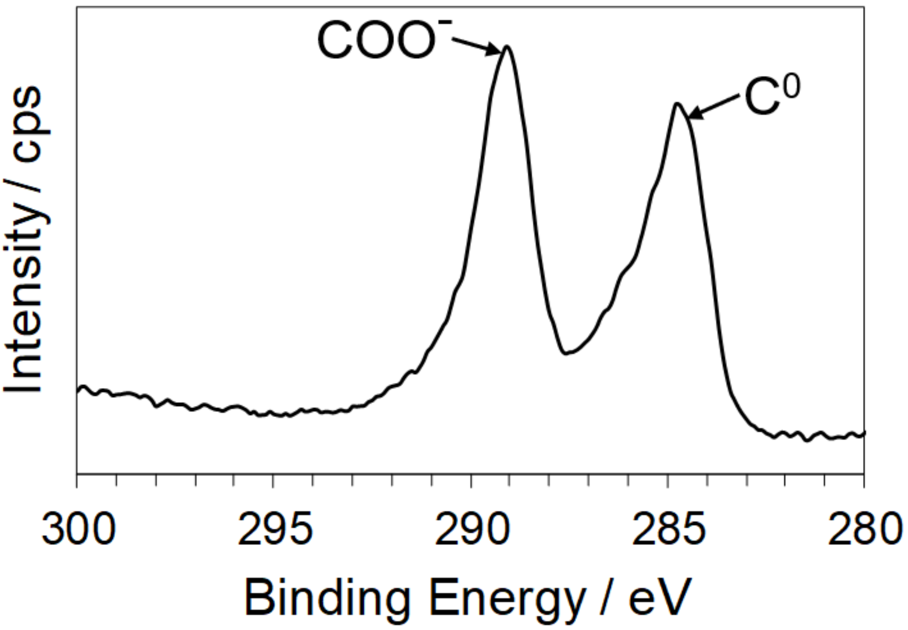

Figure 3-17. XPS spectrum of C 1s peaks obtained from the precipitate of Cu@Ag NPs after the washing process using the 100 mM oxalic acid + 1.0 mM CTAC methanol solution.

3-2-3 Effect of Acidity on Coalescence of Cu-Ag Core-Shell NPs

From the results in the section 3-2-2, the author hypothesized that the coalescence of Cu@Ag NPs was affected by the acidity in the methanol solution because the acidic methanol solution containing HCl, oxalic acid, or malonic acid strongly induced the coalescence of NPs. As TOPO is protonated under the acidic conditions, TOPO on the surface of Cu@Ag NP easily desorbed, which brings about the effective coalescence (Figure 3-18a). On the contrary, the basic methanol solution containing hydrazine suppressed the coalescence. To investigate the hypothesis, various amounts of NaOH were added to the 1.0 mM CTAC methanol solution. The PXRD patterns and the crystallite sizes of the precipitates of Cu@Ag NPs after the RT chemical sintering are shown in Figure 3-19 and Table 3-2, respectively. The addition of the low concentration of NaOH (≤ 3.9 mM) slightly increased the crystallite size. Under the basic conditions, it may be difficult for TOPO to desorb from Cu@Ag NP (Figure 3-18b) because TOPO is not protonated. On the other hand, the addition of the high concentration of NaOH (≥ 10 mM) significantly increased the crystallite size. When the high concentration of NaOH was added, it is probable that the hydroxide ion effectively worked as a sintering agent (Figure 3-18c) because the hydroxide ion has also been used as a sintering agent of Ag NPs [31]. The sharp peak originated from Cu_2O ($2\theta = 36°$) was observed in those cases [32-34]. Moreover, the main peak originated from Ag and Cu ($2\theta = 44°$) shifted and the peak became identical with that of bulk Ag. Namely, it means that most of Cu atoms were oxidized under the high concentration NaOH (≥ 10 mM). The slow desorption of TOPO under the basic conditions may allow Cu to be oxidized by oxygen in air before the coalescence.

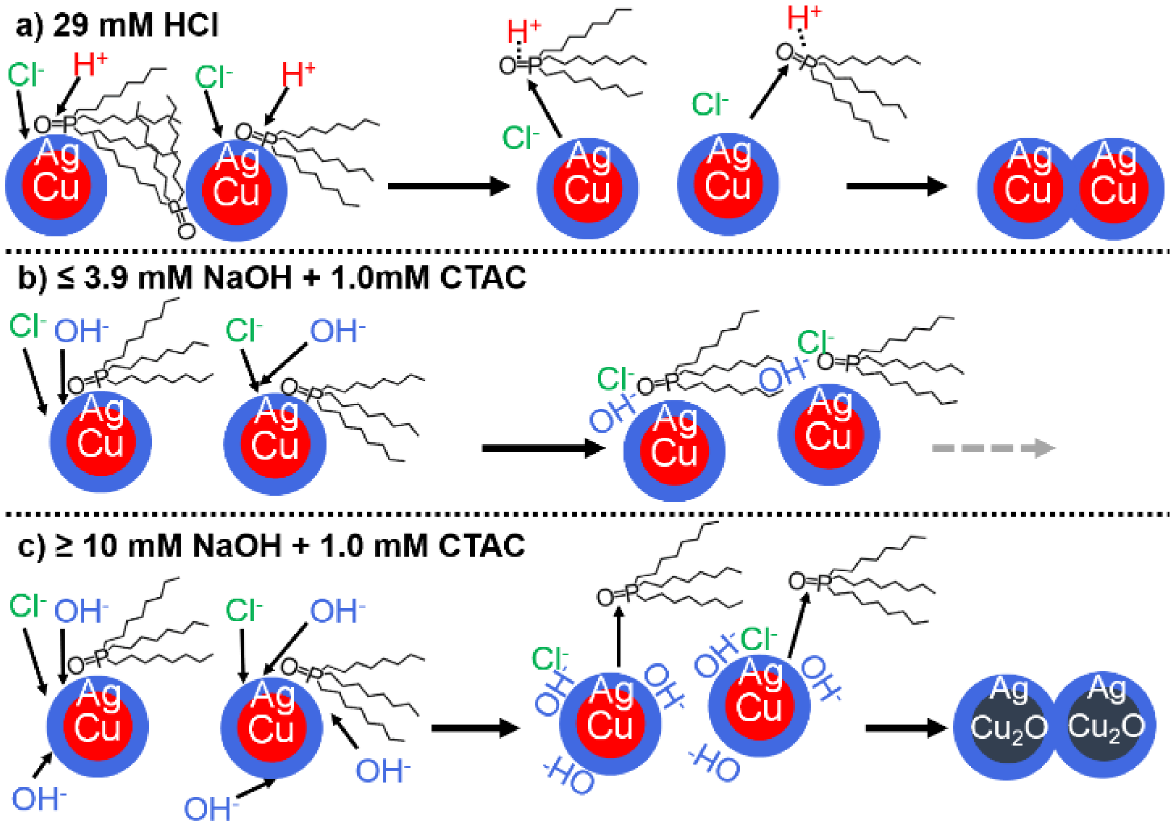

Figure 3-18. Plausible mechanism of coalescence of Cu@Ag NPs under various conditions.

Table 3-2. Crystallite sizes of the precipitates of Cu@Ag NPs at Ag (111) after the washing process using the 1.0 mM CTAC methanol solution and various concentrations of NaOH.

Added agents	Crystallite size ± standard error (nm)
Before ligand exchange	2.8 ± 0.1
1.0 mM CTAC	13.4 ± 0.1
0.39 mM NaOH + 1.0 mM CTAC	7.2 ± 0.1
1.0 mM NaOH + 1.0 mM CTAC	7.6 ± 0.2
3.9 mM NaOH + 1.0 mM CTAC	5.7 ± 0.1
10 mM NaOH + 1.0 mM CTAC	20.5 ± 0.6
100 mM NaOH + 1.0 mM CTAC	18.8 ± 0.2

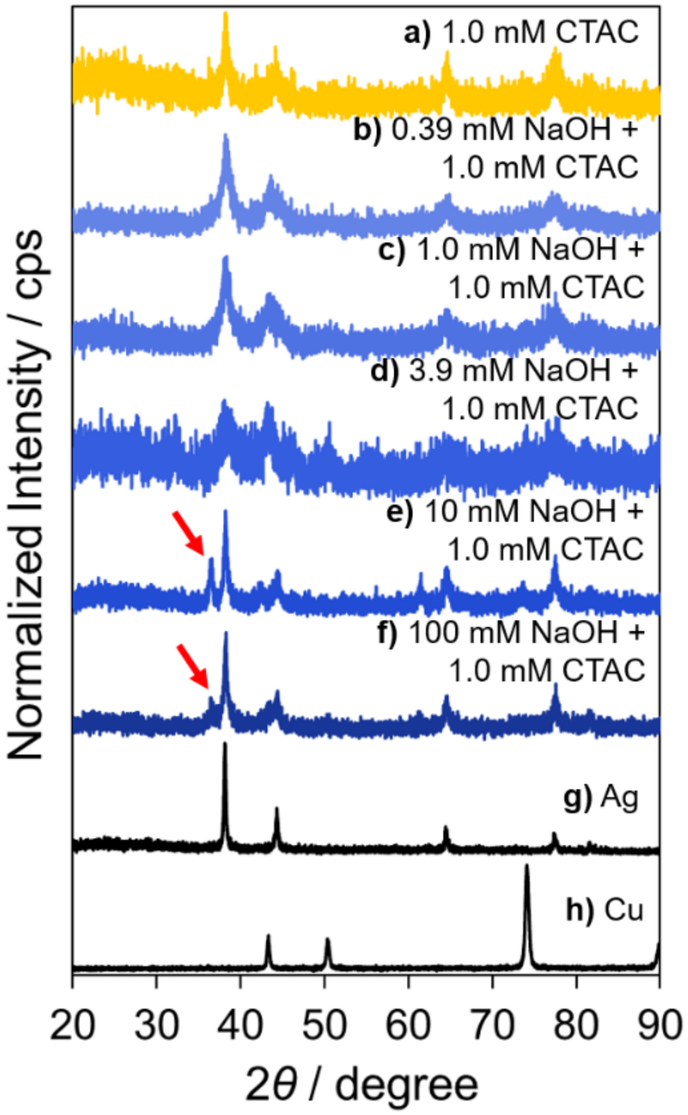

Figure 3-19. PXRD patterns of the precipitates of Cu@Ag NPs after the washing process using the 1.0 mM CTAC methanol solution and various concentrations of NaOH. [NaOH] = (a) 0 mM, (b) 0.39 mM, (c) 1.0 mM, (d) 3.9 mM, (e) 10 mM, and (f) 100 mM. Reference patterns of (g) bulk Ag and (h) bulk Cu. The red arrows show the peak originated from Cu_2O.

3-2-4 Characterization of Cu/Ag Thin Film Prepared by RT Chemical Sintering

The TOPO paste of Cu@Ag NPs can be used as a NP ink because Cu@Ag NPs stably disperse in a nonpolar solvent. After the Cu@Ag NP ink was cast onto the PET substrate, the RT chemical sintering was carried out by dipping the substrate into methanol containing a sintering agent and/or a reducing agent for 30 min under air atmosphere (Figure 3-20). The various methanol solutions containing a sintering agent and/or a reducing agent were examined here. Only in the case of 29 mM HCl a conductive thin film was obtained (Table 3-3). The optical image of the Cu/Ag thin film is shown in Figure 3-21. The electrical resistivity of the obtained Cu/Ag thin film was $(5.1 \pm 1.7) \times 10^{-5}$ Ω m, which is comparable to that [$(1.2 \pm 0.5) \times 10^{-5}$ Ω m] of the Ag thin film reported in the section 2-2-5. From the corresponding SEM images, it was shown that most of the Cu@Ag NPs coalesced and that organic compounds were removed (Figures 3-22c and 3-22d). In addition, the cross sectional SEM image of this thin film revealed that the coalescence of Cu@Ag NPs proceeded up to 1 μm depth at least (Figure 3-23). However, many cracks were observed. Thus, the resistivity of this thin film was higher than that of bulk Ag and Cu. In other cases, electrical resistivity was too high to be measured. The high electrical resistivity was attributed to the many cracks and organic compounds that existed in the film. While the coalescence of Cu@Ag NPs and removal of organic compounds were attained by the addition of 1.0 mM CTAC, 100 mM malonic acid + 1.0 mM CTAC, and 50 mM NaOH + 60 mM hydrazine (Figures 3-22b, 3-22h, and 3-22j), many cracks generated in the film because of the relatively-slow coalescence (Figures 3-22a, 3-22g, and 3-22i). Strong acid such as HCl was necessary for the preparation of the conductive thin film. In the case of oxalic acid, organic compounds mostly remained (Figures 3-22e and 3-22f). This fact induced the high electrical resistivity. The existence of organic compounds was also confirmed by TGA (Figure 3-15).

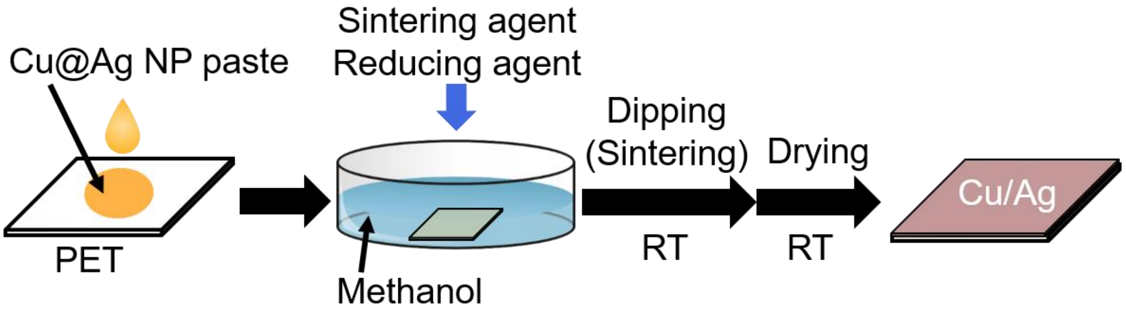

Figure 3-20. Preparation of a Cu/Ag conductive thin film by the RT chemical sintering of Cu@Ag NPs through dipping into methanol containing a sintering agent and/or a reducing agent.

Table 3-3. Electrical resistivity of Cu/Ag thin films prepared from Cu@Ag NPs by dipping into methanol containing a sintering agent and/or a reducing agent for 30 min at RT.

Added agents	Electrical resistivity (Ω m)
1.0 mM CTAC	No conductivity
29 mM HCl	$(5.1 \pm 1.7) \times 10^{-5}$
100 mM oxalic acid + 1.0 mM CTAC	No conductivity
100 mM malonic acid + 1.0 mM CTAC	No conductivity
60 mM hydrazine + 50 mM NaOH	No conductivity

Figure 3-21. Optical image of the brown Cu/Ag thin film obtained by dipping Cu@Ag NPs into the 29 mM HCl methanol solution for 30 min at RT.

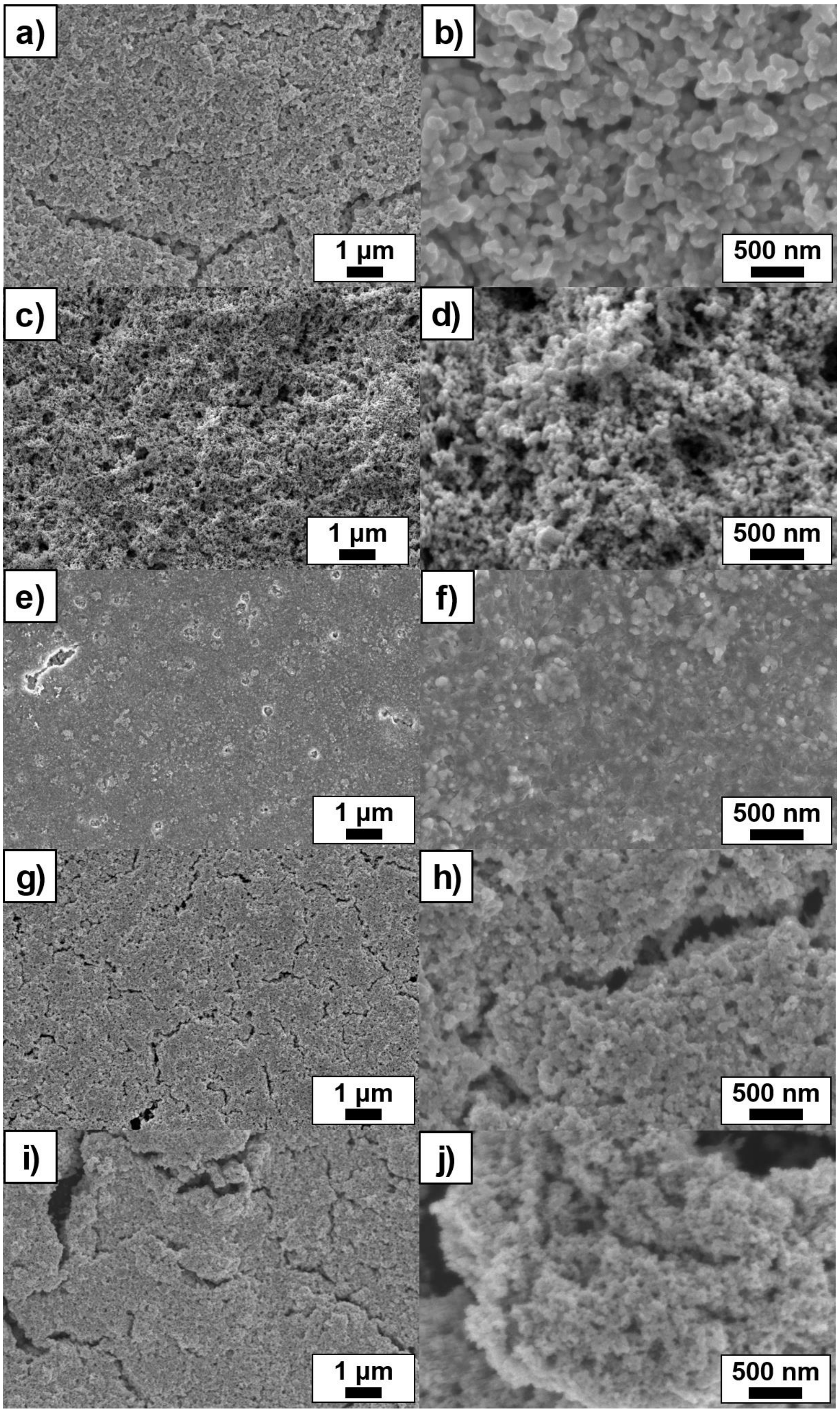

Figure 3-22. SEM images of Cu/Ag thin films prepared from Cu@Ag NPs by dipping into the (a, b) 1.0 mM CTAC, (c, d) 29 mM HCl, (e, f) 100 mM oxalic acid + 1.0 mM CTAC, (g, h) 100 mM malonic acid + 1.0 mM CTAC, and (i, j) 50 mM NaOH + 60 mM hydrazine methanol solutions.

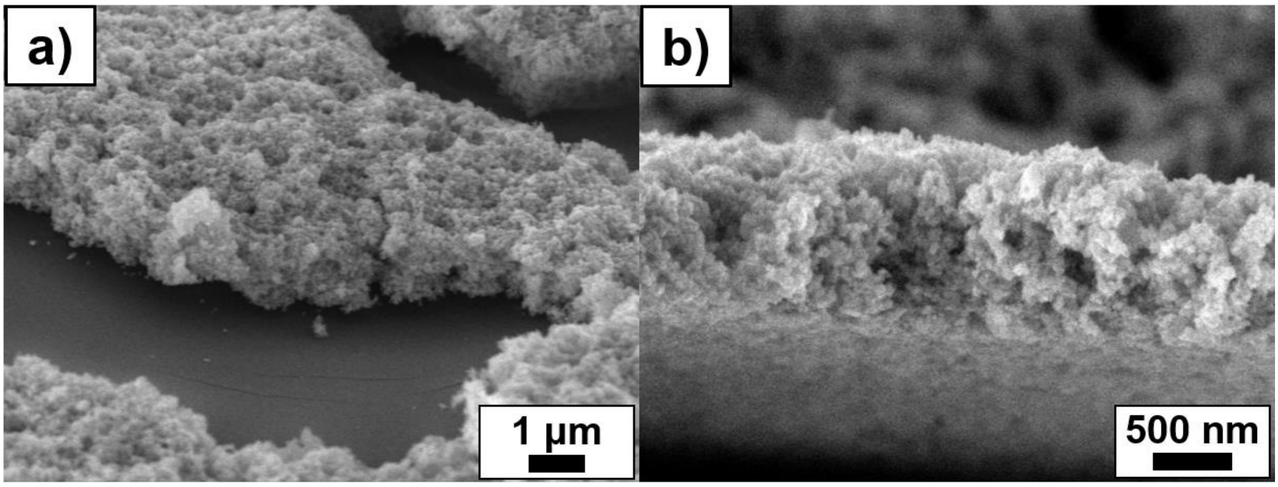

Figure 3-23. Cross sectional SEM images of the Cu/Ag thin film prepared from Cu@Ag NPs by dipping into the 29 mM HCl methanol solution observed at (a) 10,000-fold and (b) 30,000-fold magnification.

To confirm the necessity of the ligand exchange to TOPO, oleylamine/oleic-acid-capped Cu@Ag NPs were also used as nanoink. The obtained Cu/Ag thin film was not conductive even after dipping into the 29 mM HCl methanol solution for 30 min at RT. As oleylamine oleic acid are less soluble in methanol, it may be difficult for them to desorb from Cu@Ag NPs in methanol. This phenomenon was also observed in the section 2-2-4. Moreover, it was observed by SEM measurements that some cracks were generated in the Cu/Ag thin film (Figure 3-24). Thus, TOPO is more suitable than oleylamine and oleic acid in the RT chemical sintering of Cu@Ag NPs.

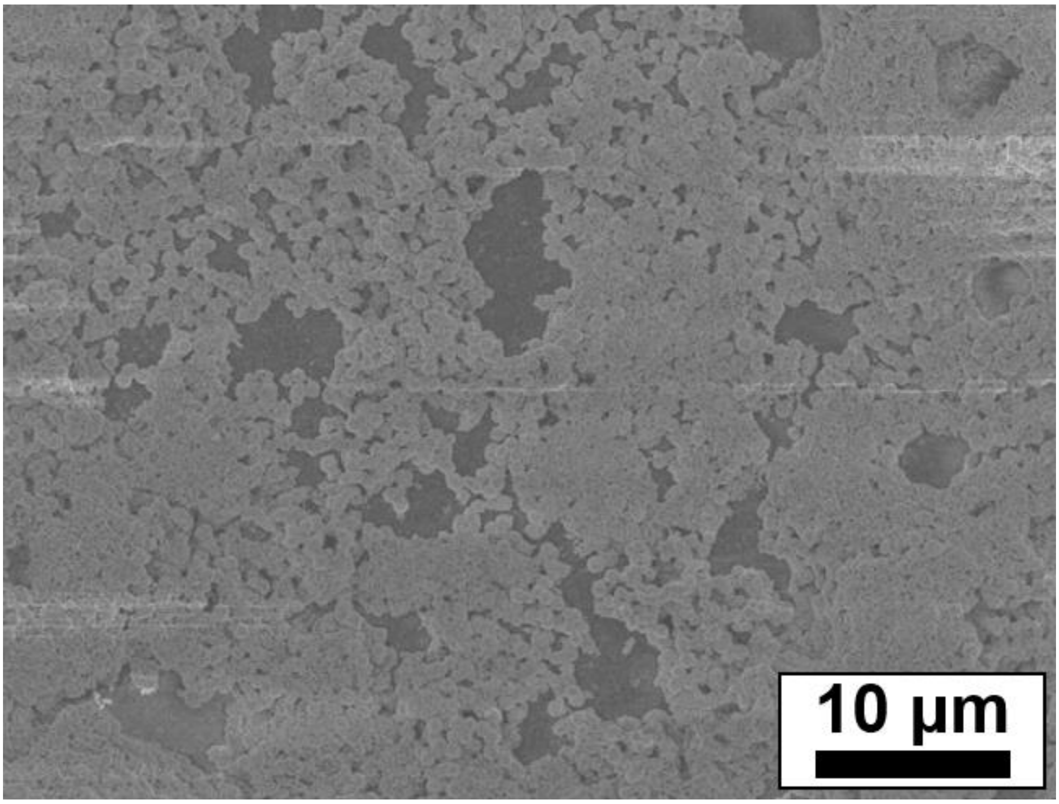

Figure 3-24. SEM image of the Cu/Ag thin film prepared from oleylamine/oleic-acid-capped Cu@Ag NPs by dipping into the 29 mM HCl methanol solution.

To confirm the elemental composition of the Cu/Ag thin film prepared using the 29 mM HCl methanol solution, PXRD measurement was carried out. The PXRD patterns of the Cu/Ag thin film were a simple mixture of PET [35], Ag, and Cu peaks (Figure 3-25). Table 3-4 shows the crystallite sizes at Ag (111) and Cu (111). While the crystallite size of Ag increased compared with that of Cu@Ag NPs before the ligand exchange, that of Cu mostly remained unchanged. This result indicates that the coalescence of Cu@Ag NPs occurred only on the Ag shell.

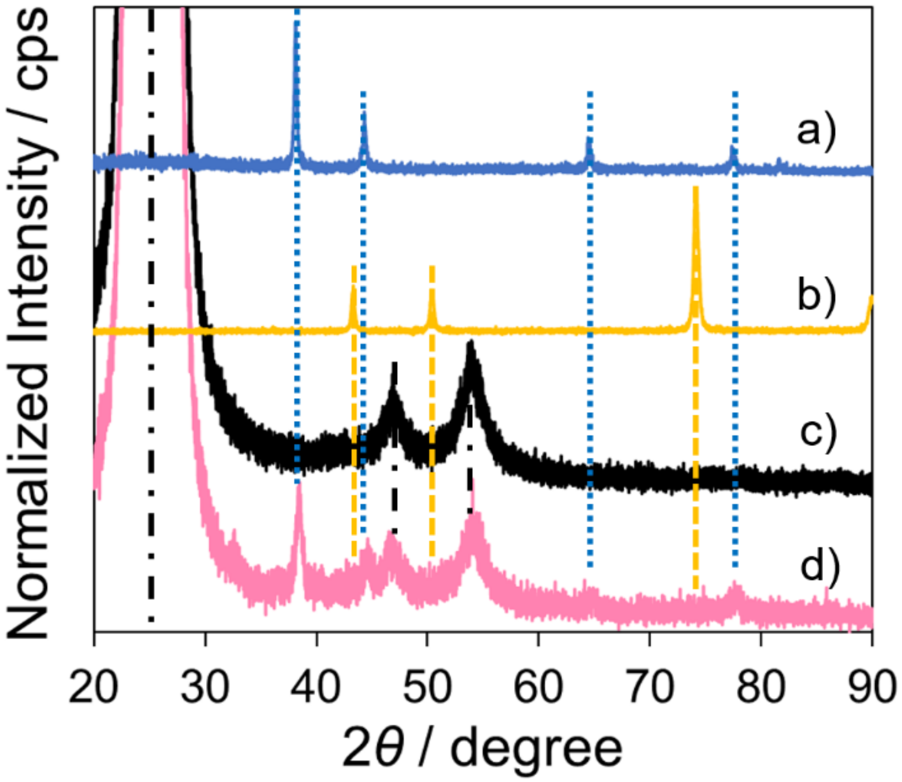

Figure 3-25. PXRD patterns of (a) bulk Ag, (b) bulk Cu, (c) PET substrate and (d) Cu/Ag thin film prepared using the 29 mM HCl methanol solution on the PET substrate.

Table 3-4. Crystallite sizes of Cu/Ag thin film prepared using the 29 mM HCl methanol solution at Ag (111) and Cu (111).

	Crystallite size ± standard error (nm)	
	Ag (111)	Cu (111)
Before ligand exchange	2.8 ± 0.1	8.6 ± 0.1
After dipping into 29 mM HCl methanol solution	15.1 ± 0.4	8.3 ± 0.2

Section 3-3: Summary

The ligand exchange from oleylamine/oleic acid to TOPO was carried out on the surface of Cu@Ag NPs and the NPs were sintered at RT with methanol containing a sintering agent and/or a reducing agent. In the case of 29 mM HCl, the crystallite size significantly increased. In addition, Ag and Cu were hardly oxidized during the process. Under strong acidic conditions, protonated TOPO rapidly desorbed from Cu@Ag NP, which brought about the effective coalescence with slight oxidation. On the basis of these results, a Cu/Ag thin film was prepared from TOPO-capped Cu@Ag NPs by dipping into methanol containing 29 mM HCl. The electrical resistivity of the obtained thin film was $(5.1 \pm 1.7) \times 10^{-5}\ \Omega$ m. The RT coalescence of Cu@Ag NPs with slight oxidation was successfully achieved under mild conditions in this study. The author expects this method to be widely applicable to the fabrication of electrodes on flexible substrates by RT chemical sintering of core-shell metal NPs.

Section 3-4: Experiments

3-4-1 Materials

All the chemicals and solvents were obtained commercially and used without further purification. Cu(II) acetylacetonate and sodium hydroxide (NaOH) was purchased from Kishida Chemical Co., Ltd. Tri-*n*-octylphosphine oxide (TOPO) was purchased from Aldrich. Silver nitrate, cetyltrimethylammonium chloride (CTAC), oleylamine, oleic acid, oxalic acid, hydrazine monohydrate, and malonic acid were purchased from Wako Pure Chemical Industries, Ltd. Hydrogen chloride methanol solution (6.6 w/w%) was purchased from Tokyo Chemical Industries Co., Ltd. Oleic-acid-capped Ag NPs (Kishu-Giken Co., Ltd., Wakayama, Japan), which were synthesized by the improved vacuum evaporation on running oil substrate (VEROS) method [36-38], were used for the fabrication of Ag NP ink. The average diameter of oleic-acid-capped Ag NPs used here was 7.1 ± 1.7 nm (Figure 3-26).

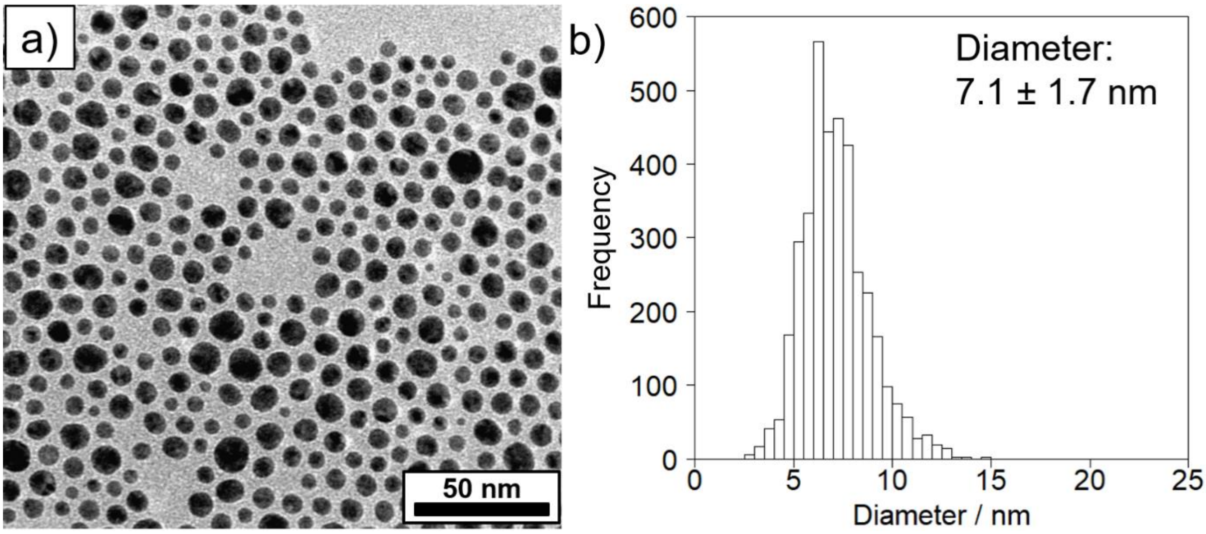

Figure 3-26. (a) TEM image and (b) particle size distribution of oleic-acid-capped Ag NPs.

3-4-2 Synthesis of Cu-Ag Core-Shell NPs

The synthesis of Cu@Ag NPs was carried out based on the method reported by Muzikansky *et al* [16]. First, Cu NPs were synthesized by the thermal decomposition method. Next, Cu@Ag NPs were synthesized by the galvanic replacement method. Typically, Cu(II) acetylacetonate (2.1 g) was added to 100 mL of oleylamine at RT (about 25 °C). The solution was stirred at 100 °C for 2 h under N_2 bubbling. Then, this solution was heated at 220 °C for 3 h under Ar atmosphere. After the reaction, the solution was cooled to RT. The oleylamine-capped Cu NPs were collected by centrifugation of the reaction solution at 15 000 rpm for 50 min, and the supernatant was removed. Then, oleylamine-capped Cu NPs were dispersed in about 2 mL of *n*-hexane. Silver nitrate (1.4 g, Cu:Ag = 1:1 mol/mol) was dissolved in 10 mL of oleylamine. The silver nitrate oleylamine solution (10 mL) and oleic acid (10 mL) were added to the dispersion of Cu NPs. The mixture was stirred at RT for 20 h under Ar atmosphere. After the reaction, about 60 mL of methanol was added as an antisolvent to the dispersion of Cu@Ag NPs (about 20 mL). The dispersion was then centrifuged at 15 000 rpm for 10 min. After the removal of the supernatant, about 20 mL of methanol was added to the residue again. The centrifugation was then carried out at 5000 rpm for 10 min. The same procedure was repeated two times. The obtained oleylamine/oleic-acid-capped Cu@Ag NPs (1.4 g) were dried in air.

3-4-3 Ligand Exchange of Cu-Ag Core-Shell Nanopaticles and Subsequent Washing Process

The ligand exchange from oleylamine/oleic acid to TOPO and subsequent washing process of Cu@Ag NPs were carried out in accordance with that shown in Chapter 2. First, oleylamine/oleic-acid-capped Cu@Ag NPs (50 mg) were dispersed in 90 mL of *n*-heptane at a concentration of 0.56 g L^{-1}. Next, the *n*-heptane solution of TOPO (0.13 M, 10 mL) was added to the dispersion of Cu@Ag NPs. The concentrations after mixing were adjusted to 0.50 g L^{-1} of Cu@Ag NP and 1.3×10^{-2} M TOPO, respectively. The mixture was stirred at 40 °C for an hour. Then, *n*-heptane was removed by a rotary evaporator to increase the NP concentration in the paste. In this step, centrifugation is not suitable because once sedimented NPs do not redisperse in the solvent. The concentrated TOPO dispersion of Cu@Ag NPs was used without purification as the paste (metal / TOPO = 37 / 500 w/w%) in the preparation of Cu/Ag films (see following paragraph). Although the paste contains oleylamine and oleic acid as impurities, the amount (about 13 mg) is very small compared with that (500 mg) of TOPO. Therefore, the effect of impurities would be negligible.

In addition, the paste was also used to investigate the coalescence of Cu@Ag NPs as a model experiment for the actual RT chemical sintering. The methanol solution containing a sintering agent and/or a reducing agent was added to the paste. The combinations of sintering agent and/or reducing agent used here were 1.0 mM CTAC, 29 mM HCl, 1.0 mM CTAC + 100 mM oxalic acid, 1.0 mM CTAC + 100 mM malonic acid, and 1.0 mM CTAC + 100 mM hydrazine. Methanol was used as a solvent in all the cases. The volume ratio of the solvent containing metal NPs to the methanol solution was set to more than five. The dispersion was then centrifuged at 4000 rpm for 10 min. After the removal of the supernatant, the methanol solution was again added to the residue under an ultrasonication. The centrifugation was carried out at 4000 rpm for 10 min. The RT chemical sintering in the model experiment was completed at this stage. Then, pure methanol was added to the residue under an ultrasonication to remove a sintering agent and/or a reducing agent. The precipitate was collected by centrifugation at 4000 rpm for 10 min, and the supernatant solution was removed. The obtained precipitate was dried in air and evaluated by TEM, FE-SEM, XRD, and XPS.

3-4-4 Preparation of Cu/Ag Conductive Thin Films

The pastes for the fabrication of Cu/Ag films were prepared as mentioned in the section 3-4-3. Poly(ethylene terephthalate) (PET) substrates (Toray, Lumirror S10 250 μm) were washed with acetone and methanol before use. Several drops of the fabricated paste were cast onto the PET substrate (20 mm × 10 mm). This substrate was dipped in 20 mL of methanol containing a sintering agent and/or a reducing agent at RT (about 25 °C) for 30 min in air (Figure 3-20). The combinations of sintering agent and/or reducing agent used here were 1.0 mM CTAC, 29 mM HCl, 1.0 mM CTAC + 100 mM oxalic acid, 1.0 mM CTAC + 100 mM malonic acid, and 50 mM NaOH + 60 mM hydrazine. Methanol was used as a solvent in all the cases. After the RT chemical sintering, the obtained Cu/Ag thin films (thickness: ~5 μm) were rinsed with pure methanol and dried in air for 30 min at RT before measurements such as electrical resistivity.

3-4-5 Characterization

TEM images were taken at 100 kV with a JEM-2100 (JEOL, Japan) for the observation of synthesized metal NPs. The diameter of NPs was evaluated by ImaegJ software. The morphology of Cu/Ag thin films was characterized by FE-SEM (JSM-6700F and JSM-7800F, JEOL, Japan). Electrical resistivity was measured using a four-probe method (MCP-T370, Mitsubishi Chemical Analytech Co., Ltd., Japan). The thickness of Cu/Ag thin films was measured by laser microscopy (OLS4100, OLYMPUS, Japan). Electrical resistivity was evaluated to multiply sheet resistance by thickness. The absorption spectra were recorded by a UV-Vis spectrophotometer V-730 (JASCO, Japan) at RT. The as-prepared samples after the ligand exchange were diluted with *n*-hexane for measurements of absorption spectra. TGA was carried out by a ThermoMass Photo (Rigaku, Japan). TICs for analysis of ligands adsorbed on Cu@Ag NPs were obtained from a GC-MS spectrometer, QP2010 Plus (Shimadzu, Japan). Here, Ultra ALLOY UA5-30M-0.25F (Frontier Laboratories Ltd., Japan) was used as a column. The samples for GC-MS were heated by a PY-3030D pyrolizer (Frontier Laboratories Ltd., Japan) at 300˚C before injection. FT-IR was performed using a FT-IR 4100 (JASCO, Japan) coupled with an ATR instrument having a Ge crystal. XRD patterns were recorded using a MiniFlexII (Rigaku, Japan, Cu Kα radiation) equipped with a Kα filter operating at 30 kV and 15 mA. The crystallite size was calculated by the Scherrer's equation: $D = 0.9\lambda/\beta\cos\theta$, where D is the crystallite size, λ is the wavelength of X-ray, β is the FWHM of diffraction peak, and θ is the diffraction angle. XPS measurements were carried out by a KRATOS AXIS Ultra DLD X-ray photoelectron spectrometer (Shimadzu, Japan). XRF measurement was carried out by an EA6000VX (Hitachi, Japan).

Reference

[1] Ma, S.; Liu, L.; Bromberg, V; Singler, T. J. Electroless copper plating of inkjet-printed polydopamine nanoparticles: a facile method to fabricate highly conductive patterns at near room temperature. *ACS Appl. Mater. Interfaces.* **2014**, *6*, 19494–19498.

[2] Tamai, T.; Watanabe, M.; Kobayashi, Y.; Nakahara, Y.; Yajima, Surface modification of PEN and PET substrates by plasma treatment and layer-by-layer assembly of polyelectrolyte multilayer thin films and their application in electroless deposition. *RSC Adv.* **2017**, *7*, 33155–33161.

[3] Knapp, C. E.; Chemin, J.-B.; Douglas, S. P.; Ondo, D. A.; Guillot, J.; Choquet, P.; Boscher, N. D. Room-temperature plasma-assisted inkjet printing of highly conductive silver on paper. *Adv. Mater. Technol.* **2018**, *3*, 1700326.

[4] Kawasaki, H.; Tomotoshi, D. Surface and interface designs in copper-based conductive inks for printed/flexible electronics. *Nanomaterials* **2020**, *10*, 1689.

[5] Kamyshny, A.; Magdassi, S. Conductive nanomaterials for printed electronics. *Small* **2014**, *10*, 3515–3535.

[6] Yamamoto, M.; Kakiuchi, H.; Kashiwagi, Y.; Yoshida, Y.; Ohno, T.; Nakamoto, M. Synthesis of Ag-Pd alloy nanoparticles suitable as precursors for ionic migration-resistant conductive film. *Bull. Chem. Soc. Jpn.* **2010**, *83*, 1386–1391.

[7] Zhang, Y.; Zhu, P.; Li, Gang; Zhao, T.; Fu, X.; Sun, R.; Zhou, F.; Wong, C.-P. Facile preparation of monodisperse, impurity-free, and antioxidation copper nanoparticles on a large scale for application in conductive ink. *ACS Appl. Mater. Interfaces.* **2014**, *6*, 560–567.

[8] Yang, H.-J.; He, S.-Y.; Chen, H.-L.; Tuan, H.-Y. Monodisperse copper nanocubes: synthesis, self-assembly, and large-area dense-packed films. *Chem. Mater.* **2014**, *26*, 1785–1793.

[9] Liu, J.; Chen, H.; Ji, H.; Li, M. Highly Conductive Cu–Cu joint formation by low-temperature sintering of formic acid-treated Cu nanoparticles. *ACS Appl. Mater. Interfaces.* **2016**, *8*, 33289–33298.

[10] Yokoyama, S.; Motomiya, K.; Takahashi, H.; Tohji, K. Green synthesis of Cu micro/nanoparticles for low-

resistivity Cu thin films using ascorbic acid in aqueous solution. *J. Mater. Chem. C* **2016**, *4*, 7494–7500.

[11] Kamikoriyama, Y.; Imamura, H.; Muramatsu, A.; Kanie, K. Ambient aqueous-phase synthesis of copper nanoparticles and nanopastes with low-temperature sintering and ultra-high bonding abilities. *Sci. Rep.* **2019**, *9*, 899.

[12] Lee, C.; Kim, N. R.; Koo, J.; Lee, Y. J.; Lee, H. M. Cu-Ag core-shell nanoparticles with enhanced oxidation stability for printed electronics. *Nanotechnology* **2015**, *26*, 455601.

[13] Tian, Y.; Jiang, Z.; Wang, C.; Ding, S.; Wen, J.; Liu, Z.; Wang, C. Sintering mechanism of the Cu–Ag core–shell nanoparticle paste at low temperature in ambient air. *RSC Adv.* **2016**, *6*, 91783–91790.

[14] Yu, X.; Li, J.; Shi, T.; Cheng, C.; Liao, G.; Fan, J.; Li, T.; Tang, Z. A green approach of synthesizing of Cu-Ag core-shell nanoparticles and their sintering behavior for printed electronics. *J. Alloys Compd.* **2017**, *724*, 365–372.

[15] Dai, X.; Xu, W.; Zhang, T.; Shi, H.; Wang, T. Room temperature sintering of Cu-Ag core-shell nanoparticles conductive inks for printed electronics. *Chem. Eng. J.* **2019**, *364*, 310–319.

[16] Muzikansky, A.; Nanikashvili, P.; Grinblat, J.; Zitoun, D. Ag dewetting in Cu@Ag monodisperse core–shell nanoparticles. *J. Phys. Chem. C* **2013**, *117*, 3093–3100.

[17] José-Yacamán, M.; Gutierrez-Wing, C.; Miki, M.; Yang, D.-Q.; Piyakis, K. N.; Sacher, E. Surface diffusion and coalescence of mobile metal nanoparticles. *J. Phys. Chem. B* **2005**, *109*, 9703–9711.

[18] Wang, J.; Shin, S.; Hu, A. Geometrical effects on sintering dynamics of Cu–Ag core–shell nanoparticles *J. Phys. Chem. C* **2016**, *120*, 17791–17800.

[19] Magdassi, S.; Grouchko, M.; Berezin, O.; Kamyshny, A. Triggering the sintering of silver nanoparticles at room temperature. *ACS Nano* **2010**, *4*, 1943–1948.

[20] Grouchko, M.; Kamyshny, A.; Mihailescu, C. F.; Anghel, D. F.; Magdassi, S. Conductive inks with a "Built-In" mechanism that enables sintering at room temperature. *ACS Nano* **2011**, *5*, 3354–3359.

[21] Shi, L.; Layani, M.; Cai, X.; Zhao, H.; Magdassi, S.; Lan, M. An inkjet printed Ag electrode fabricated on

plastic substrate with a chemical sintering approach for the electrochemical sensing of hydrogen peroxide. *Sensors and Actuators B* **2018**, *256*, 938–945.

[22] Peng, P.; Li, L.; Guo, W.; Hui, Z.; Fu, J.; Jin, C; Liu, Y.; Zhu, Y. Room-temperature joining of silver nanoparticles using potassium chloride solution for flexible electrode application. *J. Phys. Chem. C* **2018**, *122*, 2704–2711.

[23] Yamamoto, M.; Kashiwagi, Y.; Nakamoto, M. Size-controlled synthesis of monodispersed silver nanoparticles capped by long-chain alkyl carboxylates from silver carboxylate and tertiary amine. *Langmuir* **2006**, *22*, 8581–8586.

[24] Lamprecht, E.; Watkins, G. M.; Brown, M. E. The thermal decomposition of copper(II) oxalate revisited *Thermochim. Acta* **2006**, *446*, 91–100.

[25] Gao, X.-Y.; Wang, S.-Y.; Li, J.; Zheng, Y.-X.; Zhang, R.-J.; Zhou, P.; Yang, Y.-M.; Chen, L.-Y. Study of structure and optical properties of silver oxide films by ellipsometry, XRD and XPS methods. *Thin solid Films* **2004**, *455–456*, 438–442.

[26] Wang, P.; Huang, B.; Zhang, X.; Qin, X.; Dai, Y.; Wang, Z.; Lou, Z. Highly efficient visible light plasmonic photocatalysts Ag@Ag(Cl, Br) and Ag@AgCl-AgI. *ChemCatChem* **2011**, *3*, 360–364.

[27] Hokita, Y.; Kanzaki, M.; Sugiyama, T.; Arakawa, R.; Kawasaki, H. High-concentration synthesis of sub-10-nm copper nanoparticles for application to conductive nanoinks. *ACS Appl. Mater. Interfaces.* **2015**, *7*, 19382–19389.

[28] Ghodselahi, T.; Vesaghi, M. A.; Shafiekhani, A.; Baghizadeh, A.; Lameii, M. XPS study of the Cu@Cu_2O core-shell nanoparticles. *Appl. Surf. Sci.* **2008**, *255*, 2730–2734.

[29] Faraggi, M. N.; Rogero, C.; Arnau, A.; Trelka, M.; Écija, D.; Isvoranu, C.; Schnadt, J.; Marti-Gastaldo, C.; Coronado, E.; Gallego, J. M.; Otero, R.; Miranda, R. Role of deprotonation and Cu adatom migration in determining the reaction pathways of oxalic acid adsorption on Cu(111). *J. Phys. Chem. C* **2011**, *115*, 21177–21182.

[30] Frost, D. C.; Ishitani, A.; McDowell, C. A. X-ray photoelectron spectroscopy of copper compounds. *Mol. Phys.* **1972**, *24*, 861–877.

[31] Xiao, Y.; Zhang, Z. H.; Yang, M.; Yang, H. F.; Li, M. Y.; Cao, Y. The effect of NaOH on room-temperature sintering of Ag nanoparticles for high-performance flexible electronic application. *Materials Letters* **2018**, *222*, 16–20.

[32] Wang, B.-Y.; Yoo, T.-H.; Song, Y.-W.; Lim, D.-S.; Oh, Y.-J. Cu ion ink for a flexible substrate and highly conductive patterning by intensive pulsed light sintering. *ACS Appl. Mater. Interfaces.* **2013**, *5*, 4113–4119.

[33] Dharmadasa, R.; Jha, M.; Amos, D. A.; Druffel, T. Room temperature synthesis of a copper ink for the intense pulsed light sintering of conductive copper films. *ACS Appl. Mater. Interfaces.* **2013**, *5*, 13227–13234.

[34] Kanzaki, M.; Kawaguchi, Y.; Kawasaki, H. Fabrication of conductive copper films on flexible polymer substrates by low-temperature sintering of composite Cu ink in air. *ACS Appl. Mater. Interfaces.* **2017**, *9*, 20852–20858.

[35] Nissen, K. E.; Stevens, M. G.; Stuart, B. H.; Baker, A. T. Characterization of PET films modified by tetraethylenepentamine (TTEPA). *J. Polym. Sci., Part B: Polym. Phy.* **2001**, *39*, 623–633.

[36] Ienaga, T.; Okada, S.; Nakahara, Y.; Watanabe, M.; Tamai, T.; Yajima, S.; Kimura, K. Comparison of physical adsorption strength of protective agents via ligand exchange of silver NPs prepared by vacuum evaporation on running oil substrate. *Bull. Chem. Soc. Jpn.* **2017**, *90*, 1251–1258.

[37] Ienaga, T.; Nakahara, Y.; Kimura, K. Synthesis and characterization of silver nanoparticles by vacuum evaporation on running hydrocarbon solution containing nonionic surfactant in cylindrical glass chamber. *Chem. Lett.* **2014**, *43*, 1893–1895.

[38] Ienaga, T.; Nakahara, Y.; Yajima, S.; Kimura, K. Effect of protective agents on silver nanoparticle preparation by vacuum evaporation on running hydrocarbon solution. *J. Nanosci. Nanotechnol.* **2018**, *18*, 2547–2554.

Chapter 4: Fabrication of Porous Pd Structures by RT Chemical Sintering of Pd NPs and Their Catalytic Activities

Section 4-1: Introduction

Pd is one of the most important and widely used metals in organic syntheses [1], purification of automotive exhaust gases [2], and fuel cell technology [3]. For example, Pd salts and Pd complexes, such as Pd(II) acetate and tetrakis(triphenylphosphine)palladium(0), are used as a homogeneous catalyst [4,5]. Homogeneous catalysts have potential problems such as difficult separation and recovery of catalysts from the reaction medium. In recent years, Pd nanoparticle (Pd NP) has also been used as such a catalyst due to its large surface area and excellent solvent dispersibility [1,6-12]. However, Pd NPs tend to aggregate upon heating, which leads to serious decline in their catalytic abilities. To prevent Pd NPs from the aggregation in the reaction, Pd NPs are normally covered with organic ligands. The ligands limit the reaction solvent where Pd NPs can disperse. The Pd NPs-catalyzed reaction takes place less efficiently in the unfavorable solvents due to the aggregation of NPs and the inhibition by ligands. The functional groups of ligands interact with the Pd NP surface and can potentially alter the bonding modes of the adsorbents, thereby affecting the catalytic activity [13].

These days, porous metal structures (PMSs) have been reported as catalytic metals such as Ag [14,15], Ni [16,17], Au [18,19], Pt [20,21], Pd [22,23], and their alloy metals (e.g. Cu-Ag [24], Pd-Au [25], and Pd-Ni [26]). In contrast to traditional porous materials such as silica and carbon, they possess intrinsic catalytic properties depending on the type of metal. Especially, nanoporous/mesoporous metals have been used as heterogeneous catalysts due to their extremely-large surface area and easy separation. Many types of PMSs have been fabricated by electrochemical methods [27]. This type of method typically involves four main steps: (1) formation of a sacrificial template on the substrate and electrode; (2) filling of pores with target metal precursors; (3) reduction of the precursors by reducing agent and electrochemical reduction; (4) selective removal of the template [27]. However, only conductive electrodes (e.g. carbon) can be used as a substrate in this method. Also, PMSs are fabricated by electrochemical dealloying of the base metal in alloy [27]. For example, Tanaka *et al.* has fabricated PMS of $Pd_{67}Ni_{23}P_{10}$ from a glassy metallic alloy of $Pd_{30}Ni_{50}P_{20}$ [28]. Although the selective dealloying requires a large amount of energy, it is difficult to obtain pure PMSs by this method.

The RT chemical sintering method of metal nanoparticles with TOPO can be conducted without heating, as shown in Chapters 2 and 3. In this method, only sintering agents are added to desorb organic ligands easily from metal NPs. This brings about the coalescence of metal NPs at RT. At that time, many voids were generated by the simple outflow of TOPO in the metal thin film. This event motivated the author to fabricate porous Pd structures by the RT chemical sintering. Although the conventional methods for the fabrication of porous metal structures using a sacrificial template produce a lot of waste containing metal ion and chemicals for removing the template, the amount of waste could be suppressed in the RT chemical sintering of NPs because the template can be removed easily during the sintering in this method. Therefore, the RT chemical sintering could be a new candidate for the fabrication of porous metal structures in environmental-friendly processes.

In Chapters 2 and 3, the author reported that TOPO-capped Ag NPs and Cu@Ag NPs were effectively coalesced by centrifugation with methanol. The RT chemical sintering of TOPO-capped Ag NPs and Cu@Ag NPs was carried out by dipping into methanol containing chloride ions. The obtained metal thin films showed higher resistivity than that of bulk metal due to many voids generated during the sintering. In this chapter, the author created a new strategy for the fabrication of porous Pd structure by the RT chemical sintering of Pd NPs with sacrificial templates and sintering agents. The outline of the strategy is shown in Figure 4-1. First, oleylamine-capped Pd NPs were mixed with TOPO as a sacrificial template to prepare the Pd NP paste. Then, porous Pd structures were fabricated at RT from Pd NPs by dipping into methanol containing a sintering agent. Since TOPO easily dissolves in methanol, the coalescence of Pd NPs proceeds even at RT with the aid of a sintering agent. Here, various sintering agents such as KOH, CTAC and HCl were examined. As porous Pd structures are expected to be heterogeneous catalysts, the Suzuki coupling reaction, which is a well-known Pd-catalyzed reaction [29-32], was performed for the evaluation of the catalytic abilities.

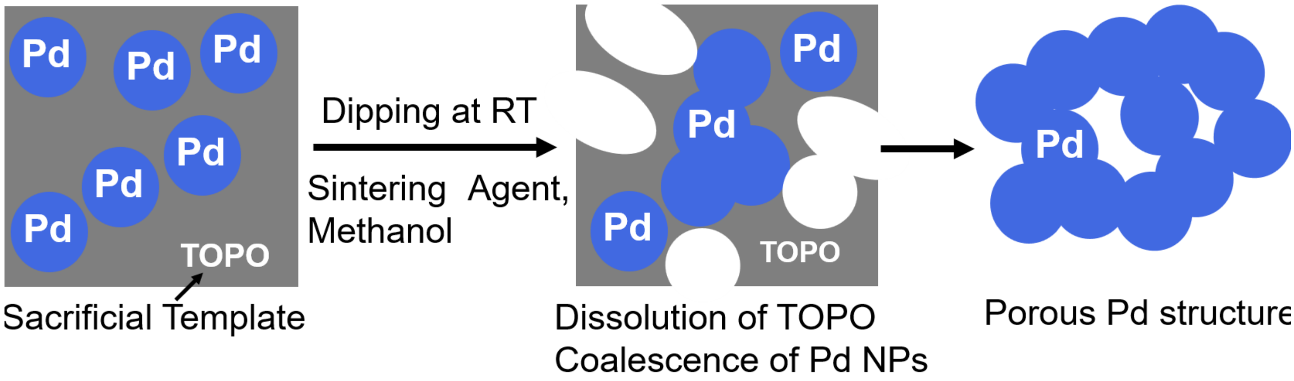

Figure 4-1. RT chemical sintering of TOPO paste of Pd NPs by dipping into methanol containing a sintering agent.

Section 4-2: Results and Discussion

4-2-1 Pd NPs ink

The synthesis of oleylamine-capped Pd NPs was conducted based on the method reported by Mazumber *et al*. [33]. Regarding the obtained Pd NPs, TEM observation was performed (Figure 4-2). From the analysis of TEM images, the average diameter of Pd NPs was determined to be 5.6 ± 0.6 nm (Figure 4-2b). This result clearly indicates that Pd NPs did not coalesce at all before the sintering process for the fabrication of porous Pd structures.

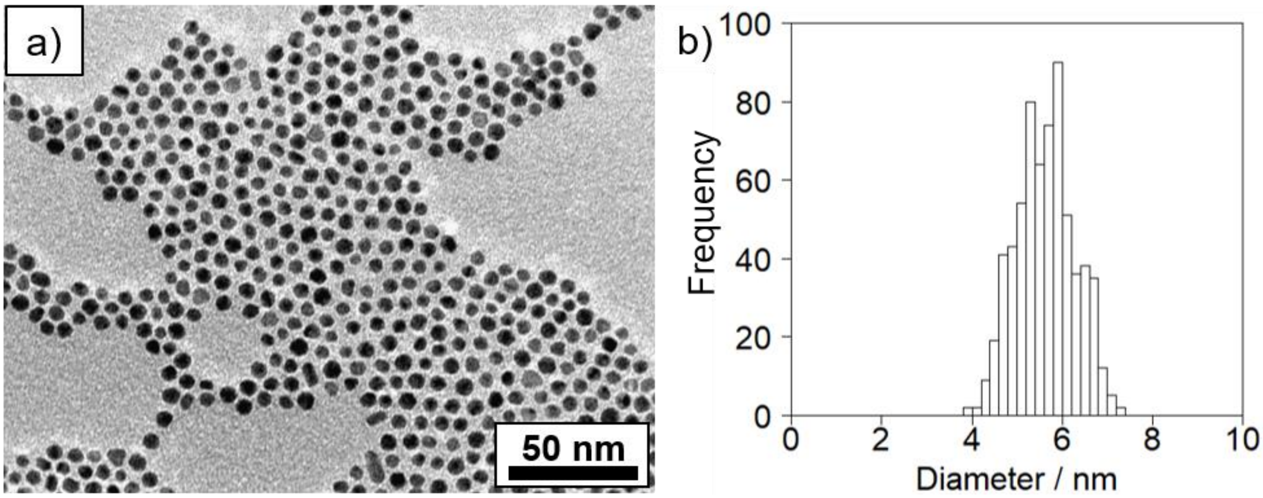

Figure 4-2. (a) TEM image and (b) particle size distribution of oleylamine-capped Pd NPs.

Pd NP pastes were prepared by mixing of oleylamine-capped Pd NP and a sacrificial template (TOPO, 1-dodecanol, and *n*-octadecane). The sacrificial templates used in this study are shown in Figure 4-3. The melting points of all the sacrificial templates selected here are around 40 °C. The surface ligand of Pd NPs was characterized by pyrolysis gas chromatograph mass spectroscopy (GC-MS) measurements after the RT chemical sintering with the 10 mM KOH methanol solution. Figure 4-4 shows total ion chromatograms (TICs) of the sacrificial templates and Pd NPs before and after the RT chemical sintering. While the peak of oleylamine was detected in the case of Pd NPs before and after mixing the template, the peaks of the sacrificial template were scarcely detected in these cases. This result indicates that the ligand exchange from oleylamine to the sacrificial template hardly proceeded on the surface of Pd NPs and that the sacrificial templates were easily removed by washing with the 10 mM KOH methanol solution.

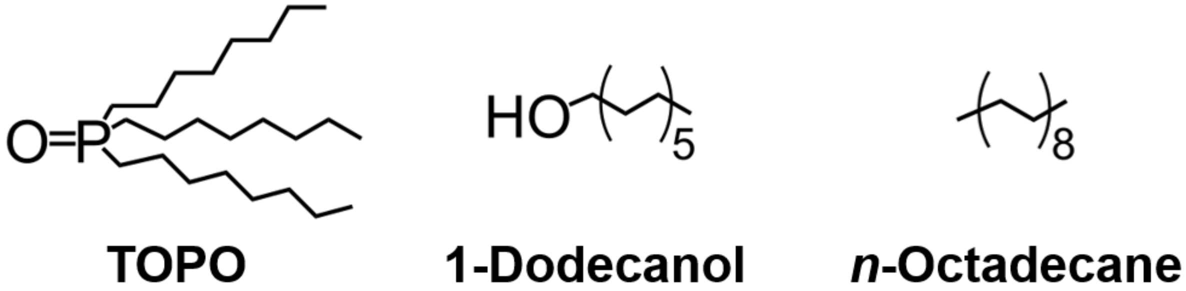

Figure 4-3. Sacrificial templates used in this study.

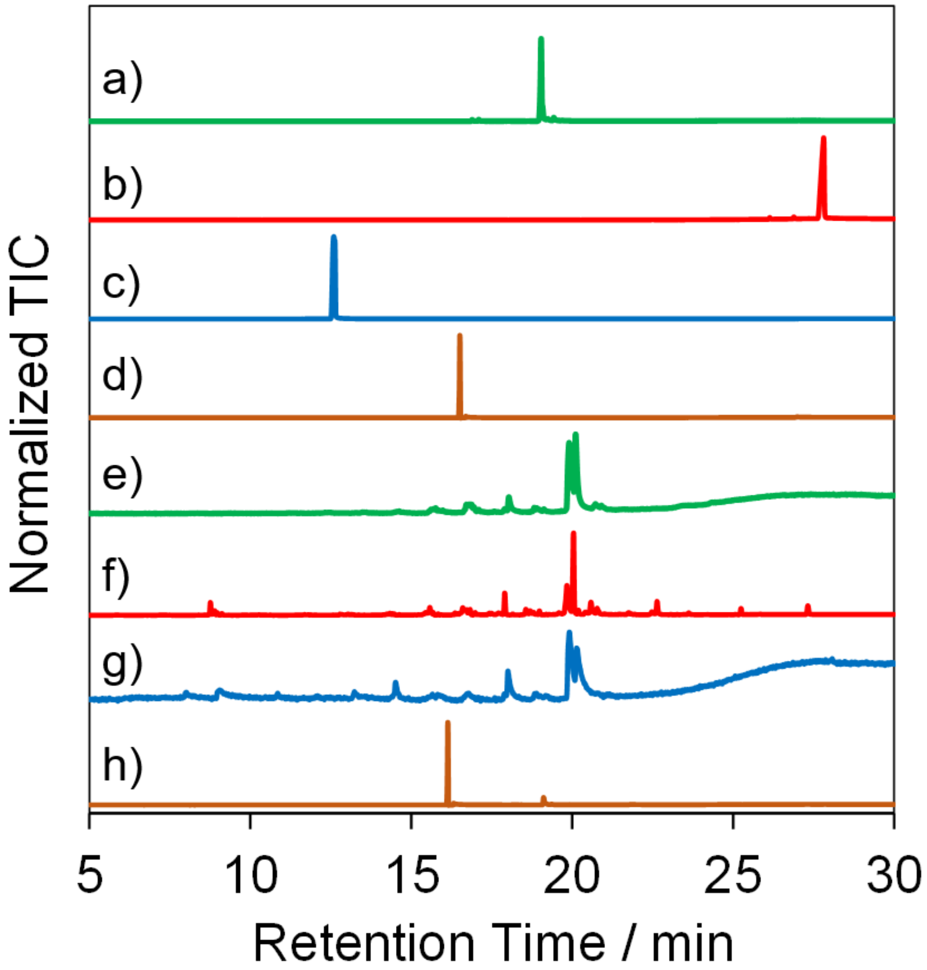

Figure 4-4. TICs of (a) oleylamine, (b) TOPO, (c) 1-dodecanol, (d) *n*-octadecane, (e) oleylamine-capped Pd NPs, and Pd NPs mixed with (f) TOPO, (g) 1-dodecanol, (h) *n*-octadecane after washing with the 10 mM KOH methanol solution.

4-2-2 Effect of Sintering Agents and Sacrifice Templates on Sintering of Pd NPs

At first, KOH was used as the sintering agent. KOH is often used for the activation of Pd catalysts and it is easily soluble in methanol. The Pd NP paste containing a sacrificial template was cast on the glass substrate and it was sintered at RT by dipping into the 10 mM KOH methanol solution for 30 min. In order to obtain Pd porous structures by the RT chemical sintering, Pd NPs should be dispersed in the sacrificial template and then coalesce each other via removing the templates by the dissolution in methanol. In the case of the TOPO paste, organic residues were mostly removed and NPs were hardly observed after the RT chemical sintering, as shown in SEM and TEM images (Figure 4-5a and 4-5b). On the other hand, NPs hardly coalesced in the case of the 1-dodecanol paste (Figure 4-5c and 4-5d) because they aggregated in 1-dodecanol. In the case of the n-octadecane paste, organic residues covered NPs and inhibited their coalescence (Figure 4-5e and 4-5f). Although Pd NPs dispersed in *n*-octadecane, *n*-octadecane was hardly removed by methanol due to its low solubility. These results demonstrate that in this RT chemical sintering, the miscibility of the sacrificial template with Pd NPs and methanol plays an important role and that TOPO is the best sacrificial template for the formation of porous Pd structures in methanol.

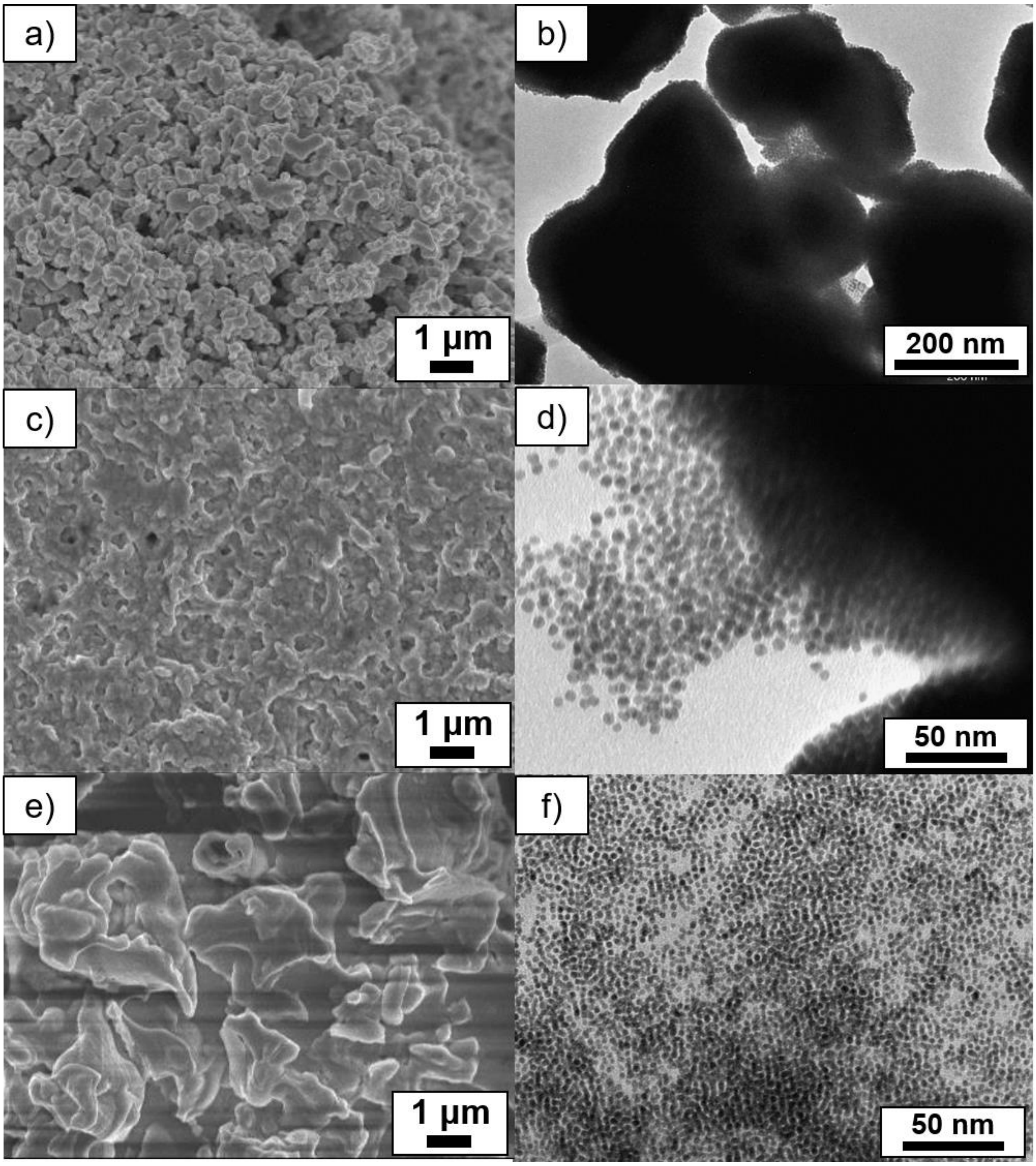

Figure 4-5. SEM and TEM images of Pd structures prepared using (a), (b) TOPO, (c), (d) 1-dodecanol, and (e), (f) *n*-octadecane by dipping into the 10 mM KOH methanol solution for 30 min.

Next, the effect of the KOH concentration on the RT chemical sintering was investigated using the TOPO paste of Pd NPs. According to the SEM images (Figure 4-6), the increase of the KOH concentration promoted the coalescence of Pd NPs. The amounts of organic compounds in the Pd structures were evaluated by TGA (Figure 4-7). Heating was performed under a helium atmosphere at a rate of 10 °C min^{-1} in the temperature range from 30 to 500 °C. In the case of methanol only, the weight loss decreased compared with that of oleylamine-capped Pd NPs. This assumes the loss of ligands on the particle surface. The increase of the KOH concentration contributed to the increase of maximum weight losses at around 350 °C. This result indicates that the Pd methoxide and Pd-OH generated with the aid of KOH [1,34]. In the case of 50 mM KOH, the weight loss decreased compared with that in the case of 10 mM KOH. Since the surface area of the Pd structure became smaller due to their coalescence, the amount of Pd methoxide and Pd-OH on the surface of Pd decreased. Namely, the optimized KOH concentration is required for the activation of porous Pd structures. The weight increase was observed at over 350 °C. This phenomenon may be originated from partial oxidation of Pd by residual oxygen [34].

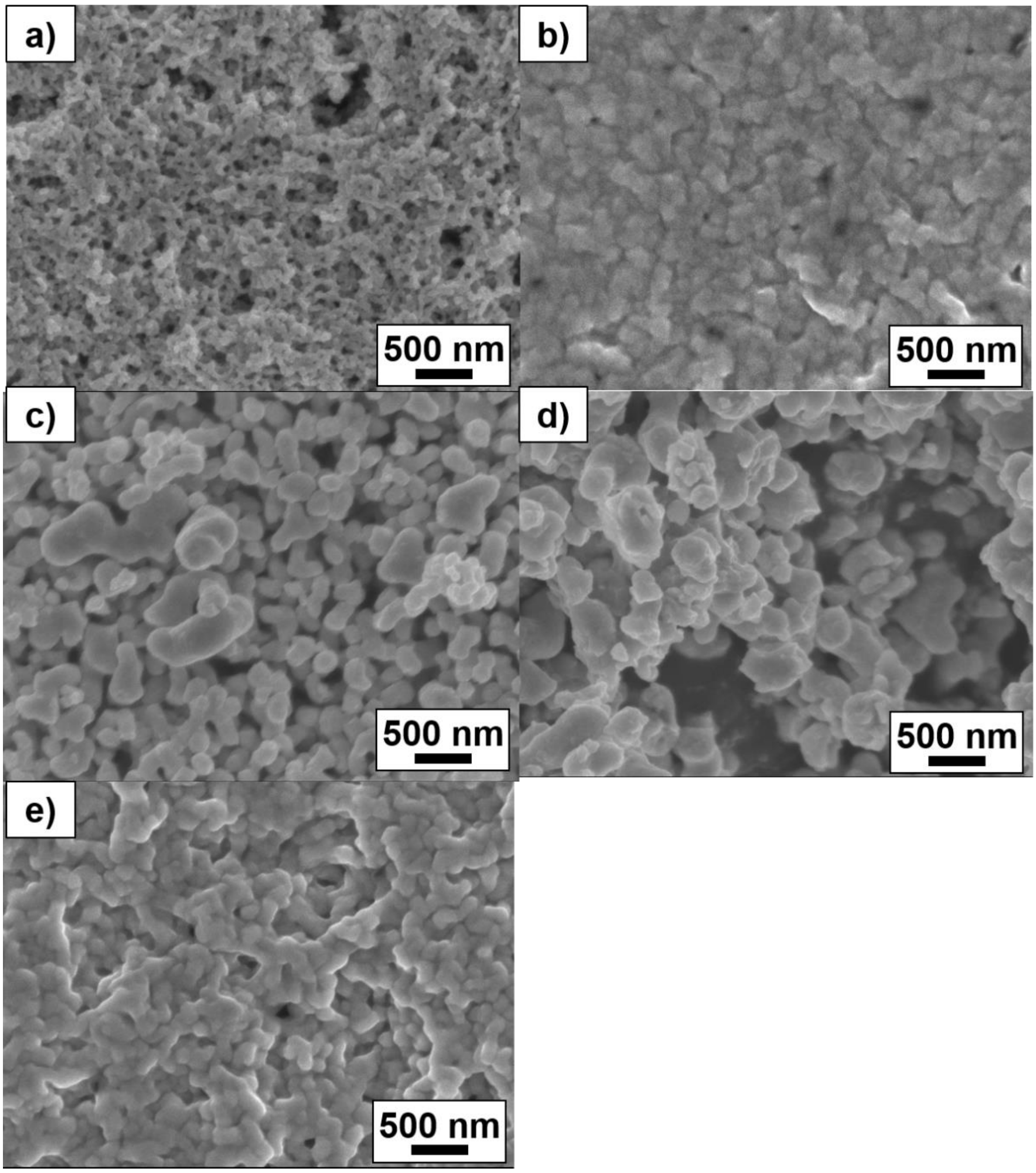

Figure 4-6. SEM images of Pd structures prepared from the TOPO paste of Pd NPs by dipping into methanol (a) without and with (b) 0.10 mM, (c) 1.0 mM, (d) 10 mM, and (e) 50 mM KOH.

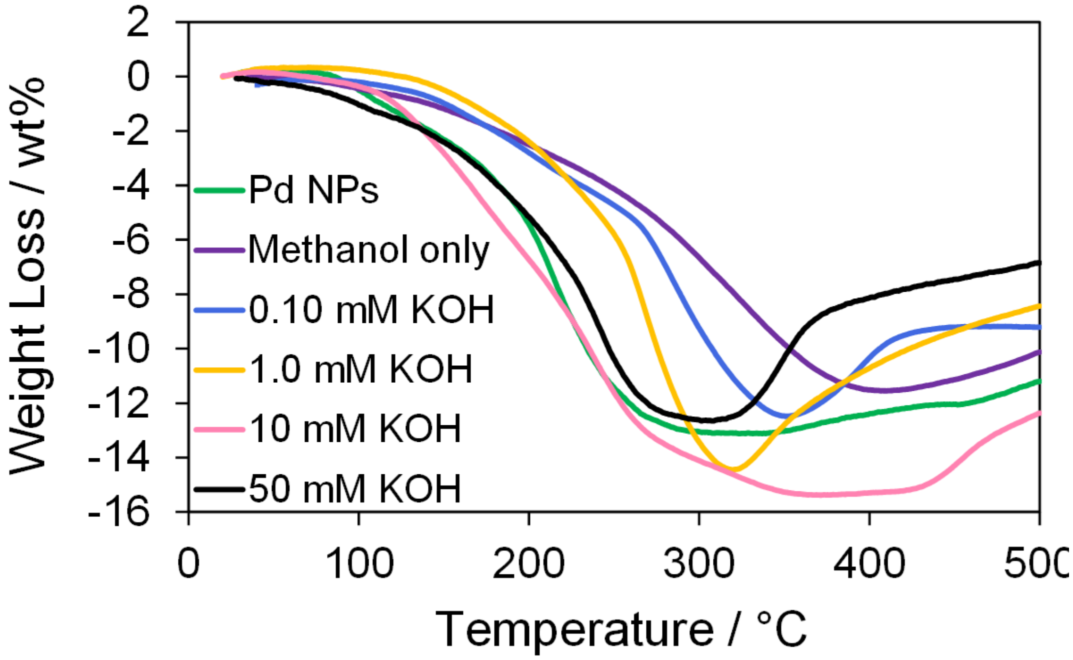

Figure 4-7. TGA curves of oleylamine-capped Pd NPs (before the RT chemical sintering) and Pd structures prepared from the TOPO paste of Pd NPs by dipping into methanol without and with 0.10 mM, 1.0 mM, 10 mM, and 50 mM KOH in a helium atmosphere.

Other types of sintering agents, which are 1.0 mM CTAC and 29 mM HCl, were also examined using the TOPO paste of Pd NPs. The concentrations of sintering agents were set according to our previous study. In the case of HCl, organic residues were completely removed and the coalescence of Pd NPs was clearly observed (Figure 4-8a). In the case of CTAC, however, organic residues were observed in almost all of the area (Figure 4-8b). From these results, the coalescence of Pd NPs was affected by the acidity in the methanol solution. As TOPO is protonated under the acidic conditions, TOPO in the Pd NP paste is easily removed, which brings about the effective coalescence. Under the neutral conditions (CTAC), it may be difficult for TOPO to remove from the Pd NP paste because TOPO is not protonated. To confirm the point, the amounts of organic compounds in the Pd NPs after the RT chemical sintering were evaluated by TGA (Figure 4-9). When HCl was added into methanol, the weight loss decreased compared with those after the RT sintering with the 10 mM KOH and 1.0 mM CTAC methanol solutions.

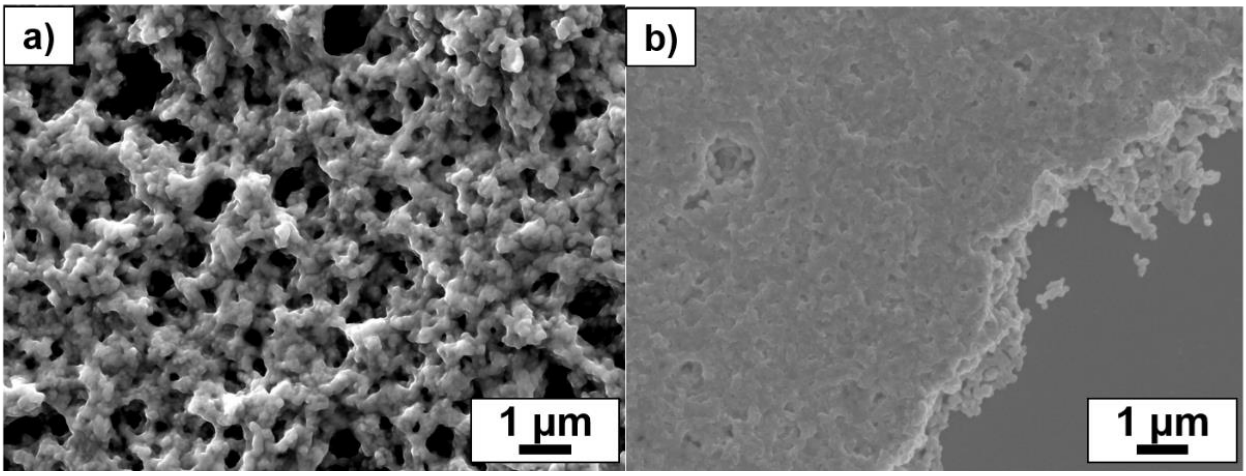

Figure 4-8. SEM images of Pd structures prepared from the TOPO paste of Pd NPs by dipping into methanol with (a) 29 mM HCl and (b) 1.0 mM CTAC.

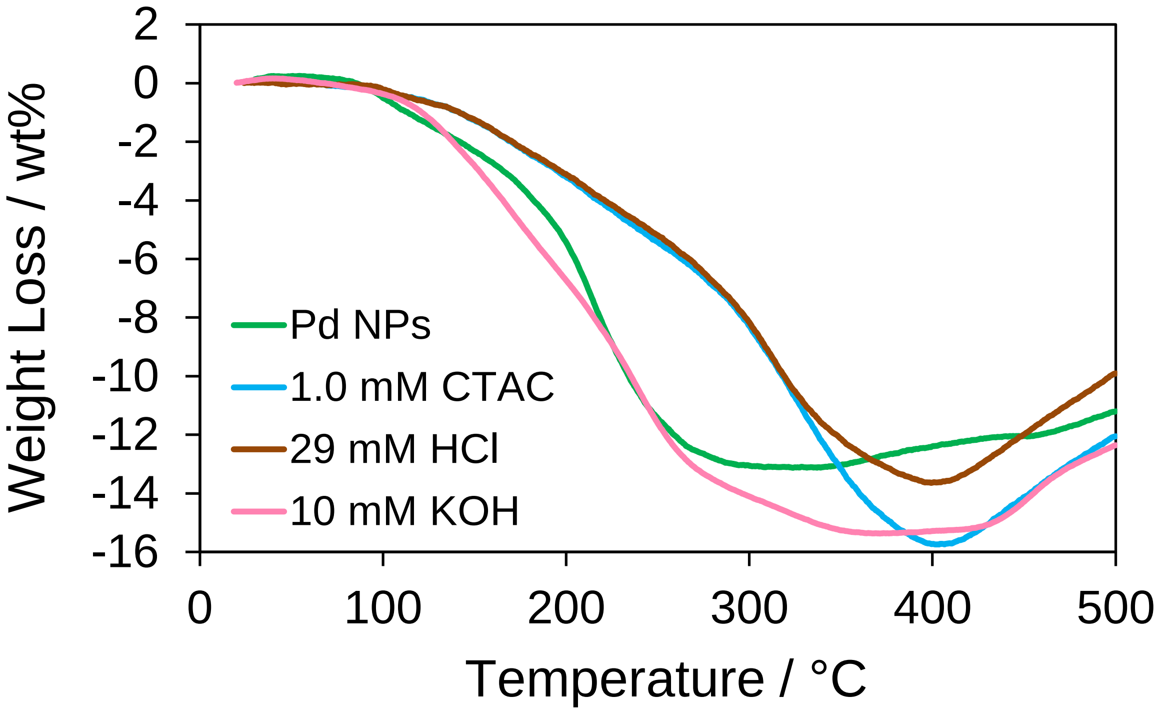

Figure 4-9. TGA curves of Pd structures prepared from the TOPO paste of Pd NPs by dipping into methanol with 29 mM HCl and 1.0 mM CTAC. in a helium atmosphere.

The elemental composition of Pd structures prepared by the RT chemical sintering was analyzed by XPS. The peaks at 335.3 eV and 340.5 eV were identified as Pd $3d_{5/2}$ and Pd $3d_{3/2}$ in Pd(0), respectively (Figure 4-10). On the other hand, the peaks at 336.9 eV and 342.3 eV were identified as Pd $3d_{5/2}$ and Pd $3d_{3/2}$ in Pd(II), respectively [36,37]. In all cases, the peaks of Pd(0) and Pd(II) were observed. The molar ratio of Pd(0)/Pd(II) was determined based on the respective area of two peaks (Table 4-1). In the cases of KOH, the ratio of Pd(II) was larger than that in other cases. Namely, the addition of KOH induced the oxidation of Pd. This result also supports that the Pd methoxide and Pd-OH generated on the surface of Pd.

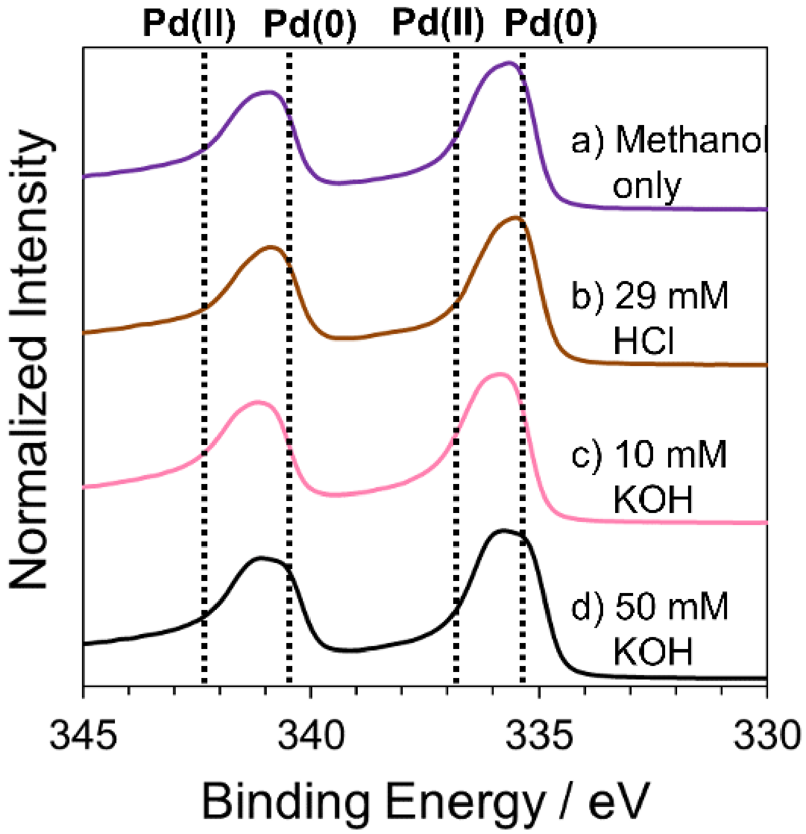

Figure 4-10 High resolution XPS spectra of Pd structures prepared from the TOPO paste of Pd NPs by dipping into methanol a) in the absence and the presence of b) 29 mM HCl, c) 10 mM KOH, and d) 50 mM KOH.

Table 4-1 The molar ratio of Pd(0) and Pd(II) in Pd structures determined by XPS.

Sintering agents	Pd(0) (mol%)	Pd(II) (mol%)
No addition (methanol only)	48	52
29 mM HCl	47	53
10 mM KOH	39	61
50 mM KOH	32	68

The crystallite sizes of porous Pd structures were evaluated by XRD (Figure 4-11). In all cases, the diffraction peaks at 2θ = 40°, 47° and 68° were identified as the (111), (200) and (220) planes of face-centered cubic Pd, respectively [38]. The crystallite sizes were calculated based on the Scherrer equation using FWHM of the diffraction peaks at Pd (111). The calculated values of crystallite sizes are summarized in Table 4-2. In all cases (methanol only, CTAC, HCl and KOH), the crystallite size of porous Pd structures mostly remained compared with that of oleylamine-capped Pd NPs. These results indicate that the crystal reconstruction and growth in the neck hardly occurred in the sintering process.

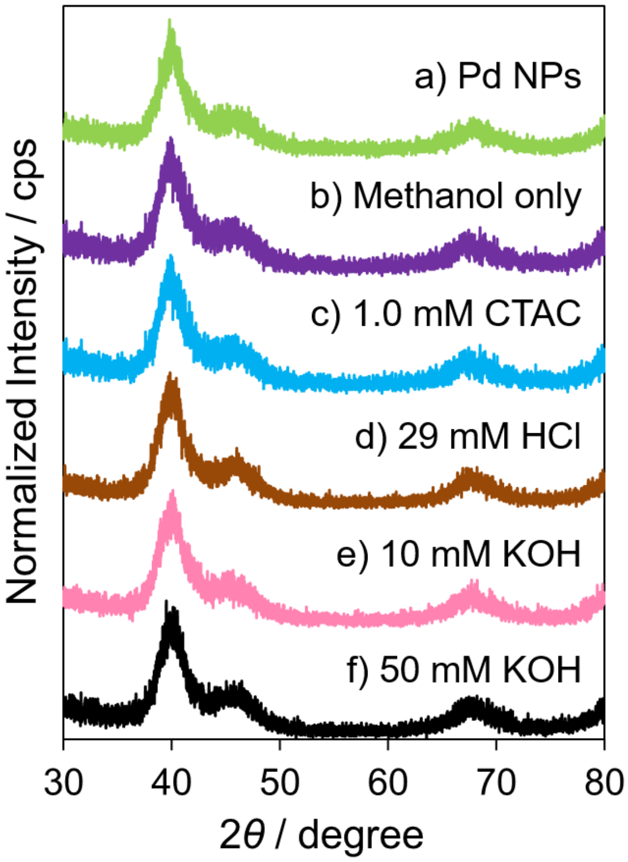

Figure 4-11. PXRD patterns of (a) oleylamine-capped Pd NPs and Pd structures prepared from the TOPO paste of Pd NPs by dipping into methanol with the (b) absence and presence of (c) 1.0 mM CTAC, (d) 29 mM HCl, (e) 10 mM KOH, and 50 mM KOH.

Table 4-2. Crystallite sizes of oleylamine-capped Pd NPs and Pd structures prepared from the TOPO paste of Pd NPs by dipping into methanol containing a sintering agent.

Sintering agents	Crystallite size ± standard error (nm)
Before RT chemical sintering (oleylamine-capped PdNPs)	3.3 ± 0.1
No addition (methanol only)	3.1 ± 0.1
1.0 mM CTAC	3.2 ± 0.1
29 mM HCl	3.2 ± 0.1
10 mM KOH	3.1 ± 0.1
50 mM KOH	3.3 ± 0.1

4-2-3 Suzuki Coupling Reaction with Porous Pd Structure as a Catalyst

In this section, the Suzuki coupling reaction of iodobenzene with 4-methylphenylboronic acid was investigated using porous Pd structures as heterogeneous catalysts (Scheme 4-1) [28]. The reactions were performed with KOH as a base in the presence of a 3.0 mol% Pd catalyst with respect to the substrate in methanol at 50 °C for 8 h. The conversion ratio (4-methylbiphenyl/(iodobenzene+4-methylbiphenyl)) was determined based on the peak area ratio at MCs obtained from GC-MS.

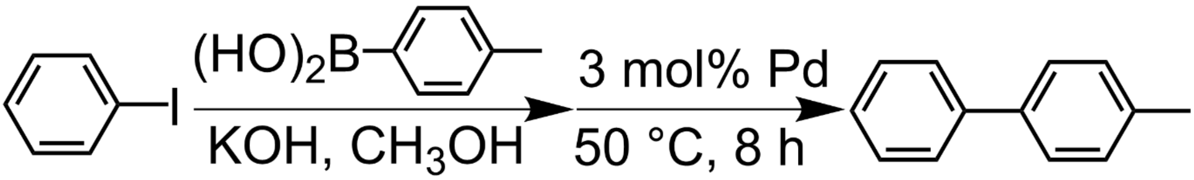

Scheme 4-1. Suzuki coupling reaction of iodobenzene with 4-methylphenylboronic acid catalyzed by Pd in methanol.

First, Pd structures prepared from the TOPO paste of Pd NPs by the RT chemical sintering with the various KOH concentrations were used as catalysts for the Suzuki coupling reaction. As for all catalysts, the coupling product was eventually obtained in ~95 % of the conversion ratio (Figure 4-12). The slopes of the molar ratio against reaction time (≤ 3h) were determined by linearly fitting the molar ratio (4-methylbiphenyl/iodobenzene) to reaction time (Figure 4-13, Table 4-3). The initial reaction rates were compared from the slopes. The reaction rate became larger with the increase of the KOH concentration (0.10~50 mM) in the RT chemical sintering. The increase of Pd methoxide and Pd-OH induced the activation of the Pd surface. Generally, Pd methoxide and Pd-OH promote transmetalation of boronic acid [1,34]. However, in the case of 50 mM KOH, the reaction rate was lower than that in the case of 10 mM KOH. In this case, the coalescence of Pd NPs excessively proceeded (Figure 4-6). Since the surface area of the Pd structure became smaller due to their excess coalescence, the catalytic activity conversely decreased. Furthermore, a leaching test of Pd was performed by inductivity coupled plasma atomic emission spectroscopy (ICP-AES) after the Suzuki coupling reaction with the porous Pd structure prepared by 10 mM KOH as the sintering agent. Dissolved Pd was detected in ~0.0015 mol% (4.4 × 10^{-5} mmol of Pd). This result is comparable to the nanoporous Pd in the Tanaka' study (<0.02 mol%) [28]. Therefore, we can say that the leaching amount of Pd is quite small in the current catalytic system.

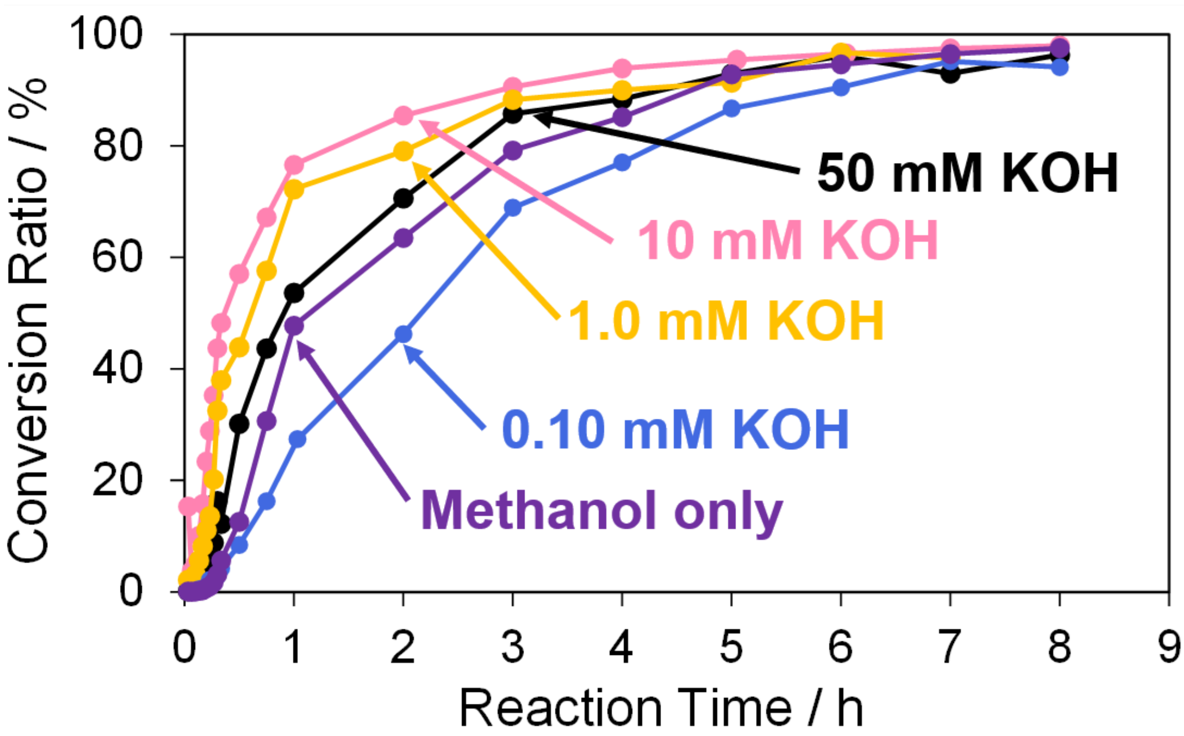

Figure 4-12. Conversion ratios versus reaction time in the Suzuki coupling reaction of iodobenzene with 4-methylphenylboronic acid in the cases using Pd structures prepared from the TOPO paste of Pd NPs by dipping into methanol without and with 0.10 mM, 1.0 mM, 10 mM, and 50 mM KOH.

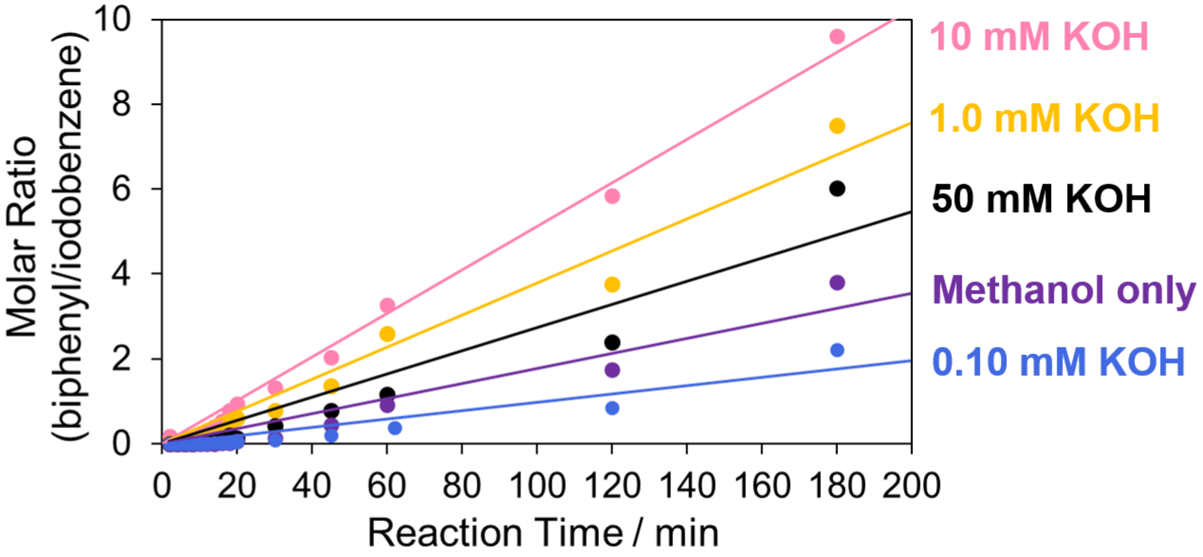

Figure 4-13. Fitting lines of the molar ratio (4-methylbiphenyl/iodobenzene) to the reaction time (≤ 3h) in the Suzuki coupling reaction of iodobenzene with 4-methylphenylboronic acid in the cases using Pd structures prepared from the TOPO paste of Pd NPs by dipping into methanol without and with 0.10 mM, 1.0 mM, 10 mM, and 50 mM KOH.

Table 4-3. Slopes of molar ratio (4-methylbiphenyl/iodobenzene) against reaction time (≤ 3h) in the cases using Pd structures prepared by dipping into methanol in the presence of various KOH concentrations.

Sintering agents	Slope (min^{-1})	Coefficient of determination, R^2
No addition (methanol only)	0.0177	0.934
0.10 mM KOH	0.0098	0.903
1.0 mM KOH	0.0378	0.974
10 mM KOH	0.0513	0.993
50 mM KOH	0.0273	0.926

Next, Pd structures prepared from the TOPO paste of Pd NPs by the RT chemical sintering with other types of sintering agents, which are 1.0 mM CTAC and 29 mM HCl, were used as catalysts for the same Suzuki coupling reaction as above (Figure 4-14). In both cases, the reaction rate was lower than that in the case of 10 mM KOH (Figure 4-15, Table 4-4). These results indicate that pre-activation of Pd by KOH affects the reactivity. In the cases of CTAC and HCl, Pd methoxide and Pd-OH are absent on the surface of porous Pd structures in advance. While the conversion ratio became finally 95 % in the case of CTAC, the conversion ratio was 85 % in the case of HCl. The Pd surface protonated in the sintering process may partly interrupt the formation of Pd methoxide and Pd-OH even in the Suzuki coupling reaction with KOH. As 10 mM KOH was the best sintering agent in this study, the porous Pd structure prepared from the TOPO paste of Pd NPs by the RT chemical sintering with the 10 mM KOH methanol solution was used for all of the following experiments.

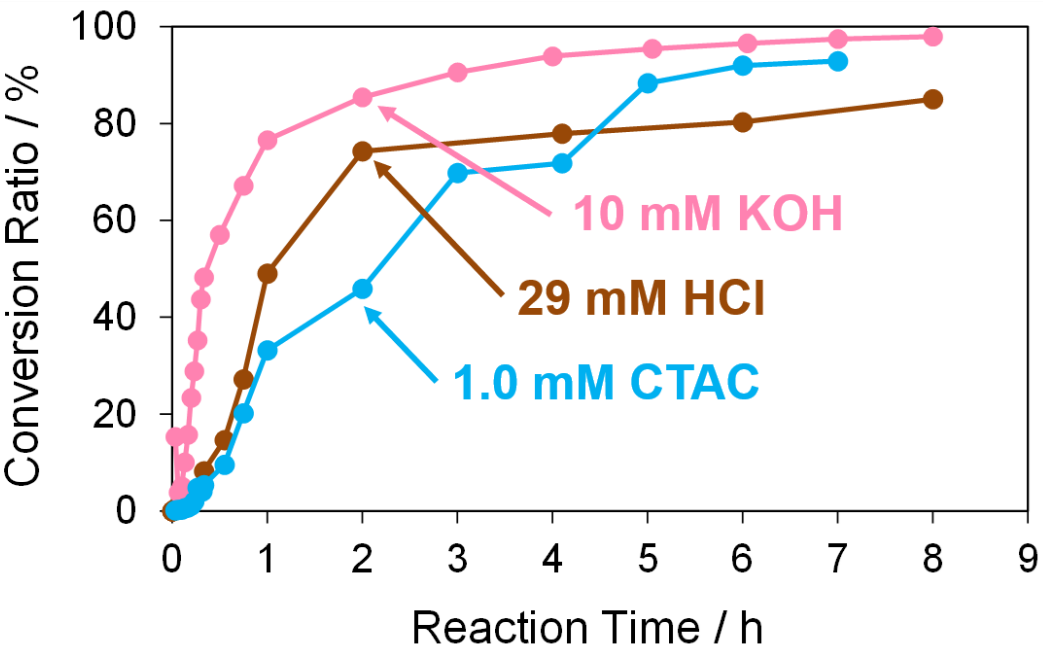

Figure 4-14. Conversion ratios versus reaction time in the Suzuki coupling reaction of iodobenzene with 4-methylphenylboronic acid in the cases using Pd structures prepared from the TOPO paste of Pd NPs by dipping into methanol with 10 mM KOH, 29 mM HCl, and 1.0 mM CTAC.

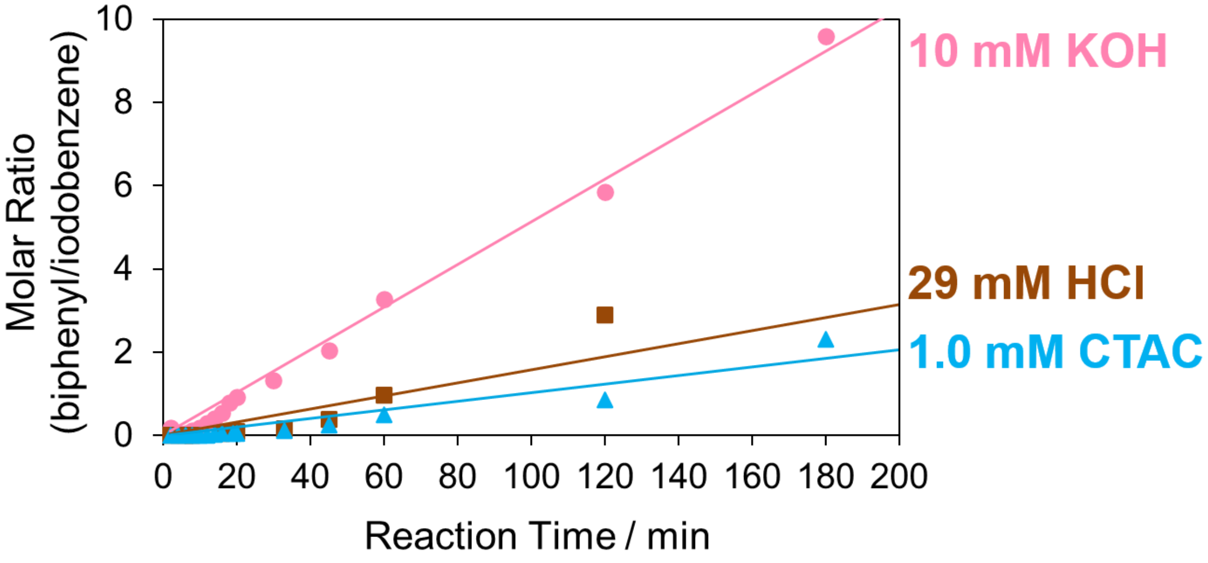

Figure 4-15. Fitting lines of the molar ratio (4-methylbiphenyl/iodobenzene) to the reaction time (≤ 3h) in the Suzuki coupling reaction of iodobenzene with 4-methylphenylboronic acid in the cases using Pd structures prepared from the TOPO paste of Pd NPs by dipping into methanol with 10 mM KOH, 29 mM HCl, and 1.0 mM CTAC.

Table 4-4. Slopes of molar ratio (4-methylbiphenyl/iodobenzene) against reaction time (≤ 3h) in the cases using Pd structures prepared by dipping into methanol in the presence of 10 mM KOH, 29 mM HCl, and 1.0 mM CTAC.

Added agents	Slope (min^{-1})	Coefficient of determination, R^2
10 m M KOH	0.0513	0.993
29 mM HCl	0.0157	0.933
1.0 mM CTAC	0.0103	0.909

Finally, the reusability of the porous Pd structure was investigated in the Suzuki coupling reaction under the same reaction condition as above. The recovery process in the current catalytic reaction is very simple. The catalysts and products can be separated easily by centrifugation. The recovered catalyst was washed with methanol several times and then reused after drying without further treatments. In Figure 4-16, the use numbers of catalysts were zero (Fresh), one (Reuse 1) and two (Reuse 2). Indeed, 4-methylbiphenyl was obtained in a high conversion yield even using the reused catalyst Reuse 1. However, the reaction rate of the reused catalyst was lower than that of "fresh". This is because further coalescence of the porous Pd structure proceeded after the first Suzuki coupling reaction, as confirmed by SEM observation of the catalyst (Figure 4-17). It seemed that KOH in the reaction medium promoted the coalescence of porous Pd structures. In the case of "Reuse 2", the reaction rate decreased compared with those of "fresh" and "Reuse 1". Similarly, further coalescence of the porous Pd structure proceeded after the second Suzuki coupling reaction (Figure 4-17).

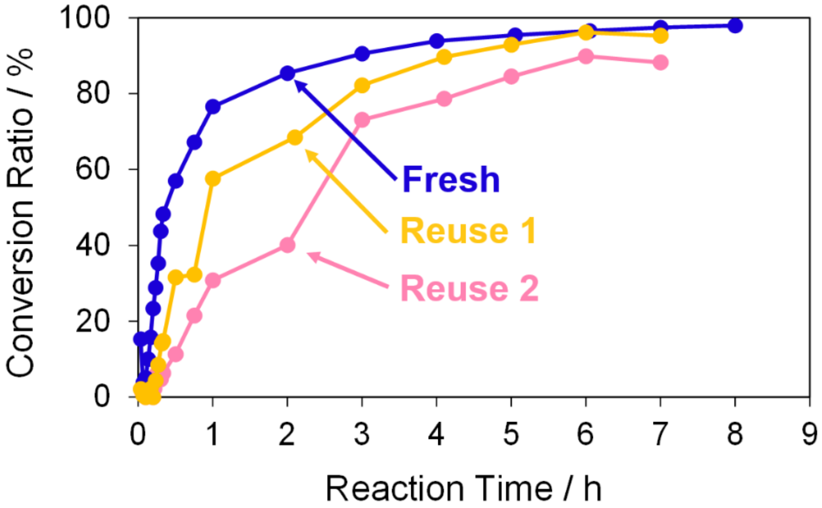

Figure 4-16. Conversion ratios versus reaction time in the repeated Suzuki coupling reaction of iodobenzene with 4-methylphenylboronic acid in the cases using fresh and recovered porous Pd strctures.

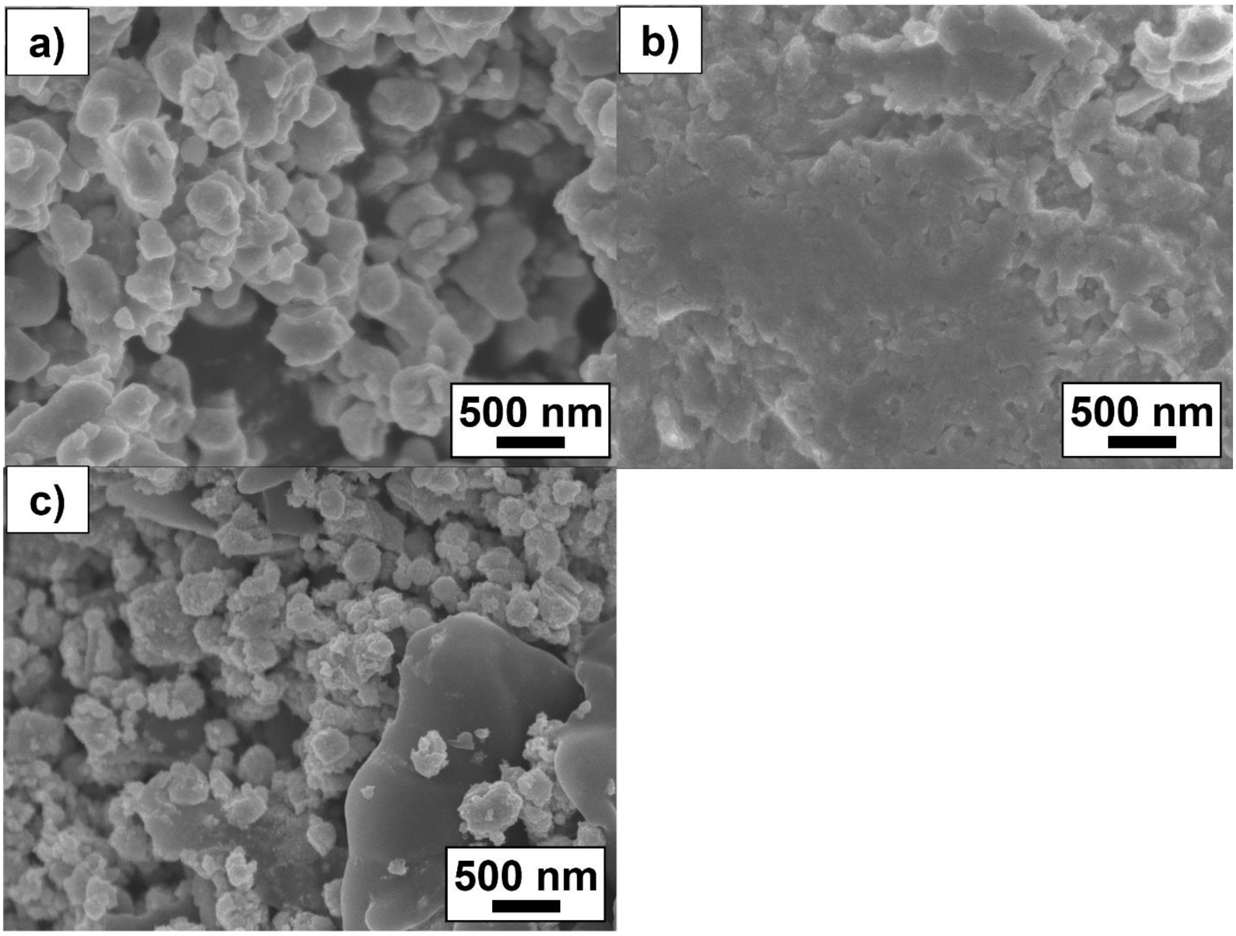

Figure 4-17. SEM images of Pd structures prepared from the TOPO paste of Pd NPs by dipping into the 10 mM KOH methanol solution for 30 min before and after the use for Suzuki coupling reaction in methanol. The use numbers of catalysts were (a) zero (Fresh), (b) one (Reuse 1), and (c) two (Reuse 2).

The catalytic ability of the porous Pd structure was also examined in the Suzuki coupling reaction with other reactants and solvent. The reaction of 4-iodophenol with phenylboronic acid was performed with K_2CO_3 as a base in the presence of a 1.0 mol% porous Pd structure with respect to the substrate in water at RT for 27 h (Scheme 4-2) [39], and 4-hydroxybiphenyl was obtained in 95 % of the conversion ratio (Figure 4-18). The catalytic activity of porous Pd structures was not affected by the reaction medium as opposed to that of the NP dispersion [40]. This contrast result would be due to the non-dispersion of porous Pd structures and the absence of organic ligands which may prevent the surface of Pd NPs from interacting with reactants.

The porous Pd structure showed similar reusability to that described above. Whatever porous Pd structures were used, the reaction rate was lower than that of "fresh". In the case of "Reuse 2", the conversion ratio significantly decreased. As in the above case, further coalescence of the porous Pd structure proceeded after the Suzuki coupling reaction (Figure 4-19).

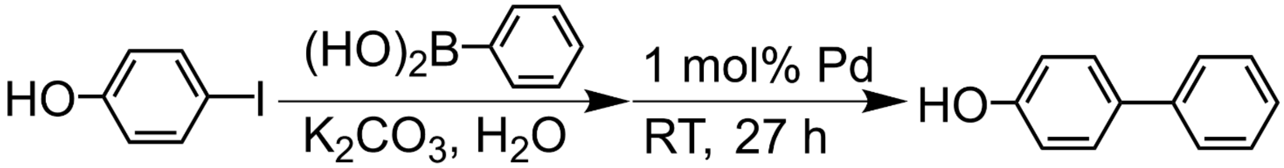

Scheme 4-2. Suzuki coupling reaction of 4-iodophenol with phenylboronic acid catalyzed by Pd in water.

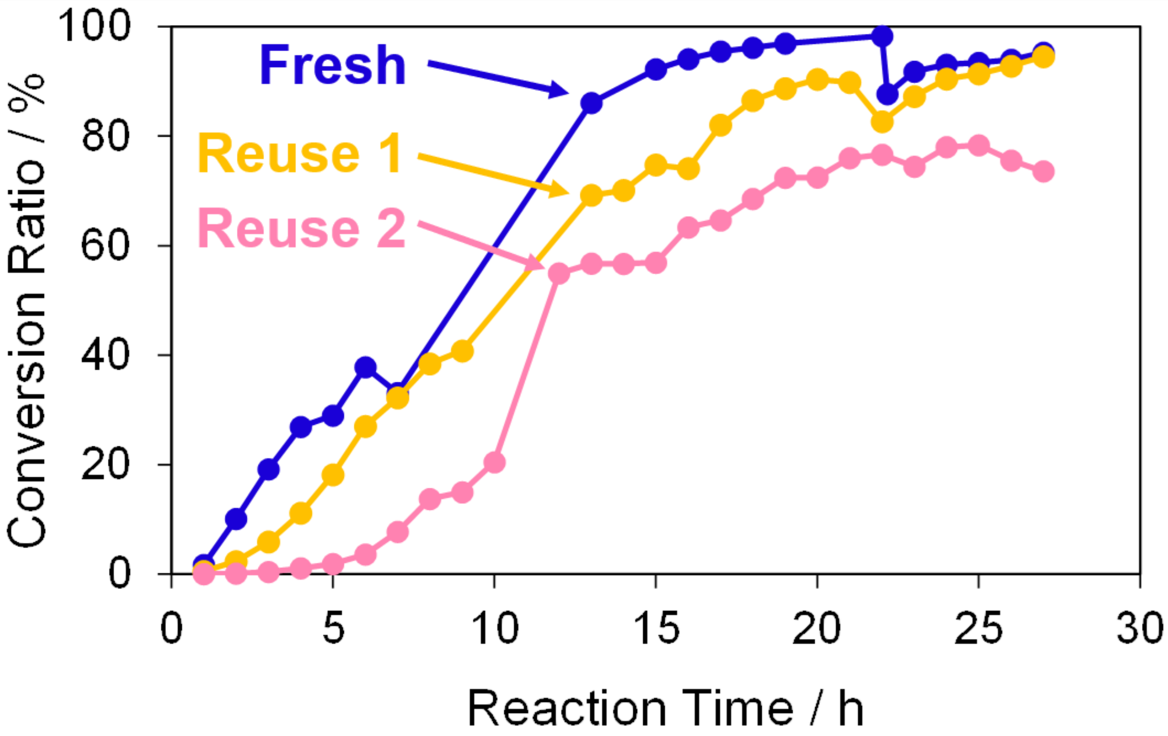

Figure 4-18. Conversion ratios versus reaction time in the Suzuki coupling reaction of 4-iodophenol with phenylboronic acid with in the case using fresh and recovered porous Pd structures.

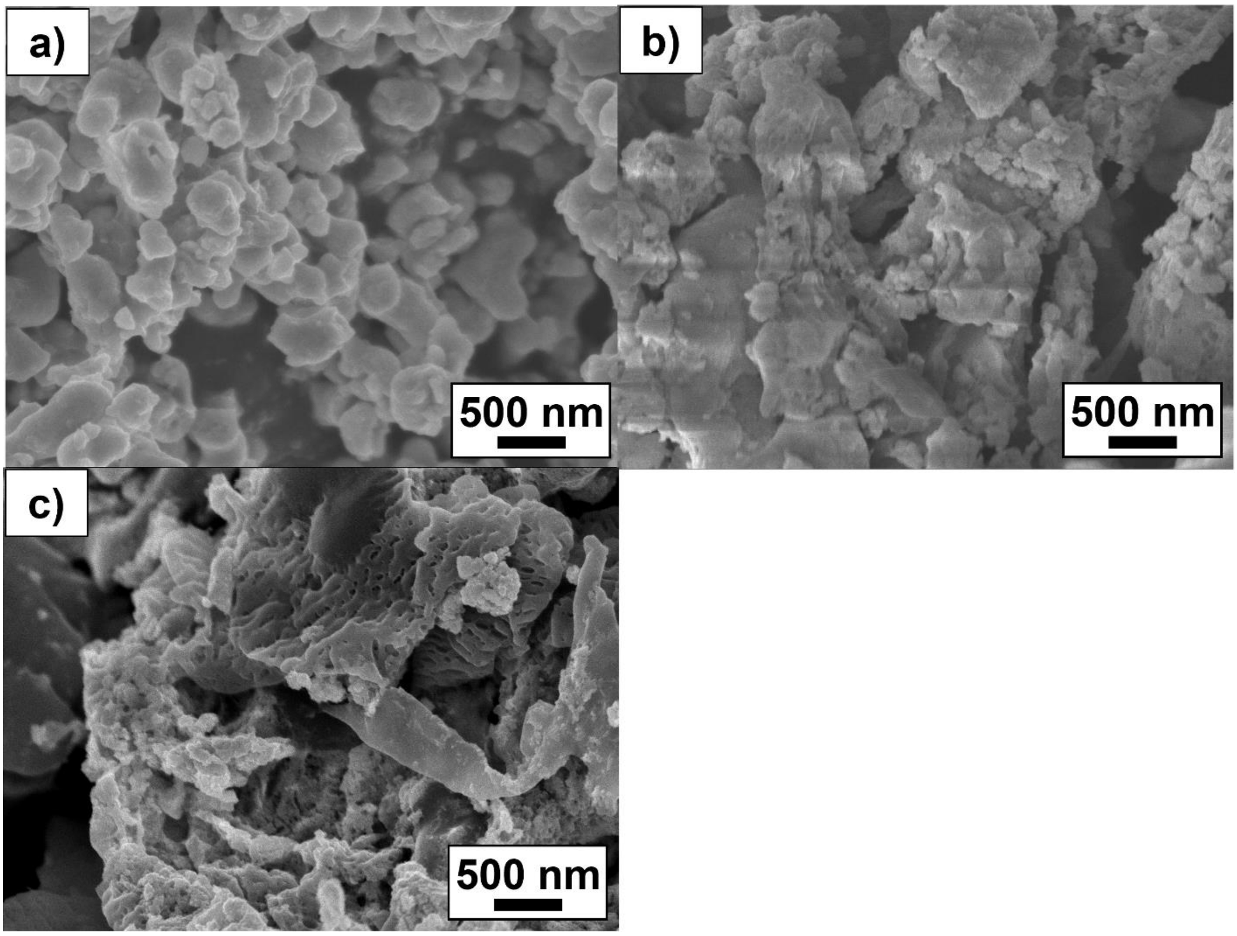

Figure 4-19. SEM images of Pd structures prepared from the TOPO paste of Pd NPs by dipping into the 10 mM KOH methanol solution for 30 min before and after the use for Suzuki coupling reaction in water. The use numbers of catalysts were (a) zero (Fresh), (b) one (Reuse 1), and (c) two (Reuse 2).

4-2-4 Comparison between Porous Pd Structure and Pd on Carbon

The catalytic activity of the porous Pd structure was compared with those of commercial Pd/C (Pd 5.0 wt%) and oleylamine-capped Pd NP in the Suzuki coupling reaction as shown in Scheme 1. The reactions of iodobenzene with 4-methylphenylboronic acid were performed with KOH as a base in the presence of a 3.0 mol% Pd catalyst with respect to the substrate in methanol at 50 °C for 8 h (Figure 4-20). The conversion ratio and reaction rate in the case using porous Pd structure were almost equal to that in the case using Pd/C (Figure 4-21, Table 4-5). In other words, the porous Pd structure showed similar catalytic activity to that of Pd/C. On the other hand, the reaction rate was significantly lower in the case using Pd NP. This result may be attributed to the fact that the surface of Pd NPs less effectively interacts with reactants due to the presence of oleylamine. All these results indicate that the RT chemical sintering makes the catalytic property of Pd more active.

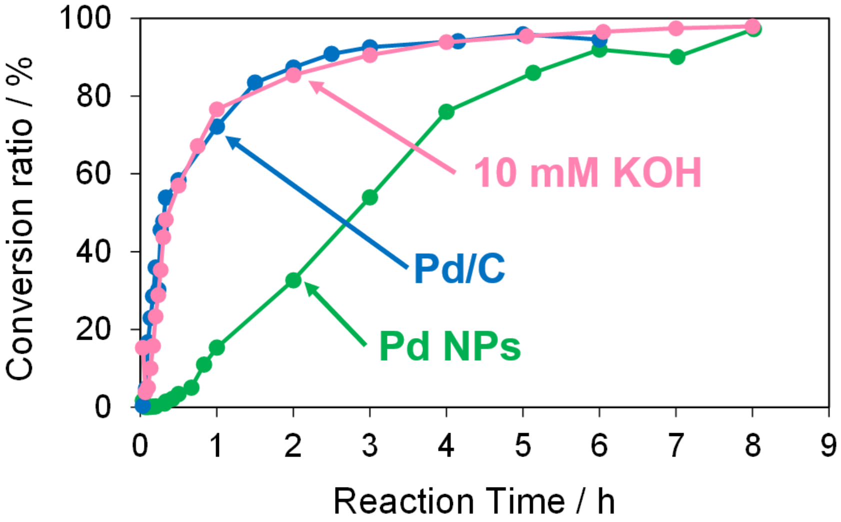

Figure 4-20. Conversion ratios versus reaction time in the Suzuki coupling reaction of iodobenzene with 4-methylphenylboronic acid in the cases using porous Pd structures, commercial Pd/C, and oleylamine-capped Pd NP.

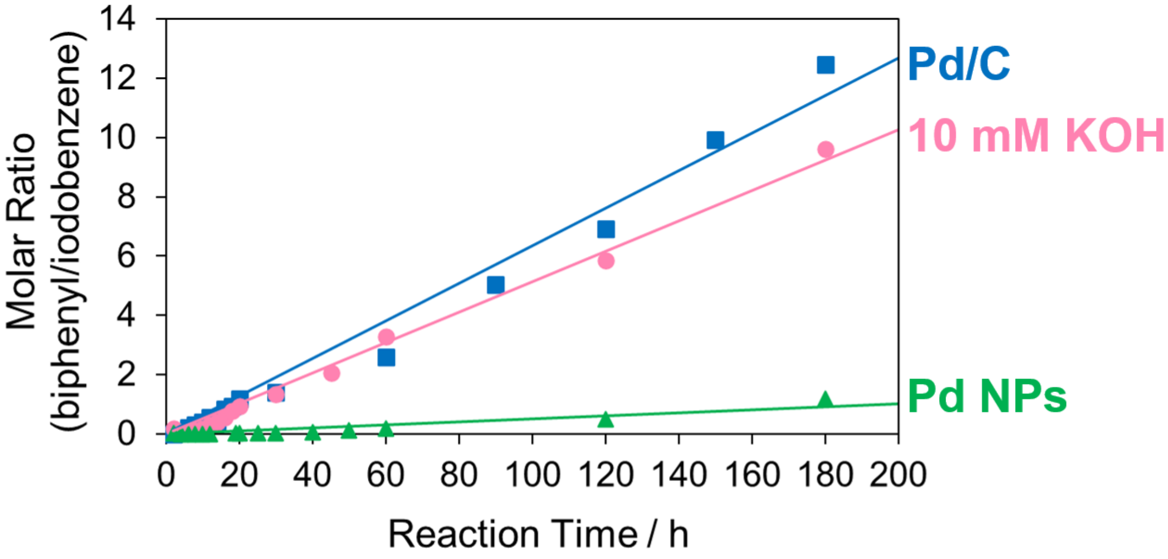

Figure 4-21. Fitting lines of the molar ratio (4-methylbiphenyl/iodobenzene) to the reaction time (≤ 3 h) in the Suzuki coupling reaction of iodobenzene with 4-methylphenylboronic acid in the cases using porous Pd structures, Pd/C, and oleylamine-capped Pd NP.

Table 4-5. Slopes of molar ratio (4-methylbiphenyl/iodobenzene) against reaction time (≤ 3h) in the cases using Pd structures prepared by dipping into methanol in the presence of porous Pd structure, commercial Pd/C and oleylamine-capped Pd NP.

Catalysts	Slope (min^{-1})	Coefficient of determination, R^2
Porous Pd structure (10 m M KOH)	0.0513	0.993
Pd/C	0.0634	0.987
Oleylamine-capped Pd NPs	0.0051	0.889

Section 4-3: Summary

The porous Pd structures were prepared by the RT chemical sintering of the Pd NP paste. By using TOPO as a sacrificial template, porous Pd structures were obtained via dipping into methanol containing KOH or HCl as a sintering agent. The catalytic activities of porous Pd structures in the Suzuki coupling reaction increased with the increase of the KOH concentration in the sintering process. In contrast, the catalytic activity of the porous Pd structure obtained by HCl was low. These results indicate that pre-activation of porous Pd structures by KOH increases the catalytic activities. As opposed to the Pd NPs, the reaction solvent hardly affected the catalytic activity of porous Pd structures due to the absence of ligands. We expect that the porous Pd structure obtained by this method is a good candidate for environmentally-friendly heterogeneous catalysts and thus this method could be widely applicable to the preparation of various porous metal structures.

Section 4-4: Experiments

4-4-1 Materials

All the chemicals and solvents were obtained commercially and used without further purification. Pd (II) acetylacetonate and borane-triethylamine complex were purchased from Sigma-Aldrich. Tri-*n*-octylphosphine oxide (TOPO) and *n*-octadecane were purchased from Aldrich. 1-dodecanol was purchased from Nakarai Tesque, Inc. Potassium hydroxide (KOH), potassium carbonate (K_2CO_3), cetyltrimethylammonium chloride (CTAC), oleylamine, iodobenzene, and palladium-activated carbon (Pd 5.0 wt%, Pd/C) were purchased from Wako Pure Chemical Industries, Ltd. Hydrogen chloride methanol solution (6.6 w/w%), 4-iodophenol, phenylboronic acid, and 4-methylphenylboronic acid were purchased from Tokyo Chemical Industries Co., Ltd.

4-4-2 Synthesis of Pd NPs and Preparation of Pd NPs Paste

Oleylamine-capped Pd NPs were synthesized based on the method reported by Mazumder *et al.* [33]. Typically, Pd(II) acetylacetonate (70 mg) was solved to 15 mL of oleylamine by stirring at 60 °C for 10 min. After this solution was heated at 90 °C, 0.30 mL of borane-triethylamine complex as a reducing agent was added to this solution. Then, this solution was heated at 90 °C for 60 min. After the reaction, about 30 mL of methanol was added as an antisolvent to the dispersion of Pd NPs (about 20 mL). The dispersion was then centrifuged at 15 000 rpm for 10 min. After the removal of the supernatant, about 20 mL of methanol was added to the residue again. The centrifugation was then carried out at 5000 rpm for 10 min. The same procedure was repeated twice. The obtained oleylamine-capped Pd NPs (20 mg) were dried in air.

The Pd NPs pastes were fabricated as below. First, oleylamine-capped Pd NPs (10 mg) were dispersed in 18 mL of *n*-heptane at a concentration of 0.56 g L^{-1}. Next, the *n*-heptane solution of sacrificial template (5.0 g L^{-1}, 2 mL) was added to the dispersion of Pd NPs. The sacrificial templates used here were TOPO, *n*-octadecane, and 1-dodecanol. The concentrations after mixing were adjusted to 0.50 g L^{-1} of Pd NP. The mixture was stirred at 40 °C for an hour. Then, *n*-heptane was completely removed by a rotary evaporator to increase the NP concentration in the paste. The concentrated sacrificial template dispersion of Pd NPs was used without purification as the Pd NPs paste (metal/sacrificial template = 8.6/500 w/w%) in the preparation of porous Pd structures (see following paragraph). Although the paste contains oleylamine as an impurity, the amount (about 1.4 mg) is very small compared with that (100 mg) of the sacrificial template. Therefore, the effect of impurities would be negligible.

4-4-3 Preparation of Porous Pd Structures

The Pd NPs pastes for the fabrication of porous Pd structure were prepared as mentioned in the section 4-3-2. Glass substrates were washed with acetone and deionized water before use. Several drops of the fabricated Pd NPs paste were cast onto the glass substrate (24 mm × 24 mm). This substrate was dipped in 20 mL of methanol containing a sintering agent at RT (about 25 °C) for 30 min in air. The sintering agents used here were CTAC, HCl, and KOH. Methanol was used as a solvent in all the cases. After the RT chemical sintering, the obtained porous Pd structures were washed by centrifugation with pure methanol (5000 rpm, 5 min). After the removal of the supernatant, pure methanol was again added to the residue under an ultrasonication. The centrifugation was carried out at 4000 rpm for 10 min. The same procedure was repeated twice. Then, the obtained porous Pd structures were dried in air for 30 min at RT.

4-4-4 General Procedure of Suzuki Coupling Reaction with Pd as a Catalyst

The Suzuki-coupling reaction in methanol was conducted based on the method reported by Tanaka et al. (Scheme 1) [28]. Typically, iodobenzene (1.0 mmol) and 4-methylphenylboronic acid (1.4 mmol) were added to the KOH methanol solution (5.0 mmol / 4.0 mL) at RT. This solution was added into a centrifuge tube containing a 3.0 mol% Pd catalyst (porous Pd structure, Pd/C and Pd

NPs) with respect to the substrate and the reaction mixture was stirred for 8 h at 50 °C. For tracing the reaction, 90 μL of the reaction solution was fractionated. The fractionated solution was filtrated by the membrane filter to remove Pd catalysts. The filtrated solution was added to the mixed solution of n-hexane and water. The organic compounds were extracted to the *n*-hexane phase. The reaction ratio of 4-methylbiphenyl was coursed by analyzing the extracted solution with gas chromatography-mass spectrometry (GC-MS). The reaction ratio was determined by the calibration curve described later.

The Suzuki-coupling reaction in water was conducted based on the method reported by Sakurai et al. (Scheme 2) [39]. Typically, 4-iodophenol (3.0 mmol) and phenylboronic acid (5.0 mmol) were added to the K_2CO_3 aqueous solution (9.0 mmol / 30 mL) at RT. This solution was added into a centrifuge tube containing a 1.0 mol% porous Pd structure with respect to the substrate, and the reaction mixture was stirred for 27 h at RT. For tracing the reaction, 90 μL of the reaction solution was fractionated. The fractionated solution was filtrated by the membrane filter for the removal of Pd catalysts. The filtrated solution was added to the mixed solution of *n*-hexane and 1.2 M HCl aqueous solution. The organic compounds were extracted from the aqueous phase to the *n*-hexane phase. The reaction ratio of 4-hydroxybiphenyl was determined by analyzing the extracted solution with GC-MS.

The leaching test of Pd in the Suzuki coupling reaction was performed by ICP-AES. The sample solution was prepared by the following procedure. After the reaction was completed, the reaction solution (4.0 mL) was evaporated. The residue was dissolved in aqua regia (3.0 mL) and H_2SO_4 (1.0 mL), and then it was diluted with the 1% HNO_3 and 2 % HCl aqueous solution up to 9.0 mL. The precipitate was filtered off, and the filtrate was analyzed by ICP-AES.

The conversion ratio (yield of biphenyl derivative) was determined by the calibration curve of molar ratio (biphenyl/iodine phenyl) to main peak area intensity ratio in mass chromatogram (MC). The MC was collected with the selected ion monitoring (SIM) method. The SIM method can detect selected ions at high sensitivity because only these ions were sent to a detector of MS. The calibration curves covered wide range of molar ratios (biphenyl/iodine phenyl) (Figure 4-22).

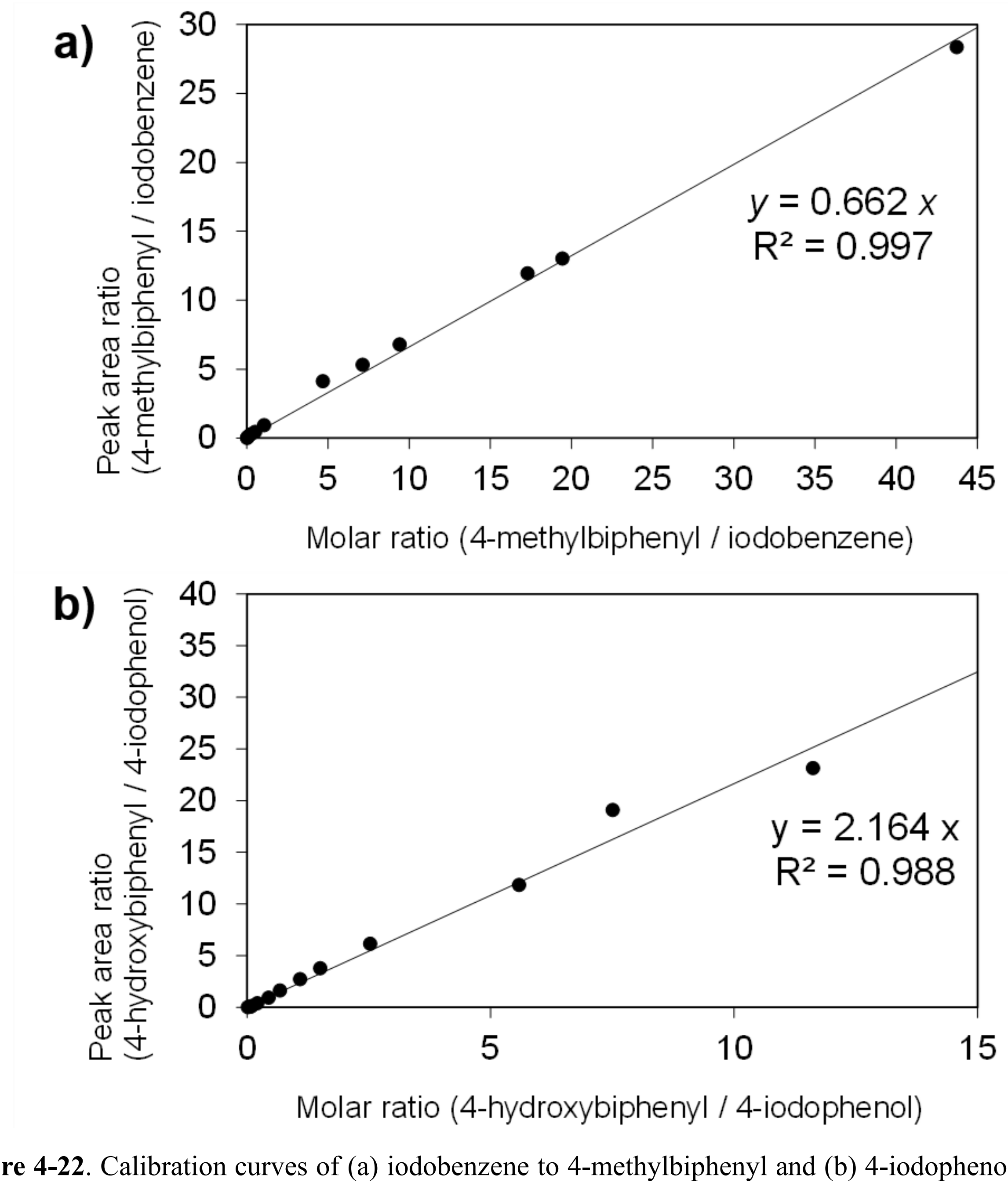

Figure 4-22. Calibration curves of (a) iodobenzene to 4-methylbiphenyl and (b) 4-iodophenol to 4-hydroxybiphenyl in MC.

4-4-5 Characterization

Transmission electron microscopy (TEM) images were taken at 100 kV with a JEM-2100 (JEOL, Japan) for the observation of synthesized Pd NPs and porous Pd structures. The diameter of NPs was evaluated by ImageJ software. The morphology of porous Pd structures was characterized by field emission scanning electron microscopy (FE-SEM, JSM-6700F and JSM-7800F, JEOL, Japan). Thermogravimetric analysis (TGA) was performed by a ThermoMass Photo (Rigaku, Japan). Total ion chromatograms (TICs) for the analysis of organic residue in Pd NPs were obtained from GC-MS, QP2010 Plus (Shimadzu, Japan). Here, Ultra ALLOY UA5-30M-0.25F (Frontier Laboratories Ltd., Japan) was used as a column. The Pd NPs for GC-MS were heated by a PY-3030D pyrolyzer (Frontier Laboratories Ltd., Japan) at 300 °C before injection. X-ray diffraction (XRD) patterns were recorded using a MiniFlexII (Rigaku, Japan, Cu Kα radiation) equipped with a Kα filter operating at 30 kV and 15 mA. The crystallite size was calculated by the Scherrer equation: $D = 0.9\lambda/\beta\cos\theta$, where D is the crystallite size, λ is the wavelength of X-ray, β is the full width at half maximum (FWHM) of the diffraction peak and θ is the diffraction angle. X-ray photoelectron spectroscopy (XPS) measurements were performed by a KRATOS AXIS Ultra DLD X-ray photoelectron spectrometer (Shimadzu, Japan). The leached Pd was quantitated by ICP-AES (SPECTRO BLUE, Hitachi, Ltd., Japan).

Reference

[1] Peral, D.; Gómez-Villarraga, F.; Sala, X.; Pons, J.; Bayón, J. C.; Ros, J.; Guerrero, M.; Vendier, L.; Lecante, P.; García-Antón, J.; Philippot, K. Palladium catalytic systems with hybrid pyrazole ligands in C–C coupling reactions. Nanoparticles *versus* molecular complexes. *Catal. Sci. Technol.* **2013**, *3*, 475–489.

[2] Hosokawa, S.; Shibano, T.; Koga, H.; Matsui, M.; Asakura, H.; Teramura, K.; Okumura M.; Tanaka, T. Excellent catalytic activity of a Pd-promoted MnO_x catalyst for purifying automotive exhaust gases. *ChemCatChem* **2020**, *12*, 4276–4280.

[3] Bianchini, C.; Shen, P. K. Palladium-based electrocatalysts for alcohol oxidation in half cells and in direct alcohol fuel cells. *Chem. Rev.* **2009**, *109*, 4183–4206.

[4] Miyaura, N.; Suzuki, A. Palladium-catalyzed cross-coupling reactions of organoboron compounds. *Chem. Rev.* **1995**, *95*, 2457–2483.

[5] Littke, A. F.; Fu, G. C. Palladium-catalyzed coupling reactions of aryl chlorides., *Angew. Chem. Int. Ed.* **2002**, *41*, 4176–4211.

[6] Li, Y.; Boone, E.; El-Sayed, M. A. Size effects of PVP−Pd nanoparticles on the catalytic Suzuki reactions in aqueous solution. *Langmuir* **2002**, *18*, 4921–4925.

[7] Cassol, C. C.; Umpierre, A. P.; Machado, G.; Wolke, S. I.; Dupont, J. The role of Pd nanoparticles in ionic liquid in the Heck reaction. *J. Am. Chem. Soc.* **2005**, *127*, 3298–3299.

[8] Yonezawa, T.; Kawai, K.; Kawakami, H.; Narushima, T. Preparation of water-dispersible palladium nanoparticles stabilized by carbon–palladium bonds and application to Suzuki–Miyaura coupling in water. *Bull. Chem. Soc. Jpn.* **2016**, *89*, 1230–1232.

[9] Chen, D.; Yang, W.; Jiao, L.; Li, L.; Yu, S.-H.; Jiang, H.-L. Boosting catalysis of Pd nanoparticles in MOFs by pore wall engineering: the roles of electron transfer and adsorption energy. *Adv. Mater.* **2020**, *32*, 2000041.

[10] Shaikh, M. N. Pd nanoparticles on green support as dip-catalyst: a facile transfer hydrogenation of olefins and *N*-heteroarenes in water. *RSC Adv*. **2019**, *9*, 28199–28206.

[11] Shao, X.; Miao, X.; Yu, X.; Wang, W.; Ji, X. Efficient synthesis of highly dispersed ultrafine Pd nanoparticles on a porous organic polymer for hydrogenation of CO_2 to formate. *RSC Adv*. **2020**, *10*, 9414–9419.

[12] Yang, Y.; Niu, H.; Zhao, W.; Xu, L.; Zhang, H.; Cai, Y. Ultrafine Pd nanoparticles loaded benzothiazole-linked covalent organic framework for efficient photocatalytic C–C cross-coupling reactions. *RSC Adv*. **2020**, *10*, 29402–29407.

[13] Choi, H. R.; Woo, H.; Jang, S.; Cheon, J. Y.; Kim, C.; Park, J.; Park, K. H.; Joo, S. H. Ordered mesoporous carbon supported colloidal Pd nanoparticle based model catalysts for Suzuki coupling reactions: impact of organic capping agents. *ChemCatChem* **2012**, *4*, 1587–1594.

[14] Gu, C. D.; Xu, X. J.; Tu, J. P. Fabrication and wettability of nanoporous silver film on copper from choline chloride-based deep eutectic solvents. *J. Phys. Chem. C* **2010**, *114*, 13614–13619.

[15] Li, Z.; Xu, J.; Gu, X.; Wang, K.; Wang, W.; Zhang, X.; Zhang, Z.; Ding, Y. Selective gas-phase oxidation of alcohols over nanoporous silver. *ChemCatChem* **2013**, *5*, 1705–1708.

[16] Li, S.; Chien, C.-L.; Searson, P. C. Fabrication of nanoporous nickel by electrochemical dealloying. *Chem. Mater.* **2004**, *16*, 3125–3129.

[17] Niu, X.; Lan, M.; Zhao, H.; Chen, C. Highly sensitive and selective nonenzymatic detection of glucose using three-dimensional porous nickel nanostructures. *Anal. Chem.* **2013**, *85*, 3561–3569.

[18] Chen, Q.; Zhang, X.; Su, S.; Xu, Z.; Li, N.; Li, Y.; Zhou, H.; Bao, M.; Yamamoto, Y.; Jin, T. Nanoporous gold-catalyzed diboration of methylenecyclopropanes via a distal bond cleavage. *ACS Catal.* **2018**, *8*, 5901–5906.

[19] Welch, A. J.; DuChene, J. S.; Tagliabue, G.; Davoyan, A.; Cheng, W.-H.; Atwater, H. A. Nanoporous gold as a highly selective and active carbon dioxide reduction catalyst. *ACS Appl. Energy Mater.* **2019**, *2*, 164–170.

[20] Kloke, A.; von Stetten, F.; Zengerle, R.; Kerzenmacher, S. Strategies for the fabrication of porous platinum electrodes. *Adv. Mater.* **2011**, *23*, 4976–5008.

[21] Steyskal, E.-M.; Qi, Z.; Pölt, P.; Albu, M.; Weissmüller, J.; Würschum, R. Electrochemically tunable resistance of nanoporous platinum produced by dealloying. *Langmuir* **2016**, *32*, 7757–7764.

[22] Cherevko, S.; Kulyk, N.; Chung, C.-H. Nanoporous palladium with sub-10 nm dendrites by electrodeposition for ethanol and ethylene glycol oxidation. *Nanoscale* **2012**, *4*, 103–105.

[23] Li, Z.; Lin, S.; Ji, L.; Zhang, Z.; Zhang, X.; Ding, Y. Nanoporous palladium catalyzed silicon-based one-pot cross-coupling reaction of aryl iodides with organosilanes. *Catal. Sci. Technol.* **2014**, *4*, 1734–1737.

[24] Hoang, T. T. H.; Verma, S.; Ma, S.; Fister, T. T.; Timoshenko, J.; Frenkel, A. I.; Kenis, P. J. A.; Gewirth, A. A. Nanoporous copper–silver alloys by additive-controlled electrodeposition for the selective electroreduction of CO_2 to ethylene and ethanol. *J. Am. Chem. Soc.* **2018**, *140*, 5791–5797.

[25] Son, J.; Cho, S.; Lee, C.; Lee, Y.; Shim, J. H. Spongelike nanoporous Pd and Pd/Au dtructures: facile synthesis and enhanced electrocatalytic activity. *Langmuir* **2014**, *30*, 3579–3588.

[26] Chen, L.; Guo, H.; Fujita, T.; Hirata, A.; Zhang, W.; Inoue, A.; Chen, M. Nanoporous PdNi bimetallic catalyst with enhanced electrocatalytic performances for electro-oxidation and oxygen reduction reactions. *Adv. Funct. Mater.* **2011**, *21*, 4364–4370.

[27] Li, C.; Iqbal, M.; Lin, J.; Luo, X.; Jiang, B.; Malgras, V.; Wu, K. C.-W.; Kim, J; Yamauchi, Y. Electrochemical deposition: an advanced approach for templated synthesis of nanoporous metal architectures. *J. Am. Chem. Soc.* **2018**, *51*, 1764–1773.

[28] Tanaka, S.; Kaneko, T.; Asao, N.; Yamamoto, Y.; Chen, M.; Zhang, W.; Inoue, A. A nanostructured skeleton catalyst: Suzuki-coupling with a reusable and sustainable nanoporous metallic glass Pd-catalyst. *Chem. Commun.* **2011**, *47*, 5985–5987.

[29] Felpin, F.-X.; Ayad, T.; Mitra, S. Pd/C: An old catalyst for new applications – Its use for the Suzuki–Miyaura reaction. *Eur. J. Org. Chem.* **2006**, *2006*, 2679–2690.

[30] Yin, L.; Liebscher, J. Carbon–carbon coupling reactions catalyzed by heterogeneous palladium catalysts. *Chem. Rev.* **2007**, *107*, 133–173.

[31] Lamblin, M.; Nassar-Hardy, L.; Hierso, J.-C.; Fouquet, E.; Felpin, F.-X. Recyclable heterogeneous palladium catalysts in pure water: sustainable development in Suzuki, Sonogashira, and Tsuji-Trost Reactions. *Adv. Synth.*

Catal. **2010**, *352*, 33–79.

[32] Ohtaka, A.; Kawase, M.; Aihara, S.; Miyamoto, Y.; Terada, A.; Nakamura, K.; Hamasaka, G.; Uozumi, Y.; Shinagawa, T.; Shimomura, O.; Nomura, R. Poly(tetrafluoroethylene)-stabilized metal nanoparticles: preparation and evaluation of catalytic activity for Suzuki, Heck, and arene hydrogenation in water. *ACS Omega* **2018**, *3*, 10066–10073.

[33] Mazumder, V.; Sun, S. Oleylamine-mediated synthesis of Pd nanoparticles for catalytic formic acid oxidation. *J. Am. Chem. Soc.* **2009**, *131*, 4588–4589.

[34] Amatore, C.; Jutand, A.; Duc, G. L. Kinetic data for the transmetalation/reductive elimination in palladium-catalyzed Suzuki–Miyaura reactions: unexpected triple role of hydroxide ions used as base. *Chem. - Eur. J.* **2011**, *17*, 2492–2503.

[35] Yamamoto, M.; Kakiuchi, H.; Kashiwagi, Y.; Yoshida, Y.; Ohno, T.; Nakamoto, M. Synthesis of Ag–Pd alloy nanoparticles suitable as precursors for ionic migration-resistant conductive film. *Bull. Chem. Soc. Jpn.* **2010**, *83*, 1386–1391.

[36] Batista, J.; Pintar, A.; Mandrino, D.; Jenko, M.; Martin, V. XPS and TPR examinations of γ-alumina-supported Pd-Cu catalysts. *Appl. Catal., A* **2001**, *206*, 113–124.

[37] Yamamoto, S.; Kinoshita, H.; Hashimoto, H.; Nishina, Y. Facile preparation of Pd nanoparticles supported on single-layer graphene oxide and application for the Suzuki–Miyaura cross-coupling reaction. *Nanoscale* **2014**, *6*, 6501–6505.

[38] Fujii, S.; Matsuzawa, S.; Nakamura, Y.; Ohtaka, A.; Teratani, T.; Akamatsu, K.; Tsuruoka, T.; Nawafune, H. Synthesis and characterization of polypyrrole–palladium nanocomposite-coated latex particles and their use as a catalyst for Suzuki coupling reaction in aqueous media. *Langmuir* **2010**, *26*, 6230–6239.

[39] Sakurai, H.; Tsukuda, T.; Hirao, T. Pd/C as a reusable catalyst for the coupling reaction of halophenols and arylboronic acids in aqueous media. *J. Org. Chem.* **2002**, *67*, 2721–2722.

[40] Janani, S.; Stevenson, P.; Veerappan, A. Activity of catalytic silver nanoparticles modulated by capping agent

hydrophobicity. *Colloids Surf., B* **2014**, *117*, 528–533.

General Conclusions

In this thesis, the author developed a novel RT chemical sintering method of metal NPs for the fabrication of metal thin films. As the first step of the objective, the coalescence of metal NPs was investigated under various conditions. Next, the author performed the RT chemical sintering of Ag, Cu@Ag, and Pd NPs in an organic solvent containing a sintering agent. Based on these knowledges, conductive metal thin films and heterogeneous metal catalysts were fabricated by the RT chemical sintering, and their properties were examined.

In Chapter 1, properties of metal NPs and their general sintering methods for printed electronics were described. From these findings, the author decided to fabricate conductive metal thin films and heterogeneous metal catalysts by the RT chemical sintering.

In Chapter 2, on the surface of Ag NPs, ligand exchanges from oleic acid to OA, DDT, and TOPO were carried out and the NPs were washed with methanol as an antisolvent after the reactions. In the case of the ligand exchange with TOPO, most of ligands desorbed from the particle surface and the crystallite size significantly increased. Based on this result, pure Ag thin films were prepared from the TOPO-capped Ag NP paste by dipping into methanol containing a sintering agent. The lowest electrical resistivity in this study was $(1.2 \pm 0.5) \times 10^{-5}$ Ω m, which was attained by dipping of TOPO-capped Ag NPs into the 0.20 mM CTAC methanol solution for 120 min at RT. The author revealed that electrical resistivity of the Ag thin films was dependent on sintering agent, its concentration, dipping time, ligand of Ag NP, and polarity of dipping solvent. Notably, it is possible that the excess addition of sintering agents induced not only the formation of Ag thin film but also the generation of Ag_2O or AgCl. Therefore, the appropriate concentration of sintering agents should be added in the RT chemical sintering with organic solvents.

In Chapter 3, the ligand exchange from oleylamine/oleic acid to TOPO was carried out on the surface of Cu@Ag NPs and the NPs were sintered at RT with methanol containing a sintering agent and/or a reducing agent. In the case of 29 mM HCl, the crystallite size significantly increased. In addition, Ag and Cu were hardly oxidized during the process. On the basis of these results, a Cu/Ag thin film was prepared from TOPO-capped Cu@Ag NPs by dipping into methanol containing 29 mM HCl for 30 min. The electrical resistivity of the obtained thin film was $(5.1 \pm 1.7) \times 10^{-5}$ Ω m. Under strong acidic conditions, protonated TOPO rapidly desorbed from Cu@Ag NP, which brought about the effective coalescence with slight oxidation.

In Chapter 4, porous Pd structures were prepared from the Pd NP paste mixed with the sacrificial template by dipping into methanol containing a sintering agent. Owing to TOPO as a sacrificial template, porous Pd structures were obtained by dipping methanol into containing KOH as a sintering agent. The catalytic activities in the Suzuki coupling reaction increased with the increase of the KOH concentration in the RT sintering. The porous Pd structure prepared by the 10 mM KOH methanol solution showed the highest catalytic activity.

In summary, this study showed that the RT chemical sintering with methanol containing a sintering agent could be useful for the coalescence of TOPO-capped metal NPs. Furthermore, the conductive metal thin films and heterogeneous metal catalysts were successfully obtained by this method. As far as the author knows, the RT chemical sintering of metal NPs in an organic solvent was systematically investigated for the first time. The author expects that this method will be applicable to a wide range of metal NPs and be adapted to the fabrication of printed electronics such as wearable device and heterogeneous catalysts for fuel cells.

Future Perspectives

The printed electronics is one of the most attractive technologies nowadays. Various approaches have been examined for realization of wearable device. For example, in order to fabricate a foldable electrode, many sintering methods of conductive metal NPs were developed. However, the author thinks that the RT chemical sintering method should be developed more to avoid the damage of the flexible substrate (e.g. paper and plastic substrate).

In this study, the author focused on the RT chemical sintering by dipping into an organic solvent containing a sintering agent. The effect of metal, ligand, dipping solvent, and sintering agent to the coalescence of NPs was systematically investigated. The author demonstrated that metal NPs could be easily sintered at RT with the aid of sintering agents in a nonpolar solvent. The findings obtained in this study would help to select the combination of metal NPs, ligand, dipping solvent, and sintering agent.

While mechanical properties (e.g. tolerance to tensile strain, bending strength, and adhesion between the metal and the substrate) and electrical properties (e.g. resistance of migration) are out of range of this thesis. However, the knowledge obtained here will partly contribute to the fabrication of the flexible electrode because it was shown in this study that the progress of the RT chemical sintering is dominated by the following two factors: “solubility of ligand to dipping solvent” and “interaction between the surface of metal NP and sintering agent”. The better combination of metal NPs, ligand, dipping solvent, and sintering agent for fabricating the flexible electrode would be predicted by considering the two factors in the near future.

In addition, a new approach for the fabrication of porous metal structures from metal NPs was shown in this study. Porous metal structures were researched in terms of heterogeneous metal catalysts. Although the conventional methods for the fabrication of porous metal structures using sacrificial template produce a lot of waste containing metal ion and chemicals for removing the template, the amount of waste could be suppressed in the RT chemical sintering of NPs because the template can be removed easily during the sintering in this method. Therefore, the RT chemical sintering could be a new candidate for the fabrication of porous metal structures in environmental-friendly processes.

When the RT chemical sintering method suggested in this thesis is completely established, great impact would be brought into various industrial fields such as catalysis, cells, and electronics. The author expects that the fabrication of porous structures of various metals (e.g. Zn, Al, and Ni) will contribute to the solution of energy problems by improving the performance of fuel cell, secondary battery, and flexible electrode.

List of Publications and International Conferences

Publication

1) "Crystallite Size Increase of Silver Nanoparticles by Ligand Exchange and Subsequent Washing Process with Antisolvent"
Soichiro Okada, Yoshio Nakahara, Mitsuru Watanabe, Toshiyuki Tamai, and Setsuko Yajima
J. Nanosci. Nanotechnol. **2019**, *19*, 4565-4570. (Chapter 2)

2) "Room-Temperature Sintering of Tri-*n*-Octylphosphine-Oxide-Capped Silver Nanoparticle Paste by Dipping into an Organic Solvent Containing a Sintering Agent"
Soichiro Okada, Yoshio Nakahara, Mitsuru Watanabe, Toshiyuki Tamai, Yasuyuki Kobayashi, and Setsuko Yajima
J. Phys. Chem. C **2019**, *123*, 14118-14125. (Chapter 2)

3) "Room-Temperature Coalescence of Tri-*n*-Octylphosphine-Oxide-Capped Cu-Ag Core-Shell Nanoparticles: Effect of Sintering Agent and/or Reducing Agent"
Soichiro Okada, Yoshio Nakahara, Mitsuru Watanabe, Toshiyuki Tamai, Yasuyuki Kobayashi, and Setsuko Yajima
Bull. Chem. Soc. Jpn. **2021***, 94,* 1616-1624. (Chapter 3)

4) "Room-Temperature Coalescence of Pd Nanoparticles with Sacrificial Templates and Sintering Agents, and Their Catalytic Activities in the Suzuki Coupling Reaction"
Soichiro Okada, Yoshio Nakahara, Mitsuru Watanabe, Toshiyuki Tamai, Yasuyuki Kobayashi, and Setsuko Yajima
in preparation (Chapter4)

International Conference

1) "Coalescence of Tri-*n*-octylphosphine-oxide-Capped Silver Nanoparticles by the Addition of Chloride Salt in Organic Solvent at Room Temperature"

   Soichiro Okada, Yoshio Nakahara, Mitsuru Watanabe, Toshiyuki Tamai, and Setsuko Yajima

   OKINAWA COLLOIDS 2019, November **2019**, Okinawa, Japan (Poster, PT06-04). (Chapter 2)

2) "Room-Temperature Sintering of Tri-*n*-octylphosphine-oxide-Capped Silver Nanoparticle Paste by Dipping into Methanol Containing a Chloride Salt as a Sintering Agent"

   Soichiro Okada, Yoshio Nakahara, Mitsuru Watanabe, Toshiyuki Tamai, and Setsuko Yajima

   International Chemical Congress of Pacific Basin Societies 2021, December **2021**, Online (Poster). (Chapter 2)

Other Publications

1) "Comparison of Physical Adsorption Strength of Protective Agents via Ligand Exchange of Silver Nanoparticles Prepared by Vacuum Evaporation on Running Oil Substrate"

Takashi Ienaga, Soichiro Okada, Yoshio Nakahara, Mitsuru Watanabe, Toshiyuki Tamai, Setsuko Yajima, and Keiichi Kimura

Bull. Chem. Soc. Jpn. **2017**, *90*, 1251-1258.

2) "Synthesis of Silica Nanoparticles with Physical Encapsulation of Near-Infrared Fluorescent Dyes and Their Tannic Acid Coating"

Yoshio Nakahara, Yukiho Nakajima, Soichiro Okada, Jun Miyazaki, and Setsuko Yajima

ACS Omega **2021**, *6*, 17651-17659.

Acknowledgments

This research was conducted under the guidance of Professor Setsuko Yajima, Graduate School of Systems Engineering, Wakayama University. The author expresses sincere thanks to Professor Setsuko Yajima for her invaluable suggestion and kind guidance throughout the Ph.D. study. Her various supports enabled the author to solve many problems in the research life. The author is grateful to Associate Professor Yoshio Nakahara, Graduate School of Systems Engineering, Wakayama University, for his guidance in the experiments. The author was able to complete this thesis owing to his elaborate correction. The author really believes that his strong supports brought about the author’s big growth. The author would like to thank Assistant Professor Shinpei Kado, Graduate School of Systems Engineering, Wakayama University. His accurate advice made the author's Ph.D. study higher-quality. The author is grateful to Professor Hidefumi Sakamoto for the advice in the author’s study.

The author’s research was also carried out in cooperation with Morinomiya Center, Osaka Research Institute of Industrial Science and Technology. The author expresses sincere thanks to Dr. Toshiyuki Tamai for his invaluable suggestion and supports in the experiments. The author would like to thank Dr. Mitsuru Watanabe. His experimental supports and advice improved the quality of the author’s study. The author is grateful to Dr. Yasuyuki Kobayashi for the guidance and advice in the experiments. In addition, they gave the author accurate advice regarding the preparation of the research papers.

The author also would like to express Dr. Takashi Ienaga, Kishugiken Kogyo Co., Ltd. for the collaborations and warm encouragements.

Finally, the author thanks to all the members of Analytical Chemistry Laboratory at Faculty of Systems Engineering, Wakayama University.

Soichiro Okada